Parkinson's disease in the spotlight

Unraveling nanoscale α-Synuclein oligomers using ultrasensitive single-molecule spectroscopy

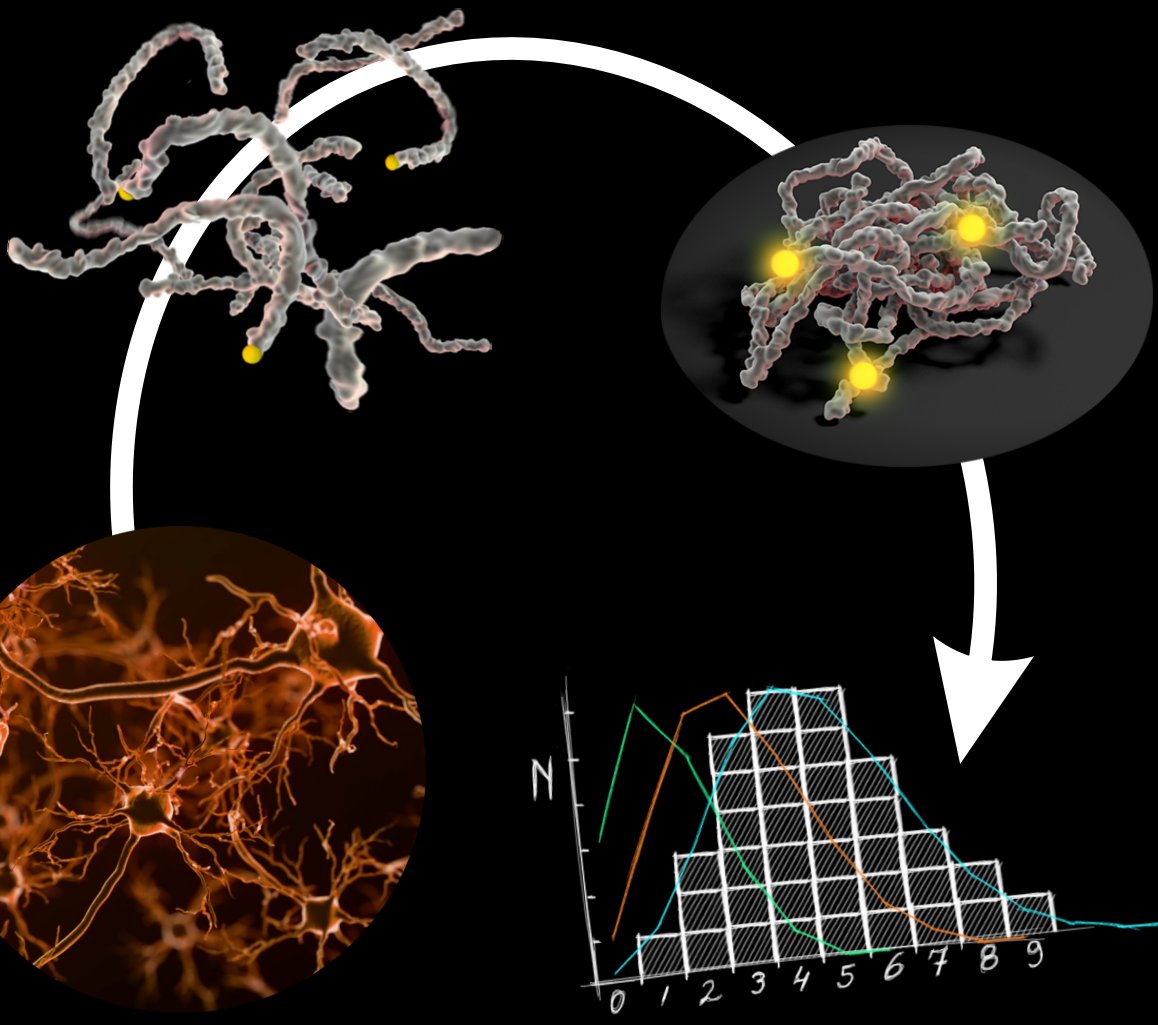

Niels Zijlstra

Parkinson's disease in the spotlight

Unraveling nanoscale α-Synuclein oligomers using ultrasensitive single-molecule spectroscopy

De ziekte van Parkinson belicht

Nanoschaal α-Synucleine oligomeren ontrafeld met behulp van ultragevoelige enkel-molecuul spektroskopie

Promotiecommissie:

Promotor	Prof. Dr. V. Subramaniam	University of Twente
Assistent promotor	Dr. C. Blum	University of Twente
Overige leden	Prof. Dr. M.F. Garcia-Parajo	ICFO The Institute of Photonic Sciences
	Prof. Dr. A.M. van Oijen	University of Groningen
	Prof. Dr. P.W.H. Pinkse	University of Twente
	Prof. Dr. E. Rhoades	Yale University
	Prof. Dr. W.L. Vos	University of Twente

The work described in this thesis was financially supported by the "Nederlandse Organisatie voor Wetenschappelijk Onderzoek" (NWO) through the NWO-CW TOP program number 700.58.302.
Additional funding was provided by the Stichting Internationaal Parkinson Fonds.

The work described in this thesis was carried out at the:
Nanobiophysics group,
MESA+ Institute for Nanotechnology,
Faculty of Science and Technology,
University of Twente, P.O. Box 217,
7500 AE Enschede, The Netherlands.

Cover design: Niels Zijlstra, Nymus3D

ISBN: 978-90-365-3748-3
DOI: 10.3990/1.9789036537483

PARKINSON'S DISEASE IN THE SPOTLIGHT

UNRAVELING NANOSCALE α-SYNUCLEIN OLIGOMERS USING ULTRASENSITIVE SINGLE-MOLECULE SPECTROSCOPY

PROEFSCHRIFT

ter verkrijging van
de graad van doctor aan de Universiteit Twente,
op gezag van de rector magnificus,
prof. dr. H. Brinksma,
volgens besluit van het College voor Promoties
in het openbaar te verdedigen
op vrijdag 17 oktober 2014 om 14.45 uur

door

Niels Zijlstra
geboren op 14 oktober 1983
te Enschede

Dit proefschrift is goedgekeurd door:

Prof. Dr. V. Subramaniam en Dr. C. Blum

Contents

Contents **1**

1 General introduction **5**
1.1 Protein misfolding and disease 5
1.2 Amyloid diseases and the oligomeric species 7
1.3 The protein α-Synuclein 10
1.4 αS oligomers 11
1.4.1 Morphology 12
1.4.2 Structure 14
1.4.3 Aggregation number 16
1.5 Outline of this thesis 18

2 Design and realization of a single-molecule sensitive optical microscope **21**
2.1 Introduction 21
2.1.1 Outline of this chapter 22
2.2 Design of a confocal, single-molecule sensitive optical microscope . . . 22
2.2.1 Requirements for single-molecule detection 23
2.2.2 Instrumentation for the single-molecule sensitive optical microscope 26
2.2.3 Design of single-molecule sensitive optical microscope 27

2.3 Aligning the microscope for optimal performance 31
2.4 Photobleaching: the basics 33
2.4.1 Single-molecule photobleaching 35
2.4.2 Limitations of single-molecule photobleaching approaches . . . 36
2.5 Sample preparation for single-molecule photobleaching 37
2.6 Summary 38

3 Aggregation number of sub-stoichiometrically labeled α-Synuclein oligomers determined by single-molecule photobleaching 41
3.1 Introduction 41
3.1.1 Single-molecule photobleaching on 100% labeled αS oligomers . 42
3.1.2 Sub-stoichiometric labeling 43
3.2 Results and discussion 46
3.2.1 Analyzing time traces 47
3.2.2 Interpreting the histograms of bleaching steps 49
3.3 Conclusions and discussion 53
3.4 Materials and methods 54
3.4.1 αS preparation, labeling, and aggregation 54
3.4.2 Sample preparation 55
3.4.3 Instrumentation and measurement procedure 55

4 Elucidating the aggregation number of dopamine-induced α-Synuclein oligomeric assemblies 57
4.1 Introduction 57
4.2 Results and Discussion 58
4.2.1 The single species approach 58
4.2.2 Multiple distinct species present in the same sample 61
4.2.3 Continuous distribution of oligomer species 66
4.2.4 Determining the optimal label density 67
4.2.5 Dopamine-induced oligomers with different label densities . . . 68
4.2.6 Influence of dopamine: testing a third protocol 72
4.3 Conclusions and discussion 74
4.4 Materials and Methods 75

4.4.1 Instrumentation and measurement procedure 75
4.4.2 αS labeling, aggregation, and oligomer purification 76
4.4.3 Sample preparation for single-molecule spectroscopy 77
4.4.4 Fitting procedure 78

5 Single-molecule photobleaching on sub-stoichiometrically labeled aggregates: How well can we do? 81
5.1 Introduction 81
5.1.1 Difficulties to precisely and accurately determine the aggregation number 82
5.1.2 Additional difficulties arise for systems with more complex compositions 83
5.1.3 Aim of this chapter 83
5.2 Results and discussion 84
5.2.1 The basics: Simulated histograms and their interpretation . . . 84
5.2.2 Optimal range of label densities for a single species 86
5.2.3 Additional uncertainty: Labeling efficiency 89
5.2.4 Choosing and optimizing the label density 91
5.2.5 Two species instead of one 92
5.2.6 Single species or double species? 95
5.3 Conclusions and discussion 97
5.4 Methods 99
5.4.1 Simulation procedure 99
5.4.2 Fitting procedure 100

6 Mapping the conformation of α-Synuclein monomers incorporated in an oligomer 101
6.1 Introduction 101
6.2 Single-pair Förster resonance energy transfer 103
6.2.1 Determining FRET efficiencies in single-pair measurements . . 104
6.2.2 Practical considerations for sample preparation 106
6.3 Doubly labeled αS monomers 107
6.4 Mapping the structure of αS monomers incorporated into oligomers . 109

6.4.1 Determining the FRET efficiency using ensemble emission lifetimes . . . 113
6.5 FRET efficiency histograms of doubly labeled αS monomers . . . 114
6.6 Binding of monomeric αS to SDS micelles . . . 118
6.7 Is the acceptor dye present in the oligomers? . . . 120
6.8 Conclusions and discussion . . . 124
6.9 Materials and methods . . . 126
6.9.1 αS preparation, labeling, and aggregation . . . 126
6.9.2 Samples for single-pair FRET measurements . . . 126
6.9.3 Instrumentation and measurement procedure . . . 127

7 Summary, conclusions, and future directions 129
7.1 Summary and conclusion . . . 129
7.2 How can we use this work in the future? . . . 133
7.2.1 Single-molecule photobleaching and sub-stoichiometric labeling 133
7.2.2 αS oligomers: what should we do? . . . 135

References 137

Nederlandse samenvatting 152

Acknowledgements 157

List of publications 159

Chapter 1

General introduction*

1.1 Protein misfolding and disease

PROTEINS are linear chains of amino acids, typically consisting of a few hundred amino acids [1, 2]. Different proteins have a different number, order, and combination of amino acids. Even though there are only 20 different types of amino acids involved in constructing proteins in the human body, there is an enormous diversity in proteins: the estimated number of different proteins in a human body is about 50-100 thousand [3].

It is not just the chain of amino acids that makes a properly functioning and biologically active protein. For most proteins to function properly, they have to be folded into a unique 3-dimensional (3D) structure [4]. However, during the last decade this structure-function paradigm has been challenged by the discovery of an increasing number of proteins that do not adopt such a unique 3D structure, but are nevertheless functional and biologically active [5, 6]. These proteins are called

* Parts of this chapter have been published as:
[1] N. Zijlstra, and V. Subramaniam, *Structural and Compositional Information about Pre-Amyloid Oligomers*, in: *Amyloid Fibrils and Prefibrillar Aggregates: Molecular and Biological Properties*, D.E. Otzen (ed), pp. 103-126, Wiley-VCH Verlag GmbH & Co. KGaA, Weinheim (2013).
[2] M.T. Stöckl, N. Zijlstra, and V. Subramaniam, *α-Synuclein Oligomers: An Amyloid Pore?*, Molecular Neurobiology **47**: pp. 613-621 (2012).

intrinsically disordered or natively unfolded proteins.

Protein folding is an extraordinarily complex process of which the details are still unclear, but is thought to be governed by the energy landscape of the protein and involves a stochastic sampling of many different folds, or conformations, until the protein reaches its thermodynamically most favorable fold [7]. This fold is usually called the native structure of the protein and is mainly determined by the amino acid sequence of the protein [8, 9], although the complex environment found in a cell is thought to influence the folding as well [10].

The folding of a protein is in some cases co-translational, that is, the folding takes place during synthesis [7, 11, 12]. In other cases, however, the protein folds in the cytoplasm after a complete synthesis, or is first transported to specific parts of the cell, such as mitochondria or the endoplasmic reticulum, before it folds, see figure 1.1 [7, 12].

Given the complexity of protein folding and the enormous number of folding events in a cell, it is not surprising that sometimes a protein does not fold correctly or that a protein does not stay folded correctly [1, 13]. The protein can get trapped in a local energy minimum resulting in the protein to misfold making the protein toxic [1, 14]. The more complex the protein folding pathway is, the more likely it is that the folding goes wrong. Normally, a cell can minimize the amount of misfolded proteins by using specialized molecular chaperones or folding catalysts to assist in the folding [4, 13]. If the folding still goes wrong, the cell can get rid of the misfolded proteins by degrading them via the ubiquitin-proteasome system, see figure 1.1 [15]. Unfortunately, this defense mechanism does not always work properly.

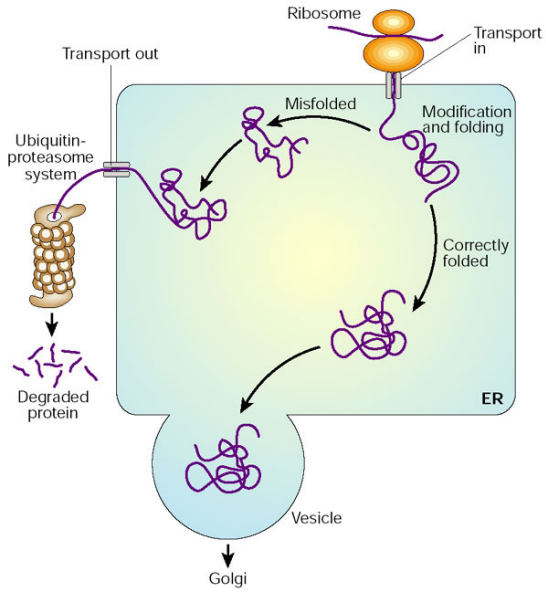

Figure 1.1: One possible protein folding pathway. Newly synthesized proteins are transported into the endoplasmic reticulum (ER), where they fold into their unique 3-dimensional structure. In some cases, this folding process is assisted by molecular chaperones or folding catalysts (not shown). The correctly folded proteins are then transported to the Golgi complex and delivered to the cytoplasm or extracellular environment, while the incorrectly folded proteins are degraded via the ubiquitin-proteasome system. Figure reprinted with permission from [7].

1.2 Amyloid diseases and the oligomeric species

Protein misfolding and the subsequent aggregation is considered to play an important role in many human neurodegenerative diseases, such as Parkinson's, Alzheimer's, and Huntington's disease, type II diabetes, and in the prion diseases [16]. These diseases are associated with the formation of inter- and intracellular inclusions that mainly contain insoluble amyloid fibrillar aggregates. Amyloid refers to the aggregates having a characteristic cross-β sheet secondary structure. These fibrils are $\sim$10 nm

in diameter, and can be several microns in length, and thus are composed of many thousands of the constituent monomeric proteins [17]. A commonly used method to detect the formation of amyloid aggregates uses the fluorescent dye Thioflavin T (ThioT). When ThioT binds to β-sheet-rich domains, the dye displays enhanced fluorescence intensity and a characteristic red shift of its emission spectrum. ThioT fluorescence is often used to monitor the kinetics of amyloid formation, which, in general, follows a sigmoidal growth curve that is characterized by an initial lag phase, followed by an exponential growth until it reaches a saturation level in which no further aggregation occurs [18]. A typical aggregation curve is shown in figure 1.2.

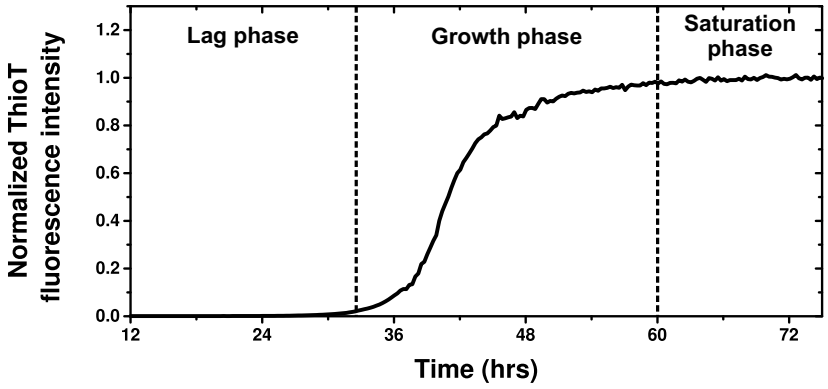

Figure 1.2: Typical aggregation curve monitored with ThioT fluorescence intensity. The lag phase, growth phase, and saturation phase are indicated. In this specific case, the aggregation of 100 μM α-Synuclein was followed.

While much research has been done on the monomeric protein and the fibrillar aggregates [16, 19, 20], it is only since the end of the 1990s that attention shifted from the fibrils to soluble amyloid oligomers as the primary cause of cytotoxicity and hence disease. Oligomers are aggregation intermediates that precede the formation of fibrils (figure 1.3). Both on- and off-pathway oligomers are observed, where, in the presence of monomers, on-pathway oligomers undergo further aggregation into fibrils, while off-pathway oligomers do not. The bi-directional arrows in figure 1.3 indicate

the typically transient nature of the different species observed during the aggregation process, that is, the species are prone to either undergo further aggregation into fibrils or dissociate into smaller oligomers or even monomers. Under specific conditions, it might be possible to stabilize the oligomers and prevent them from dissociating or aggregating further, as we will discuss below for α-Synuclein oligomers formed under specific conditions.

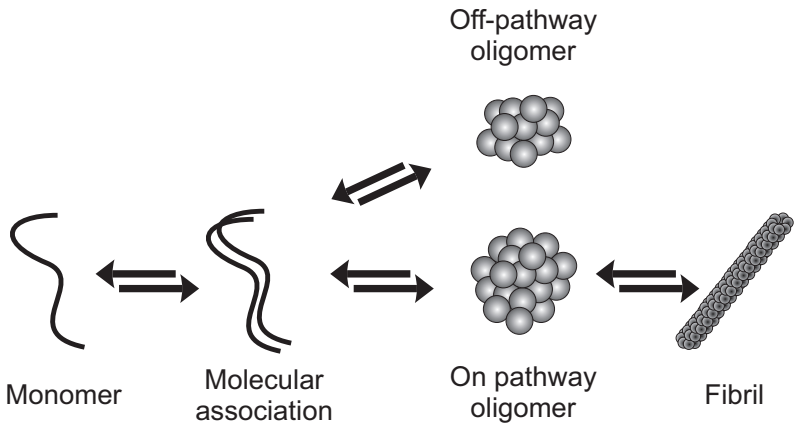

Figure 1.3: Simplified representation of the protein self-assembly process. Monomers can self-associate and form oligomers, which in turn can form fibrillar structures. Typically, the species observed are not stable and can dissociate or aggregate further. Off-pathway oligomers are also observed, and are not competent to form fibrils. In reality, the aggregation process is significantly more complex than depicted in the schematic above, and many more species can be observed, since the oligomers are not often a well-defined species.

There is growing evidence that suggests that the oligomeric form may play a primary role in the mechanisms of many amyloid diseases [21, 22], with fibrils likely to be inert bystanders in the disease process [23–25]. Cellular toxicity studies have shown that oligomers have a higher cytotoxicity compared to the fibrillar form of the proteins [21, 26–30].

Therefore, molecular insights into the structure, morphology, and aggregation number of these oligomeric aggregates are essential for understanding the aggregation

process and ultimately the cause of the disease. Despite the fact that the oligomeric form is considered a very important species, information on their structure and aggregation number is very limited, due to the typically extremely low concentrations and transient nature of these oligomers.

1.3 The protein α-Synuclein

The neuronal protein α-Synuclein (αS) is considered to play a critical role in the onset and progression of Parkinson's disease [31]. The pathological hallmarks of Parkinson's disease are intracellular inclusions called Lewy bodies and Lewy neurites that are composed largely of αS amyloid fibrils [32]. These inclusions appear to accompany the loss of dopaminergic neurons mainly in the *Substantia Nigra* [33], which is located in the midbrain.

αS is a 140 amino acid protein that is abundantly expressed in the human nervous system. αS has no stable secondary or tertiary structure at physiological pH and has been considered an intrinsically disordered protein, although very recent reports suggest that αS exists as a helical tetramer in vivo [34, 35], but these observations remain a matter of considerable debate [36]. Most Parkinson's disease patients suffer from a sporadic form of the disease involving wild-type αS. About 15% of the patients however have one of the seven point mutations (A18T, A29S, A30P, E46K, H50Q, G51D, or A53T) in the N-terminal part of the protein causing a familial form of Parkinson's disease [37–42]. The normal biological function of αS is not yet understood, which makes it very difficult to determine its exact role in Parkinson's disease, but several possible biological functions are suggested [43]. It has been show that tubulin significantly increases αS fibril formation and that αS might be active as a functional microtubule-associated protein [44, 45]. Additionally, a number of studies showed indications of an important role for αS in membrane-associated processes in the presynaptic terminal [43, 46], including the regulation of dopamine neurotransmission [47]. Interestingly, it has also been suggested that αS might have a role as a molecular chaperone [48], specifically in the folding or refolding of synaptic SNARE proteins, which are involved in the regulation of vesicle fusion [49, 50].

As mentioned in section 1.2, current thinking suggests that fibrillar aggregates and

inclusions are potentially not harmful, and represent a neuronal defense mechanism, while oligomeric αS aggregates are likely to be significantly more toxic to neurons. The formation of αS oligomers follows the same aggregation pathway as depicted in figure 1.3. During the past ten years, a large number of studies has addressed the cytotoxicity of αS oligomers [23, 24, 27, 30, 51, 52], but detailed information on their structure, morphology, and aggregation number is lacking.

1.4 αS oligomers

There are many preparation protocols available to create αS oligomers *in vitro*. However, it remains an open question what the biologically most relevant conditions are to prepare oligomers. The currently available protocols differ in terms of protein concentration, incubation times, agitation speeds, temperature, and buffer conditions [53–57]. Furthermore, the addition of specific compounds, such as dopamine [58–62], 4-hydroxy-2-nonenal (HNE) [63], docosahexaenoic acid (DHA) [64], lipids [52, 65–68], organic solvents [56, 69], or metal ions [56, 57, 70] can influence the aggregation of αS resulting in possibly different oligomers.

Because there is a large number of different protocols to prepare αS oligomers, one of the major difficulties in the field is to identity the actual cytotoxic species. In the very unlikely situation that there is only a small set of cytotoxic oligomers found *in vitro*, it remains a challenging task to fully characterize these and potentially find similarities between these oligomers that allow us to develop efficient drugs. Moreover, it remains a challenge to link the complex aggregation pathways observed *in vitro* with what actually happens inside the cell, since the biologically complex interior of a cell is likely to affect the aggregation process and thus the oligomers formed.

As is highlighted above, there are many different aggregation protocols for αS oligomers, all resulting in oligomers that differ in terms of morphology, structure, and aggregation number. In the next three sections, we will summarize the information known about αS oligomers.

1.4.1 Morphology

Morphological studies of αS oligomers prepared using different protocols have revealed a large diversity of apparent structures, see figure 1.4. Atomic force microscopy (AFM) and electron microscopy (EM) studies showed spherical oligomers with diameters up to 30 nm [71] and heights ranging between 2-10 nm [72–75], although there is also a report about spherical shaped supramolecular intermediate aggregates with diameters of a few 100 nm [76]. Additionally, spheroids [77, 78], annular shaped oligomers [72, 79, 80], and chains of spheres [74] have also been observed. Another report has observed with AFM that an extended incubation time resulted in an increase of annular shaped oligomers, while stirring during the aggregation resulted in more compact but highly heterogeneous oligomers [77]. We note that AFM and EM studies require a suitable substrate and that typical sample preparations involve drying, which may influence the true morphology of the oligomeric species.

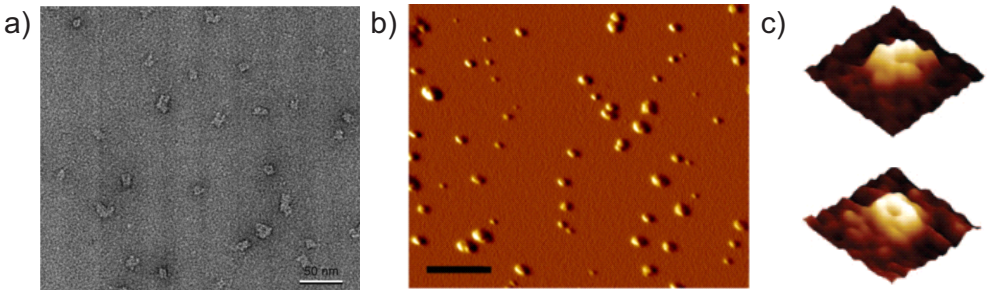

Figure 1.4: **(a)** Negative stain EM image showing annular and tubular αS oligomers. (Figure reprinted with permission from [79].) **(b)** Typical AFM image of Baicalein-stabilized αS oligomers showing spherical oligomers with heights between 2.5 and 8.5 nm and widths between 10 and 30 nm. Scale bar is 200 nm. (Figure reprinted with permission from [75].) **(c)** Two high resolution AFM images showing annular-shaped αS oligomers. Image size is 25 nm. (Figure reprinted with permission from [80]. Copyright (2005) National Academy of Sciences, U.S.A.)

Small angle X-ray scattering (SAXS) has been used to determine the structure

of proteins and protein aggregates that have sizes in the nanometer range. A major advantage of SAXS is that the measurements can be performed in physiologically relevant conditions in solution, although SAXS measurements require high concentrations of protein and the final resolved protein structure is the average of many proteins. In two recent studies, SAXS measurements in solution on oligomers formed under high protein concentrations at 37 °C yielded a low-resolution structure of ellipsoidal shaped oligomers with a radius of about 4.5 nm and a radius to length ratio of about two [54, 81] (see figure 1.5).

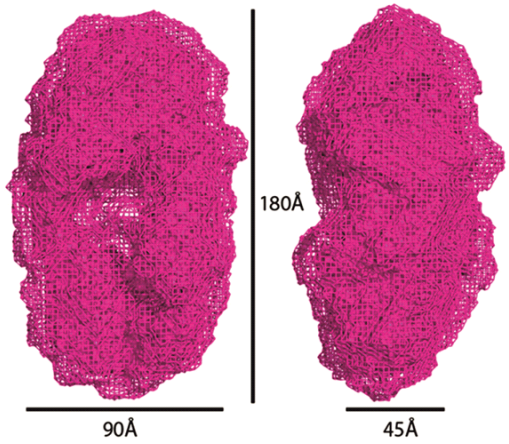

Figure 1.5: Low resolution SAXS derived structure of αS oligomers showing a slightly elongated annular species. The averaged (mesh representation) and filtered averaged (surface representation) structures are superimposed. The model is shown in two orientations, rotated by 90° around the longest axis. (Figure reprinted with permission from Ref. [54]).

In addition to these preparation protocols without any additional compounds present during aggregation, it has been shown that the morphology of αS oligomers is affected by molecular crowding [82] or by the addition of lipids [52, 65–68], or organic solvents [56, 69], or metal ions [56, 57, 70]. Furthermore, it has been shown that the aggregation of αS can be influenced by the addition of docosahexaenoic acid (DHA)

[64], dopamine [58–62], 4-hydroxy-2-nonenal (HNE) [63], or by using a C-terminally truncated variant αS(1-108) [83].

Transmission EM and AFM analysis on the DHA oligomers showed that the addition of DHA in a 50:1 ratio to the protein resulted in stable oligomers, typically spherically or annularly shaped with diameters of about 11 nm [64]. The addition of the neurotransmitter dopamine induces αS to form soluble, sodium dodecyl sulfate (SDS)-resistant oligomers, which are small and irregular shaped [58–62]. SAXS measurements of dopamine-induced oligomers indicated a globular species with a radius of gyration between 6.7 and 10.5 nm [62]. For HNE-induced αS oligomers, AFM measurements showed protofibril shaped oligomers of 2-4 nm in height and lengths between 100-200 nm [63]. Additionally, annular structures were observed having inner diameters of 30-50 nm, outer diameters of 80-100 nm, and heights of 1-2 nm. While the aggregation was accelerated for the C-terminal truncated version, there was less polymorphism in the oligomers [83].

1.4.2 Structure

The structure of oligomers can be separated into two categories: their secondary structure and their tertiary/quaternary structure. The secondary structure of αS oligomers has been investigated extensively by Raman microscopy, Fourier Transform Infrared (FTIR) spectroscopy, and circular dichroism (CD) spectroscopy, which revealed that αS oligomers contain a significant amount of α-helical and β-sheet structure [75, 77, 84, 85].

As mentioned above, the aggregation of αS can be accelerated by the addition of DHA [64] or dopamine [58–62]. For the DHA-induced oligomers, FTIR showed that the oligomers had a decreased fraction of random structure and an increased fraction of α-helix. For the dopamine-induced oligomers, a lack of ThioT binding was found, indicating that they do not possess characteristic amyloid structures [58]. Furthermore, CD showed a decrease in random coil, but no indication of an increase in either β-sheet or α-helix.

The tertiary and quaternary structures of αS oligomers have been investigated much less. Our lab has focused on αS oligomers formed under high protein

concentrations and long incubation times. The oligomers formed under these specific conditions were found to be stable for a prolonged time of about four weeks when purified by size exclusion chromatography to minimize the amount of monomers, stored at 4 °C, and at an oligomer concentration in the nM range.

In an attempt to understand the global structure of these αS oligomers, a systematic structural study was performed by generating a series of Tryptophan (Trp) -containing mutants (wild-type αS does not contain Trp residues) and performing Trp fluorescence spectroscopy [53]. The intrinsic fluorescence of the amino acid Trp can be used to monitor the microenvironment of the Trp residue, since it shows a polarity dependent fluorescence emission maximum [86–88].

Figure 1.6 shows that the monomeric αS exhibits relatively red-shifted Trp fluorescence spectra, indicative of significant solvent exposure of the Trp residues, as would be expected for an intrinsically disordered protein. In the oligomer, a very different picture emerges. Trp fluorescence from αS oligomers containing Trp residues engineered at positions 4, 39, 69, and 90 of the amino-acid sequence exhibit a very significant blue shift of the spectrum, suggesting that these residues are well-shielded from the solvent, and form the core of the oligomeric aggregate. In contrast, C-terminal Trp residues (at positions 124 and 140) continue to exhibit red-shifted fluorescence in the oligomeric state, indicating that the C-terminus of the component monomers remains solvent exposed [53].

On the other hand, Dusa *et al.* have reported that residue 39 is solvent exposed in the transient oligomers formed during αS aggregation [89]. Dusa *et al.* used agitation at 120 rpm in contrast to 1250 rpm that we have used. Although not conclusive, these differences may significantly influence the role of secondary nucleation events in the formation of oligomers, as discussed extensively by Knowles and coworkers [90–92]. These differences in results highlight the need to carefully characterize the wide range of oligomeric species that can be formed during aggregation.

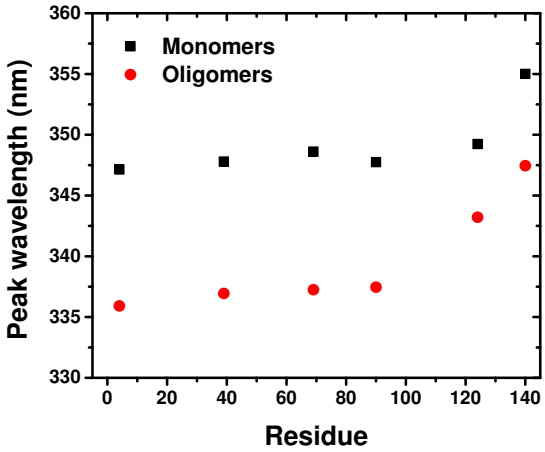

Figure 1.6: The peak wavelength of the Trp emission for monomeric αS (black squares) and oligomeric αS (red circles). For the oligomers, residues 190 of the component monomers are well shielded from the solvent, while the C-terminal residues remain significantly more solvent exposed. See also Ref. [53].

1.4.3 Aggregation number

To date it still remains unclear if the wide range of aggregation numbers found for αS oligomers, that is, the number of monomers forming one oligomer, originates from the presence of a variety of different oligomers resulting from different aggregation protocols or is attributable to the methods used to acquire these data.

The aggregation number of oligomeric protein aggregates is usually determined by calculating the number of monomers per oligomer from the molecular weight of the oligomer. Two commonly used methods for molecular weight determination are SDS- or native-PAGE gels or size exclusion chromatography (SEC). Various reports estimate the aggregation numbers between 5 and 50 monomers per oligomer, depending on preparation protocols and specific stage in the aggregation process [23, 51, 62, 93, 94]. However, both the gels and SEC yield unreliable results especially for aggregates of intrinsically disordered proteins such as αS, since αS oligomers migrate anomalously on columns and gels and therefore have larger apparent

hydrodynamic radii compared to globular proteins which are typically used as reference proteins.

Alternatively, mass spectrometry is used on protein complexes [95]. However, αS forms large oligomeric species, which are potentially at the limit of what can be measured accurately by mass spectrometry and are on top of this very unstable under the ionization conditions necessary for mass spectrometry, which makes the application of this technique to αS oligomers challenging.

Sedimentation velocity analytical ultracentrifugation (SVAU) determines the rate at which molecules move when a centrifugal force is applied by measuring the radial absorbance. This rate can then be linked to a molecular mass. This technique has been used to determine the aggregation number of dopamine-induced oligomers, resulting in a range from 8 to 60 monomers per oligomer [62].

Fluorescence spectroscopy is becoming an increasingly important tool to determine the aggregation numbers of protein aggregates. Fluorescence intensity analysis, for example, determines the ratio between the intensity of a monomer and the intensity of an oligomer to estimate the aggregation number. All monomeric subunits of the oligomer should be fluorescently labeled. However, incomplete labeling in combination with increased fluorescence quenching by the oligomer can significantly influence the aggregation numbers found. Consequently, the estimated aggregation numbers for αS oligomers formed *in vitro* range between 20-50 monomers per oligomer [56, 96], while in a recent study, an aggregation number of about six was found for oligomers formed in cells [97].

In a recent study, Cremades *et al.* investigated the aggregation number of αS oligomers formed under low protein concentrations during long incubation times at 37 °C [98]. The authors linked the apparent aggregation number of the oligomers determined by two-color coincidence detection (TCCD) method to the structure of the oligomers determined by single-molecule Förster resonance energy transfer (FRET) measurements. TCCD uses the simultaneous bursts of two fluorescent labels that have different emission wavelengths and are both incorporated into a single oligomer. All monomers were fluorescently labeled in a 50/50 ratio between the two fluorescent labels. Using only simultaneous bursts ensures that an oligomer is observed, since a monomer only contains one fluorescent label. By comparing the intensity of the bursts

of single oligomers to the bursts of single monomers, one can determine the number of monomers per oligomer. FRET is a technique that is based on the energy transfer of a donor fluorophore to an acceptor fluorophore and is a very sensitive method to determine the distance between the donor and acceptor. The distance between the donor and acceptor can be determined by comparing the emission intensity from the donor fluorophore with the emission intensity of the acceptor fluorophore. Cremades *et al.* observed four distinct distributions of oligomers, namely A_{small}, A_{med}, B_{med} and B_{large}, where A and B indicate low and high FRET efficiencies respectively, and small indicates ∼2-5-mers, medium indicates ∼5-15-mers, and large indicates ∼15-150-mers. The difference in FRET values of A and B oligomers suggest that they have a different structure.

To gain more insight into possible differences in aggregation numbers between αS oligomers, a more direct approach to study the aggregation number of αS oligomers is needed. Additionally, this technique should ideally also be suitable to study the αS oligomers formed at physiological concentrations in a cellular context, since cellular membranes and other components are likely to affect the aggregation process and hence the oligomers formed.

Single-molecule photobleaching offers a very suitable technique to directly probe the aggregation number of oligomers and to determine a possible heterogeneity in the number of monomers per oligomer. Single-molecule photobleaching does not rely on determining the molecular mass of the oligomer, comparison with a reference sample, or the need for a high spatial resolution. This technique has been successfully used to study the aggregation number of amyloid-beta oligomers [99, 100], but has not been applied to αS oligomers.

1.5 Outline of this thesis

To gain more insight into possible differences in aggregation numbers between αS oligomers, we develop a new approach that combines single-molecule photobleaching and sub-stoichiometric labeling to directly study the aggregation number of αS oligomers formed under a variety of different conditions. Chapter 2 describes the custom-built, optical microscope with single-molecule sensitivity that was used to

perform the photobleaching experiments and the basic principles behind single-molecule photobleaching. In chapter 3, we determine the aggregation number of αS oligomers formed under high protein concentrations and long incubation times using a technique that we developed that uses the combination of single-molecule photobleaching and sub-stoichiometric labeling.

As was discussed in this chapter, there are indications that the formation of αS oligomers strongly depends on the aggregation protocol used. Therefore, we also study the aggregation number of dopamine-induced oligomers, see chapter 4. We show that our new method is capable of distinguishing multiple species present in the same sample and can determine the aggregation number for multiple species present in the same sample.

To gain a practical insight into the accuracy with which we can determine the aggregation numbers of the single and double species we found in chapters 3 and 4, we used simulated histograms of bleaching steps in chapter 5. Additionally, we show some general trends in the optimal range of label densities and discuss under which conditions we are able to distinguish a single species from two species.

To better understand the aggregation process, it is essential to not only study the aggregation numbers of oligomers, but also the initial steps of aggregation. Since not all αS monomers present in the human brain aggregate and since we found indications that the oligomers have a specific structure (see chapters 3 and 4), it is likely that only monomers having a specific conformation are able to self-assemble. To gain more insight into the aggregation prone conformations of the monomer, we investigated the structure of αS monomers incorporated into an oligomer using single-pair Förster resonance energy transfer measurements in chapter 6.

In the final chapter, we will summarize and discuss all results obtained in this thesis. We will discuss how these results influence the currently existing global picture of αS oligomers and suggest promising directions for future research.

Chapter 2

Design and realization of a single-molecule sensitive optical microscope

2.1 Introduction

Over the past decades, fluorescence spectroscopy has become an indispensable tool within biology and the biophysical sciences. As was highlighted in the previous chapter, both ensemble and single-molecule fluorescence spectroscopy approaches have been extensively used to study amyloid oligomers. Although ensemble fluorescence spectroscopy is typically easy to implement due to the generally high fluorescence intensities and can quickly provide information about the average properties of the system under study, it also obscures the properties and behavior of subpopulations. Information on hidden subpopulations becomes crucially important when the system is thought to be heterogeneous, as is thought for α-synuclein (αS) oligomers.

Single-molecule spectroscopy can provide insights into the individual properties

and behavior of these subpopulations: it removes the ensemble averaging by looking at single particles. The technique itself, however, is far more complex to implement compared to ensemble spectroscopy due to the inherently low emission intensities associated with single fluorophores. A single fluorophore can only emit a limited number of photons before it photobleaches, that is, before it irreversibly loses its ability to fluoresce. Typically, a fluorophore can emit about 10^5 to 10^6 photons before it photobleaches [101, 102]. For single-molecule spectroscopy, it is therefore very important to collect as many photons as possible within the lifespan of the fluorophore. The limited number of photons requires a careful optimization of the signal-to-noise ratio for a single-molecule sensitive experimental setup.

2.1.1 Outline of this chapter

In this chapter, we will describe the custom-built single-molecule sensitive optical microscope setup that we realized to study αS oligomers and discuss the considerations that played a role in the design, see section 2.2. We will also shortly discuss how the alignment can be optimized to reach a maximum sensitivity and signal-to-noise ratio, see section 2.3. As was emphasized in the previous chapter, single-molecule photobleaching is especially suitable to characterize amyloid oligomers in terms of their aggregation number. In section 2.4, we will discuss the basic principles of photobleaching and the limitations of this approach. Since the setup has single-molecule sensitivity, small intrinsically fluorescent contaminations in the sample can easily be confused with the oligomers under study. Therefore, it is extremely important to have clean samples with no, or as few as possible, fluorescent contaminations. In section 2.5, we discuss how we clean microscope coverslips and prepare typical samples suitable for single-molecule measurements.

2.2 Design of a confocal, single-molecule sensitive optical microscope

In this section, we will discuss the basic requirements for single-molecule detection. Subsequently, we address the requirements for the microscope instrumentation. The

aim was to realize a multipurpose single-molecule sensitive setup, capable of measuring fluorescence intensities and emission lifetimes for a wide range of fluorophores at the single-molecule level both *in vitro* and *in vivo*. Additionally, the setup should be adjustable to perform fluorescence correlation spectroscopy (FCS) and Förster resonance energy transfer (FRET) measurements. Not all of the requirements for instrumentation discussed in this section have been used for the measurements described in this thesis. Finally, we will present the design of the microscope.

2.2.1 Requirements for single-molecule detection

There are two main requirements for single-molecule detection. First, one needs to make sure that only a single molecule is in the detection volume during the observation time. Second, the signal-to-noise ratio needs to be maximized, but should be at least unity to be able to distinguish the signal from a single molecule from the background noise [103].

Guaranteeing that only one molecule is observed at a time can be achieved by making the observation volume as small as possible while using low sample concentrations. Achieving the highest possible signal-to-noise ratio requires minimizing the background noise while simultaneously maximizing the signal.

2.2.1.1 Minimizing the background noise: a small detection volume is essential

The main sources of background noise in optical microscopy are fluorescence from optical parts, elastic scattering of the excitation light of the laser, and background photons coming from the sample itself [103]. Other noise sources include dark counts from detectors and the shot-noise in the single-molecule emission, but these sources are typically much lower than those mentioned above and are therefore neglected here.

The fluorescence from optical parts can be easily minimized by choosing high quality optical components specifically designed for having minimal fluorescence. Since the elastic Raleigh scattering of the laser light has the same wavelength as the excitation light and hence does not fall within the same spectral region as

the fluorescence signal of interest, it can usually be suppressed efficiently by using appropriate emission filters. Background photons originating from the sample, however, are much more difficult to suppress. There are two main sources of background photons originating from the sample, namely the inelastic Raman scattering of the excitation light from the substrate or solvent and the fluorescence from impurities present in the sample. The inelastic Raman scattering might fall into the same spectral region as the fluorescence signal of interest and is therefore difficult to suppress. Impurities in the sample can be minimized by using ultrapure solvents, but cannot be completely avoided. However, both the inelastic Raman scattering and the number of impurities observed depend on the detection volume and can therefore be minimized by limiting the detection volume as much as possible. For a typical detection volume of about 1 fL, the total Raman scattering is about 100 times smaller than the fluorescence signal of a single molecule [103].

The size of the detection volume is thus a crucial parameter in single-molecule detection. Therefore, we chose to build a confocal microscope, since the confocal detection scheme offers a convenient approach to realize a small detection volume.

2.2.1.2 Maximizing the collected signal: the collection efficiency

As was highlighted above, the number of photons that a single fluorophore can emit is inherently limited and hence, the maximum signal that can be collected from a single fluorophore is also limited. Over the last decade, there has been a continuous improvement in the brightness and photostability of fluorophores, greatly improving the number of photons emitted by a single fluorophore. However, the collection efficiency of a microscope is limited by the components used and will significantly limit the signal that can be collected from a single fluorophore. Therefore, to maximize the collected signal, it is important to maximize the collection efficiency of the optical microscope or, equivalently, to minimize the losses in the microscope.

There are two key components in the optical microscope that considerably limit the collection efficiency and therefore should be carefully considered when designing a single-molecule sensitive setup: the microscope objective and the single-photon counting detector. Of course, there are many additional factors that all combine to

significantly influence the collection efficiency, such as the emission filters, dichroic mirror, wavelength dependent detection efficiency of the detectors, and the preferred emission direction of dipoles into high refractive index media. However, these factors do not influence the design choices discussed in this section and are therefore not considered.

The collection efficiency of a microscope objective is mainly determined by its numerical aperture (NA), or simply speaking, its collection angle: the larger the collection angle, the more light is collected. It is therefore necessary to use microscope objectives with a high NA, so that one can collect over the largest possible solid angle. The highest available NA for an oil immersion microscope objective is about 1.4, which limits the solid angle over which light is collected to about 1.6π steradian. Since a full sphere has a solid angle of 4π steradian, even by using an objective with the highest possible NA, the maximum collection efficiency of the microscope will be limited to about 40%. However, the optical microscope should be suitable for single-molecule studies in a cellular environment and for FCS measurements in solution. Therefore, a water immersion objective is more suitable than an oil immersion objective, since using water as immersion medium will greatly reduce the spherical aberrations introduced by the refractive index mismatch between the immersion medium and the cell interior or an in vitro sample in buffer solution [104]. However, the NA of water immersion objectives is lower than that of oil immersion objectives, maximally about 1.2, which limits our collection efficiency to about 28%. In addition, the microscope objective used (UplanApo/IR, 60X, 1.2NA, water immersion, Olympus, see also section 2.2.3) has, according to the manufacturer, about 60% transmission at 550 nm. Therefore, the total collection efficiency of the microscope objective is about 17%.

Secondly, another source of losses is the single-photon detector. For single point detection, as is used in confocal microscopy, there are two options for detectors: the photo multiplier tube (PMT) and the avalanche photodiode (APD). One of the main advantages of APDs over PMTs is their detection efficiency. PMTs have significantly lower detection efficiencies of $\sim$20% as compared to APDs with efficiencies $\sim$60%, especially in the visible wavelength range we are interested in (500-700 nm). Additionally, APDs typically have a very low background rate in the order of 20-200 counts per second, which is comparable with or even better than the best

PMTs. We therefore chose to use APDs instead of PMTs.

By only considering the high NA microscope objective and the single-photon detectors, the total detection efficiency of our setup is limited to about 10%. In addition to these two components, every interface the emission light encounters on its way to the detector will introduce additional Fresnel losses. It is therefore important to minimize the number of interfaces as much as possible. The custom-built confocal microscope we designed (see section 2.2.3) has eight reflecting glass interfaces in the detection path that all contribute a 4% loss plus one silver mirror contributing a 2% loss in the fluorescence emission, resulting in a total additional loss of about 30%.

Combining these losses (the microscope objective, APD, and reflecting surfaces), the maximum collection efficiency of the microscope can be estimated at about 7%, which is in good agreement with the estimate made by Meixner *et al.* [105]. The low collection efficiency for a typical single-molecule sensitive optical microscope highlights the need to both minimize the background noise and strive to maximize the collected signal by carefully choosing the components as discussed above.

2.2.2 Instrumentation for the single-molecule sensitive optical microscope

As was highlighted in the previous section, a small detection volume and high collection efficiency are crucial for single-molecule detection. Therefore, we chose to design a confocal microscope in combination with a high NA objective and APD detectors. The literal translation of the term confocal is "having the same focus", which means that the excitation focus (or volume) is at the same position as the detection focus (or volume): the two volumes overlap. Since only a single point is illuminated at the same time, the sample needs to be raster scanned through these volumes to create an image. Additionally, for studying single molecules, it is very important to be able to accurately reposition a single molecule in these volumes again after it is localized with an initial area scan. Since for single-molecule detection a very small detection volume is imperative, it is essential to move the sample with a high repeatability to guarantee that the same single-molecule is located in the detection volume again. A high repeatability, typically less than a few nanometers, is provided

by piezo scanning stages.

To be able to access not only the fluorescence emission intensities, but also time-resolved lifetime data from the single fluorophores, we chose to do time-correlation single-photon counting (TCSPC). TCSPC is typically operated in reverse mode and is based on measuring the time between the arrival of a photon at the detector and the excitation pulse [101]. By measuring many of these events, a histogram of photon arrival times can be built, from which the emission lifetime can be determined. Of course, TCSPC still allows access to the fluorescence emission intensities.

As will be explained in chapter 6, FRET is an ideal tool to study inter-dye distances at the nanometer scale. To be able to determine the FRET efficiency, it is necessary to record the fluorescence intensities for both the donor dye and acceptor dye simultaneously. Therefore, a detection scheme comprising two detection channels and hence two APDs is needed.

2.2.3 Design of single-molecule sensitive optical microscope

Taking all these considerations into account, we chose to build a sample scanning, inverted confocal microscope with two detection channels. Figure 2.1 shows a schematic of the custom-built confocal microscope.

Two pulsed diode lasers operating at 485 nm and 640 nm with a tunable repetition rate of up to 80 MHz (LDH-D-C-485 and LDH-D-C-640, both Picoquant) were coupled into the same single mode fiber using a microscope objective (Plan N, 10x, 0.25NA, Olympus), that closely matched the NA of the optical fiber to obtain a maximum incoupling efficiency. A single-mode fiber was used to create the high quality Gaussian beam profile necessary for FCS measurements. Additionally, using a single fiber for both lasers guarantees spatial overlap between the two laser beams. These two laser sources were chosen to closely match the excitation wavelengths of a wide range of commonly used fluorophores, including the Alexa Fluors 488 and 647 (or similar dyes from Atto-Tec), the Green Fluorescent Protein (GFP), Fluorescein, Rhodamine6G, and RhodamineB. Since the setup needs to have the capability to measure emission lifetimes, pulsed laser sources are required.

The laser light was collimated with a microscope objective (Plan N, 4x, 0.1NA,

Olympus), creating a beam diameter closely matching the diameter of the back aperture of the microscope objective enabling the use of its full NA. The fiber output was mounted on a 5-axis platform that allows for a precise beam collimation and high quality beam profile. Subsequently, the laser light was spectrally cleaned by a dual band excitation filter (ZET488/640x, Chroma Technology).

The laser light was coupled into the microscope objective (UplanApo/IR, 60X, 1.2NA, water immersion, Olympus) by a wedged glass plate with a typical reflection of less than about 2%, minimizing the loss of fluorescence emission. Since the currently available high NA microscope objectives have excellent corrections for chromatic aberrations, an epi-illumination configuration was used in which the excitation and emission collection are through the same microscope objective. Moreover, this configuration minimizes alignment as compared to using a transmission configuration with two separate microscope objectives for excitation and emission collection. The sample was mounted on a piezo-nanopositioning stage (Physik Instrumente, P-733, range 100 x 100 μm^2) having a high repeatability of less than 2 nm.

The emission light was spatially filtered using a confocal pinhole of which the diameter was optimized for each experiment, ranging between 15 μm and 50 μm. The appropriate pinhole size can be determined using a number of ways and typically the size depends on the information that needs to be obtained from the measurements. FCS, for example, has very strict requirements for the pinhole size since the analysis depends on the assumption of a very well-defined Gaussian shaped confocal volume, while for intensity measurements the requirements are much less strict, since the pinhole is only used to minimize the detection volume [106, 107]. A shared pinhole was chosen for both detection channels, since the difference in emission wavelengths between both channels (if used simultaneously) will be less than 100 nm. The pinhole can be aligned optimally for both wavelengths at the same time for these small wavelength differences. Furthermore, maintaining optimal alignment for a single pinhole is easier than for the case with two separate pinholes.

The remaining excitation light in the detection path was suppressed with a combination of filters that depended on the excitation wavelength used. To collect fluorescence intensity, the emission light was focused onto either one or two single-photon avalanche photodiodes (APD) (SPCM-APQR-16, PerkinElmer) with

a quantum efficiency of more than 50% in the wavelength range of 500-750 nm. Both APDs are connected to a TCSPC module (PicoHarp300, Picoquant) via a four channel detector router (PCH800, Picoquant) allowing to measure both fluorescence intensities and emission lifetimes for up to four detection channels. Additionally, the PicoHarp300 has two independent but synchronized input channels allowing for antibunching measurements and has the capability to do online FCS.

Both the optional dichroic mirror, which could be used to split the fluorescence emission between the two detectors, and the emission filters were optimized for each experiment.

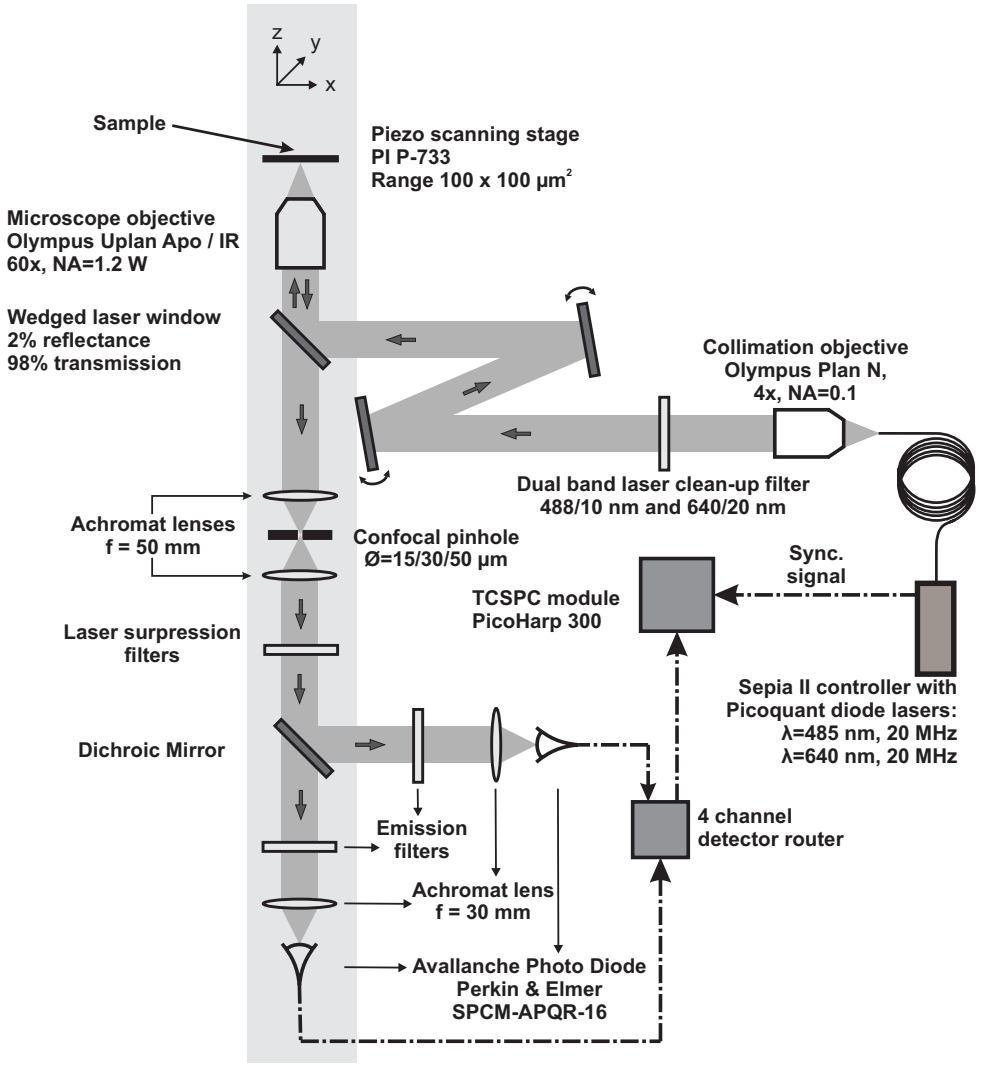

Figure 2.1: Schematic of the custom-built confocal microscope. Gray paths and dash-dotted lines denote optical and electrical signals, respectively. Arrows indicate the direction of the signals. An epi-illumination setup was used, i.e., illumination and emission collection through the same microscope objective. The emission light is spatially filtered by a single confocal pinhole before it is spectrally split into two detection channels. The light gray box on the left side indicates the detection path for a single APD.

2.3 Aligning the microscope for optimal performance

For an optimal performance of a single-molecule sensitive microscope, there are a few aspects in the alignment that need to be considered carefully. Aligning a single-molecule sensitive setup is an iterative process. Therefore, going through the steps described below only once may not provide the optimal result and multiple iterations might be necessary.

Since we are using confocal microscopy, one of the most important aspects is the overlap between the excitation volume and the detection volume. If these two volumes do not overlap perfectly, one needs to use much more excitation power then necessary to be able to image a single fluorophore, which will result in rapid photobleaching of the fluorophore. Since the beam path on the detection side is stationary, the location of the detection volume volume cannot be changed and it is therefore the excitation volume that needs to be overlapped with the detection volume. Please note that the x- or y-position is used to refer to positions perpendicular to the beam direction, while the z-position is used to refer to the position parallel to the beam direction, see also figure 2.1.

A perfect overlap can only be obtained with a perfectly collimated excitation beam, since any decollimation will result in a change in the z-position of the excitation volume. Furthermore, to overlap the detection and excitation volumes in the x-y plane, it is very important to go straight and on-axis through the microscope objective. If the beam is off-axis or at an angle, the x-y location of the excitation volume will be changed.

An easy way to verify that the beam is going on-axis and straight through the microscope objective is by imaging the point spread function (PSF) of a single emitter. If the incoming excitation beam has a perfect Gaussian intensity profile, the PSF can be approximated with a Gaussian intensity profile when imaging a single emitter. Of course, small deviations in the PSF will always be observed, since reflections in the emission path or a not completely circular pinhole can distort the PSF slightly.

However, before a single emitter can be observed, the rest of the microscope needs

to be aligned as well. Therefore, first the detector needs to be aligned, which is a multi-step process, especially when aligning the setup for the first time. A commonly used method to align the detector is by using samples having decreasing brightness and each time maximizing the intensity recorded with the detector.

Therefore, the first step is to image the reflection of the laser beam. This allows us to easily find the sensor of the detector and get an initial idea about the x-, y- and z-position. The second step is a sample with a thin, but dense layer of fluorophores. Optimizing the fluorescence intensity recorded by the detector for this sample usually gives the optimal x- and y-position of the detector, while the z-position might not be optimal yet. To find the optimal z-position for the detector, single emitters that are much smaller than the diffraction limit of ∼250 nm should be imaged, such as gold nanorods, which have, in our case, sizes of about 25 nm by 45 nm. Imaging such small nanorods should result in a diffraction limited Gaussian shaped PSF. The main advantage of using gold nanorods is the fact that gold nanorods are very photostable even under high excitation powers during long illumination times, which makes them ideal targets for alignment.

Once single emitters can be imaged properly, the profile of the measured PSF can be used to verify the quality of the alignment of the excitation beam through the microscope objective.

Finally, the confocal pinhole needs to be aligned. This can be done in a similar manner as the detector. Please be aware that the position of the detector should only be optimized without the confocal pinhole present. If the confocal pinhole is present, the detector will optimized to image the pinhole and not the detection volume.

Figure 2.2 shows a typical area scan of a single gold nanorod using a 15 μm confocal pinhole. The PSF shows a diffraction limited Gaussian intensity profile in both orientations with an average full width at half maximum (FWHM) of about 270 nm, which corresponds to a diffraction limited spot and indicates that the setup is aligned correctly. More importantly, the FWHM is very similar for both the x and y orientations, indicating that the excitation beam is aligned correctly through the microscope objective. An incorrect alignment could show, for example, large differences in FWHM between both orientations, or a PSF with dimensions much larger than the diffraction limit.

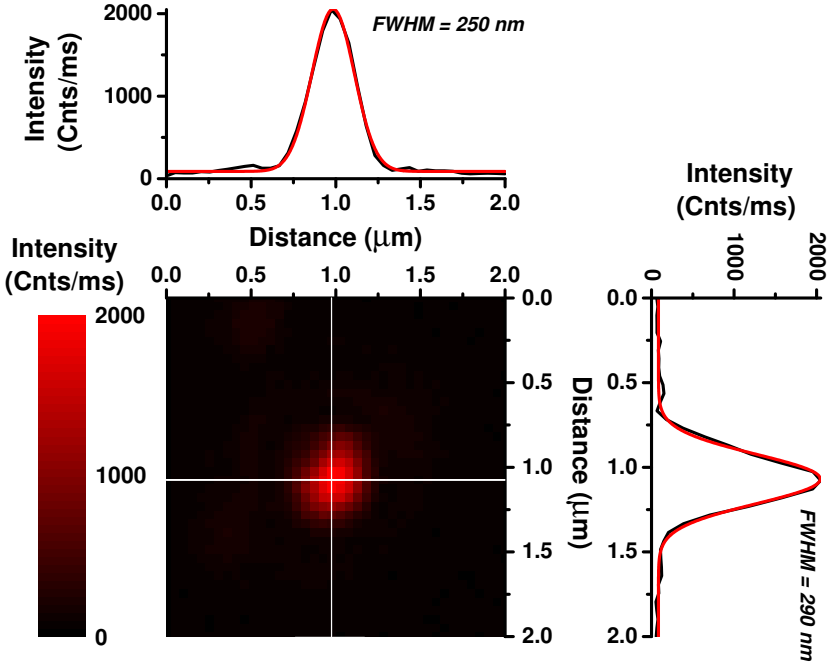

Figure 2.2: Typical fluorescence intensity scan of a single gold nanorod using about 25 kW/cm^2 at 485 nm excitation wavelength. The white lines show the position of the line profiles: top and right graphs.The line profiles (black lines) show that the rod is almost circular and has a diffraction limited Gaussian profile (red lines).

2.4 Photobleaching: the basics

Almost all fluorophores permanently cease to emit after a period of observation. This phenomenon is called photobleaching, which is the irreversible loss of a fluorophore's ability to fluoresce and is the result of the photochemical destruction of the fluorophore. Photobleaching is one of the most intensively studied features of single molecules, since it can provide unique insights into the photophysical properties of the fluorophores themselves [108]. The exact mechanism behind the photochemical destruction of the fluorophore is still unknown and is most likely

different for each fluorophore and depends on the experimental conditions, such as whether the fluorophores are embedded in a matrix or freely diffuse in solution, the temperature, and the excitation powers used [108–111].

However, the presence and diffusion of molecular oxygen in the vicinity of the fluorophore is generally assumed to be the dominant factor in photobleaching [102, 112, 113]. There are two main interactions between oxygen and fluorophores that are thought to result in photobleaching: a direct interaction between singlet oxygen and a fluorophore in the long-lived excited triplet state, or an indirect interaction in which molecular oxygen reacts with radical ions of the fluorophores. Both interactions can result in the photochemical destruction of the fluorophore [102, 113].

It is not possible to directly excite the molecular oxygen to the singlet state when working within the visible wavelength range. However, oxygen can be excited to the singlet state via the energy or electron transfer from fluorophores residing in the excited triplet state. Singlet oxygen is a highly reactive oxygen species with a lifetime of a few microseconds in aqueous solution [114]. Once the singlet oxygen is produced, it can react with a neighboring fluorophore and photo-oxidize it, causing irreversible photobleaching [115].

Radical ions of fluorophores can form by a photo-induced electron transfer to an electron acceptor or from an electron donor [109]. For Rhodamine6G dyes, for example, it was shown that the triplet state acts as an intermediate state in the formation of radical ions [116]. The radical ions typically have very long lifetimes in the millisecond range. Molecular oxygen can then interact with radical ions of the fluorophore also causing irreversible photobleaching.

Regardless of the exact mechanism causing the photochemical destruction of fluorophores, the interaction between a fluorophore in the triplet excited state and oxygen seems to play a key role. Therefore, photobleaching can be reduced by removing as much of the molecular oxygen as possible, although removing oxygen also increases the lifetime of the triplet state of fluorophores and therefore increases the time a fluorophore can react with molecular oxygen to form singlet oxygen. Oxygen can be removed by, for example, exchanging it with nitrogen or by adding an oxygen scavenger system, such as the glucose, glucose oxidase and catalase system, or β-mercaptoethanol [117, 118].

2.4.1 Single-molecule photobleaching

Typically, a fluorophore photobleaches after emitting about 10^5 to 10^6 photons [101, 102], although it has been shown that the photostability of fluorophores strongly depends on the experimental conditions [108, 109]. When observing a single fluorophore, photobleaching generates a discrete, and permanent, step in the fluorescence intensity time trace, see figure 2.3. In the very beginning of the time trace shown in figure 2.3, a single photoblinking event is observed, indicating that indeed a single fluorophore is observed. Photoblinking is the reversible loss of fluorescence, in contrast to photobleaching, which is irreversible.

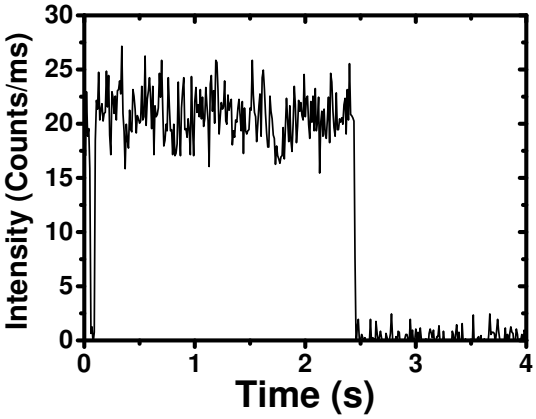

Figure 2.3: Typical intensity time trace showing the photobleaching of a single fluorophore. The dip in the very beginning of the timetrace is blinking event, characteristic for single molecules.

Although the mechanism behind photobleaching is still poorly understood, it can be exploited to obtain information and is very useful in techniques such as fluorescence recovery after photobleaching or single-molecule photobleaching approaches [102].

As we highlighted in the previous chapter, single-molecule photobleaching allows

for direct probing of the aggregation number of αS oligomers without relying on the determination of the molecular mass, a reference, or the need for an extremely high spatial resolution. Single-molecule photobleaching experiments rely on labeling all subunits in the oligomer [99, 100, 119, 120]. The oligomers are then individually analyzed. Sequential photobleaching of all fluorescent labels incorporated into the oligomer will generate discrete steps in the fluorescence intensity. Counting the bleaching steps yields insight into the number of labels in the respective oligomer, and therefore the number of monomers.

2.4.2 Limitations of single-molecule photobleaching approaches

There are, however, limitations to single-molecule photobleaching approaches. One of the main issues with photobleaching is that the number of bleaching steps needs to be determined accurately from a time trace. However, if the aggregate contains too many subunits and therefore too many fluorescent labels, it becomes very difficult to accurately determine the number of bleaching steps, since the intensity time trace will converge to an exponentially decaying curve. For a high fluorophore density, the probability that multiple fluorescent labels photobleach simultaneously or within a very short time of each other also increases significantly.

However, if it can be assumed that all the photobleaching steps originating from single fluorophores result in equal sized bleaching steps, it is possible to extract the step size of a single bleaching event from one of these exponentially decaying time traces and use this to determine the total number of bleaching events from the total fluorescence intensity at the beginning of the time trace [120].

On the other hand, if the fluorophores are immobilized on a surface, as is the case in this thesis, the individual bleaching events do not result in the same fluorescence intensity drop, due to differences in detection efficiencies and excitation efficiencies of the individual fluorophores as a result of differences in their dipole orientation. It is therefore not correct to assume equal step sizes for each bleaching event, making it impossible to distinguish between a single fluorescent label bleaching and multiple fluorescent labels bleaching simultaneously. This makes it impossible to determine the individual bleaching steps from an exponentially decaying intensity time trace.

Therefore, individual bleaching events need to be visible in the time trace. As we will show in the next chapter, the maximum number of bleaching steps that can be accurately determined from an intensity time trace is ∼10. Therefore, the number of monomers forming an oligomer that can be determined with single-molecule photobleaching is also limited to 10.

Furthermore, the fluorophores can influence the oligomer formed by steric hindrance. If there are too many fluorescent labels present, the aggregation process can change, resulting in different oligomers. Therefore, one should be very careful with using too many fluorescent labels to study the aggregation number of oligomers using single-molecule photobleaching.

2.5 Sample preparation for single-molecule photobleaching

To study the oligomers, they need to be immobilized and spatially separated. To realize this, the isolated oligomers were diluted to about 1 nM in HPLC water and directly spincoated for 10 s at 6000 rpm on top of a cleaned coverslip. The samples contained the oligomers at low concentrations, so that the oligomers were well separated and did not overlap within the diffraction limit of the microscope, see figure 2.4.

For single-molecule spectroscopy, it is very important to minimize the fluorescent contaminations in the sample, since even the smallest fluorescent contamination can already be confused with a single or a few fluorophores of specific interest. Starting with a clean substrate is therefore essential.

To obtain a clean substrate, microscope glass coverslips were cleaned by rinsing them first with spectroscopically very pure methanol (Methanol Uvasol, Merck Millipore) to get rid of large contaminations, and subsequently placed in an UV/ozone cleaner (UV/Ozone ProCleaner Plus; Bioforce) for at least one hour to oxidize the contaminations on the surface and hence remove their fluorescence. A typical scan of a cleaned coverslip is shown in figure 2.5.

Figure 2.5 shows that there are only a few contaminations on the cleaned coverslip

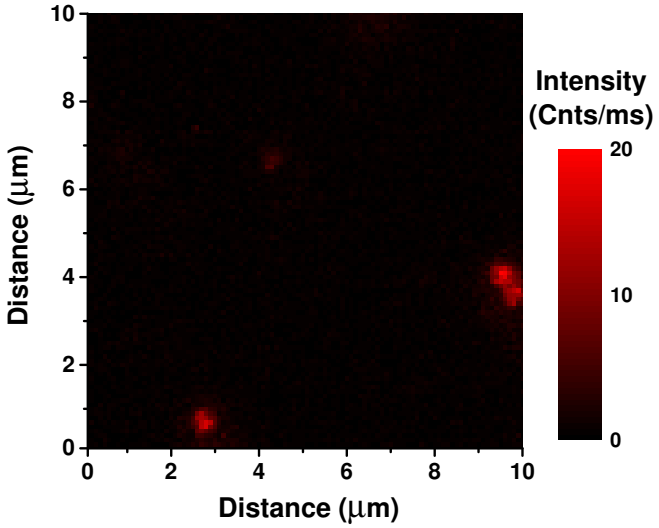

Figure 2.4: Typical area scan of fluorescently labeled αS oligomers spincoated on top of a clean coverslip recorded using an excitation power of ∼750 W/cm^2 at 640 nm excitation wavelength. The scan clearly shows well-separated fluorescence spots. The differences in intensity between the spots are the result of different numbers of fluorescently labeled monomers incorporated into the oligomer due to the stochastic nature of aggregation.

left, about 3-4 per 100 μm^2. The density of these contaminations is much lower than what is typically aimed for with single-molecule spectroscopy, which is about 20 particles per 100 μm^2, see also figure 2.4. Moreover, these contaminations are much dimmer than a typical fluorophore or a typical oligomer, by about a factor of 10, which makes them unlikely to be selected during a measurement.

2.6 Summary

In this chapter, we have discussed the basic requirements for single-molecule detection and described the multipurpose custom-built single-molecule sensitive optical microscope setup that is capable of measuring fluorescence intensities and emission lifetimes at the single-molecule level both *in vitro* and *in vivo*. Optimal alignment of such a microscope is crucial in collecting the maximum signal. We

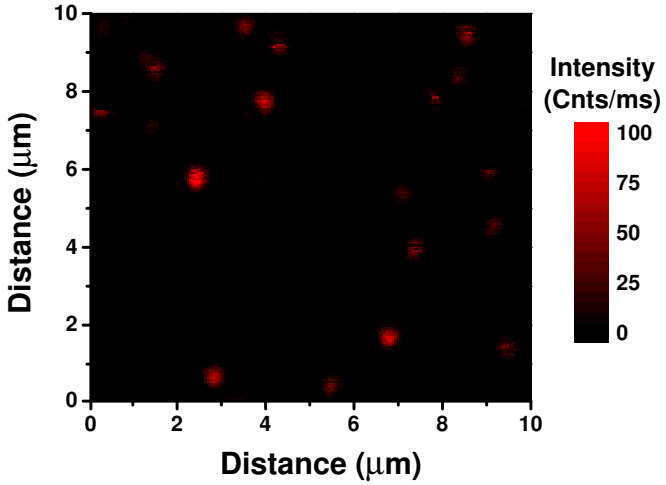

Figure 2.5: Area scan of a microscope coverslip rinsed with methanol and subsequently place in an UV/Ozone cleaner for at least 1 hour. The excitation wavelength was 485 nm at $\sim$2.5 kW/cm^2.

described in short how the optimal alignment can be achieved. We emphasized that single-molecule photobleaching offers an ideal tool to study the aggregation number of αS oligomers and introduced the basic concepts behind this technique and discussed the advantages and disadvantages. Finally, one of the main requirements for single-molecule photobleaching are spectroscopically clean substrates. Cleaning substrates can be an elaborate procedure, but in this chapter we discussed a simple method that results in clean substrates suitable for single-molecule detection.

Chapter 3

Aggregation number of sub-stoichiometrically labeled α-Synuclein oligomers determined by single-molecule photobleaching*

3.1 Introduction

As we emphasized in the previous chapters, single-molecule photobleaching is a very suitable technique to directly probe the aggregation number of protein aggregates without relying on the determination of the molecular mass, a reference, or the need for an extremely high spatial resolution. Conventional single-molecule photobleaching experiments use 100% fluorescently labeled aggregates, that is, all monomeric subunits contain a fluorescent label [99, 100, 121]. In this chapter,

* This chapter has been published as:
N. Zijlstra, C. Blum, I.M.J. Segers-Nolten, M.M.A.E. Claessens, and V. Subramaniam, *Molecular composition of sub-stoichiometrically labeled α-Synuclein oligomers determined by single-molecule photobleaching*, Angewandte Chemie IE **51** (35): pp. 8821-8824 (2012).

we study the aggregation number of α-Synuclein (αS) oligomers prepared using an aggregation protocol based on high αS concentrations and long incubation times (for details on the aggregation protocol, see the Materials and Methods).

3.1.1 Single-molecule photobleaching on 100% labeled αS oligomers

Figure 3.1 shows a typical intensity time trace obtained for an individual αS oligomer in which all monomeric subunits are fluorescently labeled. A thin polyvinylalcohol (PVA) layer containing the oligomers at low densities, approximately 1 oligomer per about 2.5 x 2.5 μm^2, was spincoated on top of a glass microscope cover slip to spatially separate and immobilize the oligomers (for more details on the sample preparation see Materials and Methods). The bleaching traces were recorded using a custom-built confocal microscope (see chapter 2 and the Materials and Methods for details). By embedding the oligomers in a PVA matrix, the fluorophores will not be able to rotate freely which will influence both the excitation and detection efficiency. However, it has been shown that the largest difference between the most efficient and least efficient orientation is a factor of $\sim$3 in detected fluorescence intensity for a high NA objective as used in our experiments [122]. This difference will only influence the step size, and not the number of bleaching steps observed.

The intensity timetrace in figure 3.1 does not show discrete steps in the fluorescence intensity, as we would expect for single-molecule photobleaching. The reason for the exponentially decaying trend is that the αS oligomers consist of a large number of monomers, as we will later show about 30 monomers, and hence contain a large number of fluorescent labels. Especially the first part of the timetrace makes it difficult to determine the number of bleaching steps accurately. Most of the fluorescent labels photobleach within a short time, that is, within less than a few seconds. Therefore, there is a high probability that multiple labels bleach simultaneously or within a very short time of each other, making it impossible to determine the individual bleaching steps.

To verify that one fluorescent label gives a single bleaching step, we also analyzed the bleaching behaviour of labeled αS monomers. These studies showed the expected

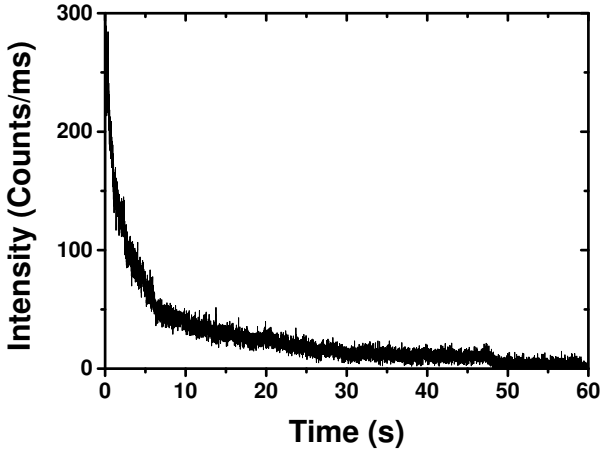

Figure 3.1: Typical intensity time trace for 100% labeled oligomers. The background has been subtracted. Accurate determination of the number of bleaching steps is not possible.

typical one step bleaching, see figure 3.2, confirming the presence of a single fluorescent label on the monomer and excluding any effects arising from dye/protein or dye/matrix interaction giving rise to multiple step intensity decreases. Therefore, we conclude that the 100% labeled αS oligomers indeed consist of a large number of monomers, which are not distinguishable by photobleaching.

3.1.2 Sub-stoichiometric labeling

Accurate determination of the number of bleaching steps for 100% labeled oligomers is not possible, since the oligomer contains too many fluorescent labels. Additionally, the presence of a large number of fluorescent labels may influence the aggregation process and result in a different oligomeric species. To overcome these limitations and problems, we have extended the single-molecule photobleaching method to be used in combination with sub-stoichiometric labeling, or underlabeling. In this approach, only a fraction of the monomers contain a fluorescent label, see figure 3.3.

The aggregation of a mixture of labeled and unlabeled monomers is a stochastic process. Therefore, aggregating a mixture of labeled and unlabeled monomers will

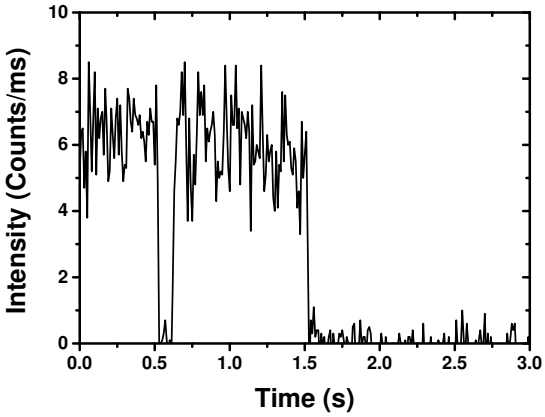

Figure 3.2: Typical background subtracted intensity time trace for fluorescently labeled αS monomers immobilized in a PVA matrix. The time trace clearly shows single step photobleaching, indicating that αS monomers indeed contain a single fluorescent label and excluding any untoward protein/dye or matrix/dye interactions giving rise to multiple step intensity decrease.

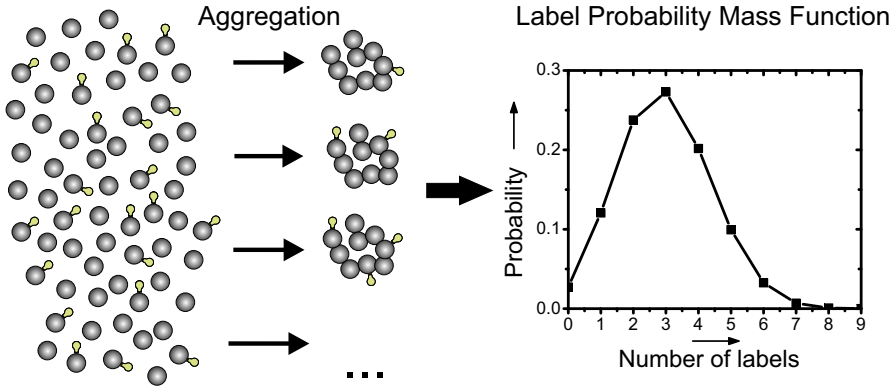

Figure 3.3: During the aggregation process, the incorporation of labeled monomers in the oligomer is a stochastic process. Therefore, the number of labels can vary between zero and the total number of monomers per oligomer. Using the stochastic nature, one can predict the discrete label probability mass function and link the number of fluorescent labels to the total number of monomers, labeled and unlabeled.

result in a distribution in the number of fluorescently labeled monomers per oligomer, even for homogeneous oligomers of the same aggregation number, see figure 3.3. The stochastic incorporation of either labeled or unlabeled monomers into the oligomer is described by a classical Bernoulli process in which there is no preference for either the labeled or the unlabeled monomers. If the label density, that is, the percentage of fluorescently labeled monomers, at the start of the aggregation is known, the probability that an oligomer with a defined number of monomers contains a specific number of labels can be predicted. This probability is called the label probability mass function (PMF) and is calculated using a binomial distribution. In principle, the number of labels can vary between zero and the total number of monomers in an oligomer. Therefore, the observed number of bleaching steps determined for a large number of underlabeled single oligomers will always show a distribution.

Hence, in contrast to conventional photobleaching experiments using 100% labeling, the bleaching trace of one oligomer in our experiment, where we use underlabeling, will not directly yield any information about the number of monomers forming the oligomer. When using underlabeling, it is essential to count the bleaching steps for a statistically relevant number of oligomers to determine the distribution of the number of labels in the oligomers. This distribution then is linked to the total number of monomers, labeled and unlabeled, in the oligomer via the label PMF. By using different label densities, it is even possible to investigate the influence of fluorescent labels on the aggregation process.

The histogram of bleaching steps for a single well-defined oligomeric species is fully explained by the label PMF for a fixed number of monomers per oligomer. Any broadening of the histogram of bleaching steps compared to the label PMF must originate from a distribution in the number of monomers per oligomer. This broadening can be directly accessed by comparing the measured histogram of bleaching steps with the label PMF for a fixed number of monomers per oligomer to obtain information about any distribution in the number of monomers per oligomer. As we will show in the next chapter, it is also possible to obtain multiple species from a single histogram of bleaching steps.

3.2 Results and discussion

Fluorescently labeled αS oligomers were prepared with different label densities, namely 7.5%, 15%, 20%, and 30%, according to the protocol based on high protein concentrations and long incubation times as described in the Materials and Methods section. Since wild-type αS does not contain a cysteine residue required for labeling, we used the A140C mutant with Alexa Fluor 488 as fluorescent label. After the aggregation, the oligomers were purified using a gel filtration column to separate non-aggregated monomers from oligomers. The oligomeric species were spread over four elution fractions. A typical elution profile for a 7.5% label density is shown in figure 3.4.

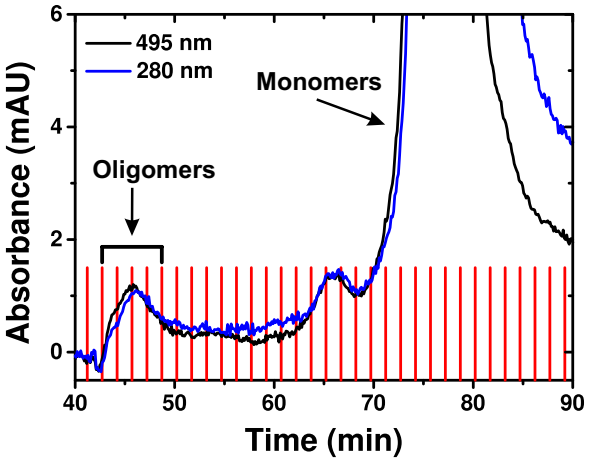

Figure 3.4: Typical elution profile measured for the absorbance at 495 nm (black line), representing the fluorescent label absorbance, and at 280 nm (blue line), representing the protein absorbance. The red lines indicate the corresponding fractions. The elution profile is for oligomers with a 7.5% label density. Indicated are the monomer peak and the specific oligomer peak that is the object of study in this chapter and in our previous work [53, 94, 123, 124].

3.2.1 Analyzing time traces

For sub-stoichiometrically labeled oligomers, in contrast to 100% labeled oligomers, sequential photobleaching of all the fluorescent labels in an oligomer does result in discrete steps in the fluorescence intensity, see figure 3.5. The number of fluorescent labels present in each oligomer was determined by counting the number of bleaching steps for each time trace. The analysis of a complex time trace with 10 bleaching steps is shown in figure 3.6. For each label density and analyzed elution fraction, we recorded bleaching traces from a minimum of 100 distinct oligomers.

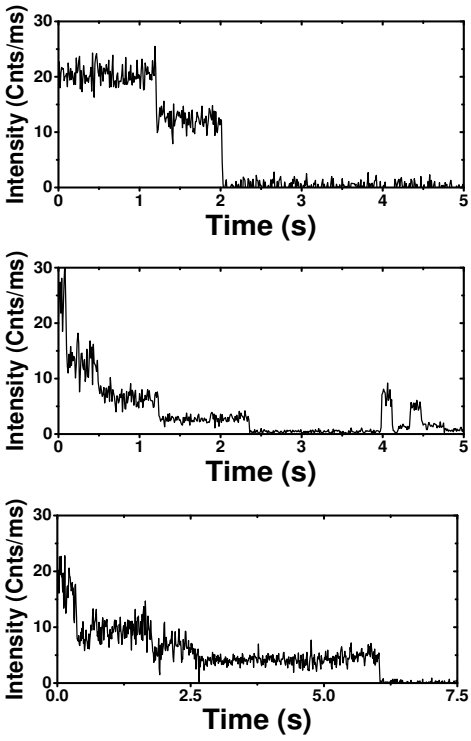

Figure 3.5: Three typical time traces with increasing number of bleaching steps. Top graph shows 2 step bleaching, middle graph 4 step bleaching, and bottom graph 5 step bleaching. The intensity is background subtracted.

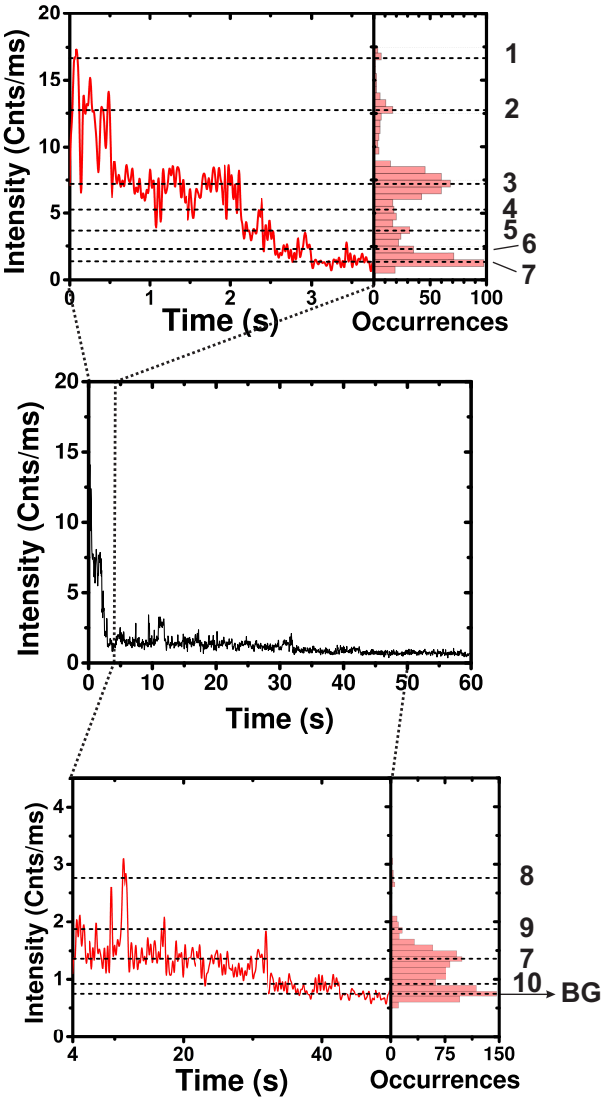

Figure 3.6: A complex time trace showing 10 bleaching steps. From the overall intensity time trace (center figure) it is not possible to determine the number of bleaching steps. Zooming in on the first 3.5 seconds and plotting the photon counting histogram allows us to determine the number of bleaching steps (top figure). The same procedure is followed for the second part of the time trace (bottom figure). Intensity level 7 is present in both the first and the second part of the time trace. BG indicates the background level, which is 0.7 counts/ms.

3.2.2 Interpreting the histograms of bleaching steps

To verify that the spread of the oligomers over four elution fractions was solely due to a broadening inherent to the column used and not due to differences in oligomers (and with it aggregation numbers), we determined the histograms of bleaching steps for outer elution fractions for the 15% label density, see figure 3.7. We fitted both histograms with a binomial distribution from which we determined the number of monomers per oligomer, see figure 3.7 solid lines. For both the first and the last fraction, we found an aggregation number of 31 monomers per oligomer.

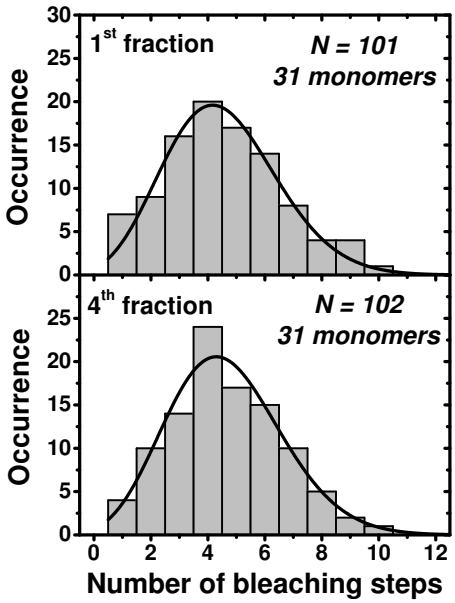

Figure 3.7: Histogram of the number of bleaching steps observed for the oligomers with a 15% label density from the 1st (top) and 4th (bottom) fraction from the size exclusion column. The histograms are fitted with a binomial distribution (solid lines) from which we determined number of monomers per oligomer. N gives the number of photobleaching traces of distinct oligomers analyzed.

Since the aggregation numbers found for the first and last fraction are the same, we chose to use the center fraction, containing the highest oligomer concentration, for all other label densities. We then obtained a histogram of bleaching steps for each of the label densities by counting the number of photobleaching steps for at least 100 distinct oligomers per label density. Figure 3.8 shows the photobleaching histograms for the 7.5%, 15%, 20%, and 30% label densities. The histograms show the expected shift from an average of about 2 bleaching steps to an average of about 7 bleaching steps with increasing label density.

The bleaching histogram for each label density was fitted with a binomial distribution and for each label density we determined the mean number of labels per oligomer (figure 3.8, solid lines). The mean number of monomers is given by the average number of fluorescent labels multiplied by the label density. Since the width of the distribution is a result of the stochastic nature of the incorporation of labeled monomers, it does not describe the uncertainty in the aggregation number. To address this uncertainty, we used simulations to determine the accuracy with which we can determine the aggregation number of these oligomers when using the combination of single-molecule photobleaching and sub-stoichiometric labeling, see chapter 5. We show in chapter 5 that for a 30-mer, when working within the optimal range of label densities, it is possible to determine the aggregation number with an accuracy of ± 3 monomers per oligomer, including possible errors made due to errors in determining the labeling efficiency. Since we show below that the 30% label density is not within the optimal range of label densities anymore, the uncertainty in the aggregation number is larger. Using the exact label density and the accuracies determined for 30-mers in chapter 5, the mean number of monomers per oligomer is determined at 31 ± 3 (7.5%), 32 ± 3 (15%), 30 ± 3 (20%), and 25 ± 4 (30%), see table 3.1. The number of monomers that form an oligomer for the 7.5%, 15%, and 20% label densities is remarkably uniform.

Within the error bars, there is no variation in the number of monomers that form an oligomer, indicating that the number, or fraction, of labeled monomers does not influence the aggregation process. Furthermore, this small variation within the error bars shows that the incorporation of labeled monomers during the aggregation process is indeed a truly stochastic process. If the process is not truly stochastic, one would

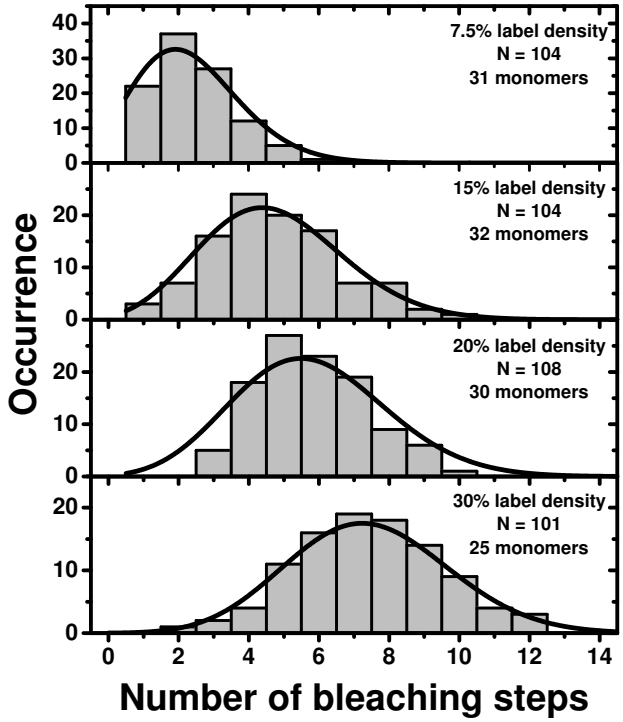

Figure 3.8: Histogram of the number of bleaching steps observed for the oligomers with 7.5%, 15%, 20%, and 30% label density. The histograms are fitted with a Poisson distribution (solid line). The mean of the binomial distributions give the average number of labels incorporated into the oligomer.

expect a systematic increase or decrease in the number of monomers per oligomer with the label density, reflecting a preference for incorporating a labeled or unlabeled monomer.

As was outlined above, any broadening of the histogram of bleaching steps compared to the binomial fit must originate from a distribution in the number of monomers per oligomer. As can be seen in figure 3.8, the total widths of all four of the measured histograms are fully explained by the widths of the binomial fits. This implies that the oligomers are present as a single species with homogeneous aggregation number, which is the key finding in this chapter.

Table 3.1: Aggregation number found for each of the label densities including the accuracies determined in chapter 5.

Label density	Aggregation number
7.5%	31 ± 3
15%	32 ± 3
20%	30 ± 3
30%	25 ± 4

The deviation that we observe in the 30% label density clearly shows the limitations of the photobleaching technique. We see different effects that can contribute to an imprecise determination of the distribution of the number of labels in the oligomers. Brighter oligomers are imaged as brighter spots in the area scan and make the less bright oligomers less visible. As a consequence, the brighter oligomers are inadvertently selected more often, which would result in seemingly larger oligomers since bright oligomers contain more fluorescent labels. However, for an oligomer containing a larger number of fluorescent labels it is more likely that the number of bleaching steps is underestimated since the probability that two fluorophores bleach within a very short time increases. We believe that this effect resulting in an underestimation of the number of labels in our case outweighs the apparent increase of the number of labels due to choosing brighter oligomers. Since this limitation already arises with the underlabeling approach used here, it is obvious that conventional photobleaching with 100% labeling is not suitable for large aggregates, as we have also shown in figure 3.1 for 100% labeled αS oligomers. Finally, the variation we find for 30% labeling density might also be an indication that the density of the fluorescent label starts to have an influence on the aggregation.

To check whether the results are reproducible, we repeated the experiment with the 7.5% label density. We found for both batches the same number of monomers per oligomer. Since the fluorescent label itself can also influence the aggregation process,

we also checked reproducibility using a different fluorescent label and therefore prepared two separate batches of oligomers labeled at 15% label density with a different fluorescent label, namely Alexa Fluor 488 and Atto 488, and compared both histograms. We found no difference, and can therefore conclude that the labels used at position 140 of the amino acid sequence of αS do not influence the aggregation.

3.3 Conclusions and discussion

In conclusion, we have developed a new method using single-molecule photobleaching in combination with sub-stoichiometric labeling that allows us to analyze large macromolecular protein assemblies. We can determine the aggregation number, probe the distribution in the number of monomers per oligomer, and investigate the influence of the fluorescent label on the aggregation process.

We find no distribution in the number of monomers per oligomer and find a single, well-defined αS oligomeric species consisting of 31 monomers per oligomer. This result is in good agreement with a recently performed SAXS study on oligomers formed under similar conditions in which the aggregation number was determined to be about 30 monomers per oligomer [81]. Additionally, we showed that for αS aggregation the fluorescent labels used do not have an influence.

In chapter 1, we discussed that van Rooijen *et al.* showed that αS oligomers are composed of a solvent-shielded core consisting of about the first 100 residues of the amino acid sequence and a solvent-exposed C-terminus [53], see figure 3.9 for a schematic representation of the possible global structure of an oligomer. No spectral broadening of the emission spectra of Tryptophan was observed, implying a homogeneous structure for all oligomers. These results in combination with our finding that the oligomers are formed of a defined number of monomers, implies the oligomers formed under the specific aggregation conditions used organize in a stable structure.
However, previous studies in literature showed differences in αS oligomers, but the origin of these differences is unclear. The variations in oligomer characteristics may reflect a combination of conformational and structural differences rather than specific aggregation numbers, i.e. specific numbers of monomers per oligomer.

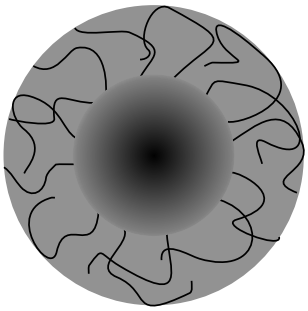

Figure 3.9: Schematic representation of the possible global structure of an αS oligomer derived from the Tryptophan measurements. The αS oligomers have a dense solvent-shielded core consisting of about the first 100 residues of the amino acid sequence. The outer shell that consists of the C-terminus has a much less dense structure and is solvent-exposed.

3.4 Materials and methods

3.4.1 αS preparation, labeling, and aggregation

Expression and purification of αS wild-type and mutant αS A140C was performed as previously published [125]. Prior to labeling, αS A140C in 10 mM Tris-HCl, 5 mM NaCl, pH7.4 was reduced with a six-fold molar excess of dithiothreitol (DTT) for 30 minutes at room temperature. The samples were desalted using a Pierce Zeba desalting column. A two-fold molar excess of Alexa Fluor 488 C5 maleimide (Invitrogen) was added and incubated for one hour in the dark at room temperature. Free label was removed using two consecutive desalting steps. The labeling efficiency was determined from the absorption spectrum. The protein concentration was determined from the absorbance at 276 nm using an extinction coefficient of 5745 M^{-1} cm^{-1} and the Alexa Fluor 488 concentration from the absorbance at 495 nm using an extinction coefficient of 72000 M^{-1} cm^{-1}. Subsequently, αS wild-type in 10 mM Tris-HCl, pH7.4 was added to the labeled αS A140C to obtain the desired ratio between wild-type and A140C. To prepare the αS oligomers, we followed the protocol described in [94], which also shows a typical elution profile and a native

gradient PAGE gel with a polyacrylamide gradient from 3% to 17%, indicating that these species migrate concomitantly with the molecular weight marker ferritin of ∼450 kDa. In short, the mixture of labeled and wild-type αS was dried in a vacuum evaporator and dissolved using HPLC water at a final protein concentration of 1 mM in 40 mM Tris-HCl, pH7.4. The solution was incubated in an Eppendorf thermo mixer for 18 hours at room temperature with shaking at 1250 rpm and subsequently for 2 hours at 37 °C without shaking. The oligomers were purified by size-exclusion chromatography on a Superdex200 gel filtration column using 10 mM Tris-HCl, 50 mM NaCl, pH7.4 as eluent. The fractions containing the αS oligomers were identified by the 495 nm absorbance.

3.4.2 Sample preparation

Microscope glass coverslips were cleaned by placing them for at least three days in 65% nitric acid to oxidize contaminations on the surface and hence minimize their fluorscence. Subsequently, the coverslips were rinsed with HPLC water and HPLC methanol, and then dried passively. To study the oligomers, they need to be immobilized. To realize this, the already formed oligomers were diluted to about 1 nM in 2% (w/v) PVA dissolved in HPLC water. Fluorescence correlation spectroscopy measurements do not show a change in diffusion time of the oligomers upon dilution, indicating that the oligomers are stable on the time scale of our experiment [6]. The oligomer-PVA solution was spincoated for 10 s at 6000 rpm on top of a cleaned coverslip, resulting in a thin layer of PVA in which the oligomers were embedded. The samples contained the oligomers at low concentrations, so that the oligomers were well separated and did not overlap within the diffraction limit of the microscope.

3.4.3 Instrumentation and measurement procedure

The photobleaching experiments were performed using a custom-built inverted confocal microscope as described in chapter 2. In short, as excitation source, we used a pulsed diode laser operating at 485 nm at a repetition rate of 20 MHz (LDH-D-C-485, Picoquant). An epi-illumination configuration was used, i.e., the illumination and emission collection are through the same microscope objective (UPLSAPO 60XW,

60X, 1.2NA, Olympus). The remaining excitation light in the detection path was suppressed with a long pass filter (RazorEdge, 488 nm, Semrock) and an additional notch filter (Stopline, 488/14 nm, Semrock). The emission was spatially filtered using a 50 μm pinhole and was subsequently focused onto a single photon avalanche diode (SPCM-APQR-16, PerkinElmer), connected to a photon counting module (PicoHarp300, Picoquant). The initial scanning of the sample was done at a high scanning speed, 2 ms per pixel, and low excitation powers, $\sim$200 W/cm^2, to minimize dye bleaching. We then located individual oligomers in the initial scan, localized them in the focus of the objective, and sequentially collected fluorescence intensity time traces from distinct oligomers. For the time trace we used higher excitation powers, $\sim$800 W/cm^2, to make sure that each dye molecule photobleached within 90 seconds.

Chapter 4

Elucidating the aggregation number of dopamine-induced α-Synuclein oligomeric assemblies*

4.1 Introduction

As we discussed in chapter 1, there are indications that the formation of α-Synuclein (αS) oligomers directly depends on the aggregation conditions [51, 58, 63, 64, 94]. However, one of the main questions is whether there are similarities between oligomers formed under different aggregation conditions and whether there is a specific cytotoxic oligomeric species or if oligomers in general cause cell death. Unfortunately, structural and biophysical information on the different oligomers is scarce.

In chapter 3, we studied the aggregation number of αS oligomers formed under

* This chapter has been published as:
N. Zijlstra, M.M.A.E. Claessens, C. Blum, and V. Subramaniam, *Elucidating the aggregation number of dopamine-induced α-Synuclein oligomeric assemblies*, Biophysical Journal **106**: pp. 440-446 (2014).

high protein concentrations during long incubation times. However, this is only one of many protocols used to form αS oligomers *in vitro*. To be able to identify similarities between oligomers, it is therefore important to investigate αS oligomers formed under different aggregation conditions.

αS oligomers formed in the presence of dopamine are of special interest because the selective loss of dopaminergic neurons suggests that dopamine might play a role in the formation of cytotoxic αS oligomers. Previous studies by Conway *et al.* showed that the addition of dopamine can stabilize αS oligomers preventing them from maturing into fibrils [126]. Cappai *et al.* showed that dopamine accelerates the formation of non-amyloidogenic, SDS-resistant αS oligomers [58]. A range of biophysical techniques has been used to study the morphology of dopamine-induced oligomers, indicating a variety of different shapes and sizes [58, 59, 126], without providing insights into the exact aggregation number of these oligomers.

In this chapter, we study the aggregation number of dopamine-induced αS oligomers using the same combination of single-molecule photobleaching and sub-stoichiometric labeling described in the previous chapter. Additionally, we investigate the aggregation number of αS oligomers formed under the same conditions as the dopamine-induced oligomers, that is short incubation times and low protein concentrations, but now in the absence of dopamine.

4.2 Results and Discussion

4.2.1 The single species approach

To study the aggregation number of dopamine-induced αS oligomers, we prepared Alexa Fluor 647 fluorescently labeled dopamine-induced oligomers with different label densities and analyzed bleaching traces for a minimum of 100 distinct oligomers per label density. A detailed description of the aggregation protocol can be found in the Materials and Methods section. In short, a mixture of 140 μM αS protein and 200 μM dopamine in 10 mM Phosphate buffer, pH7.4, was incubated for 3 hours at 37 °C. In the previous chapter, we showed that the fluorescent label at position 140 of the amino acid sequence does not influence the aggregation process by checking

multiple different fluorescent labels and a range of different label densities. Therefore, we chose to use the same labeling position in this study. Additionally, to verify the stochastic incorporation of labeled αS into the dopamine-induced oligomers, we compared the elution profiles of wild-type oligomers without fluorescent labels and the Alexa Fluor 647 labeled oligomers. We observe no difference in the peak position of the elution profile, and therefore conclude that the fluorescent label does not influence the aggregation process, see figure 4.1. The differences in profile shape observed are well within the differences observed between multiple preparations using this aggregation protocol to prepare dopamine-induced oligomers.

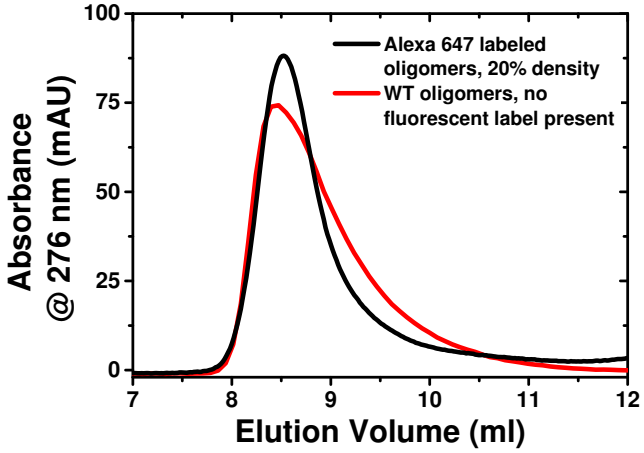

Figure 4.1: Zoom of the oligomeric peak within elution profiles of Alexa Fluor 647 labeled oligomers (black solid line) and wild-type oligomers containing no fluorescent label (cyan solid line) measured for the protein absorbance at 276 nm. The elution profile shows that both oligomer batches are eluting at the same volume, indicating that both oligomers are the same and that the fluorescent label does not influence the aggregation.

Figure 4.2 shows the photobleaching histogram for dopamine-induced αS oligomers with a 20% label density derived from bleaching traces analyzed for 105 distinct oligomers. As was discussed in chapter 3, the stochastic incorporation of labeled monomers in the oligomers is described by a classical Bernoulli process in which there

is no preference for either labeled or unlabeled monomers. Assuming there is only a single species of oligomers present as seen in chapter 3, the bleaching histogram was fitted with a single binomial distribution from which the average number of monomers per oligomer was determined as 21 (see figure 4.2, blue dash-dotted line). This aggregation number does contain interesting information: it already indicates that these oligomers are clearly smaller than the oligomers we studied in the previous chapter. The fit, however, does not represent the data well. The histogram has a significantly lower peak value compared to the fit and displays a clear broadening, especially on the right side of the histogram. As can be seen in figure 4.2, the fit might even be overestimating the aggregation number, since the peak position of the fit is at a higher number of bleaching steps compared to the peak of the histogram.

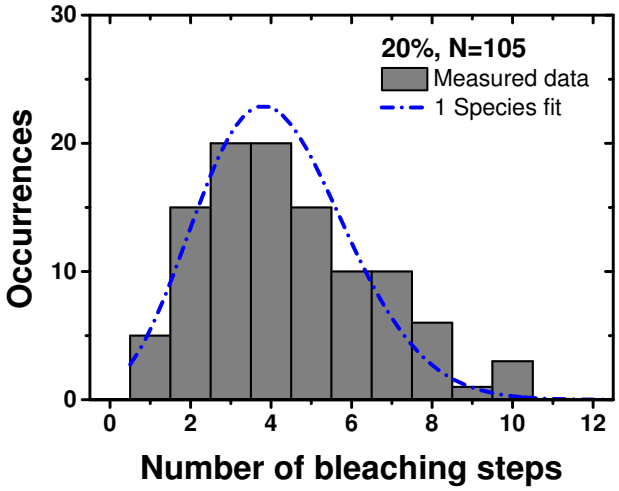

Figure 4.2: Experimental histogram of bleaching steps for dopamine-induced oligomers with a 20% label density built from bleaching traces of 105 distinct oligomers. The histogram is fitted with a single binomial distribution (blue dash-dotted line) that does not appear to represent the measured distribution accurately.

4.2.2 Multiple distinct species present in the same sample

The difference between the measured distribution and the fit is much larger than we observed in the previous chapter for oligomers present in a single, well-defined species. Clearly, if the oligomers are present in multiple species instead of a single species, the distribution of bleaching steps will change significantly, see figure 4.3.

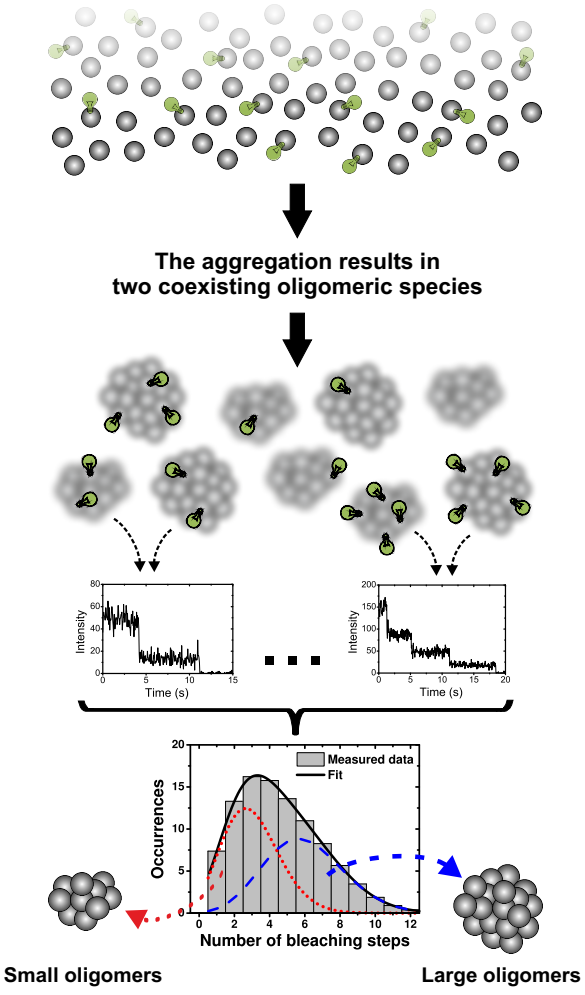

Figure 4.3: Single molecule photobleaching on sub-stoichiometrically labeled oligomers in the case that the aggregation results in two coexisting oligomeric species instead of a single species. Using a sub-stoichiometric mixture of fluorescently labeled and unlabeled monomers for aggregation will result in oligomers containing different numbers of fluorescently labeled monomers. Counting the number of bleaching steps for a statistically relevant number of oligomers will result in a distribution of bleaching steps that can be linked to the total number of monomers per oligomer via the label density chosen at the initiation of aggregation and the label PMF. If oligomers of different aggregation numbers are present, the measured histogram of bleaching steps will consist of the sum of binomial distributions. By fitting the appropriate number of species, it is possible to obtain the aggregation number of multiple species from a single histogram of bleaching steps.

The histogram of bleaching steps will then consist of the sum of multiple binomial distributions instead of a single binomial distribution, given by:

$$\sum_{i=1}^{s} A_i \cdot \begin{pmatrix} n_i \\ k \end{pmatrix} \cdot p^k \cdot (1-p)^{n_i - k} \tag{4.1}$$

where A_i is the total number of analyzed oligomers for species i with aggregation number n_i, s is the total number of species, k the number of fluorescent labels, and p is the label density.

To test whether we can discriminate multiple species present in the same sample from a single histogram of bleaching steps, we simulated a histogram of bleaching steps for a mixture of two oligomeric species consisting of 20 and 35 monomers per oligomer with a 15% labeling density, see figure 4.4. As a consequence, a single species fit cannot adequately reconstruct the histogram of bleaching steps, as is also indicated by the low fit quality (see figure 4.4, black dash-dotted line for single species fit). The fit quality is characterized by the reduced chi-squared parameter χ^2_{red} (see equation 4.5), which was determined for the single species fit as 1.6. Compared to the single species fit, the simulated histogram is clearly broadened, especially on the right side of the histogram, and has a lower peak value compared to the fit. The simulated histogram, however, can be adequately explained if a sum of multiple binomial distributions is fitted (see figure 4.4, red solid line), which is also reflected by the χ^2_{red} of this fit of 1. Moreover, this result indicates that it is possible to obtain the aggregation number of multiple species from a single histogram of bleaching steps.

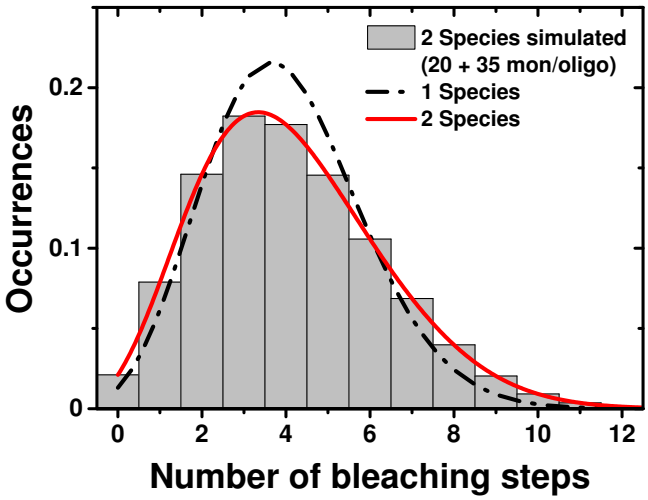

Figure 4.4: Simulated histogram of bleaching steps for a mixture of two oligomeric species consisting of 20 and 35 monomers per oligomer with a 15% labeling density and present in equal fractions. The histogram is clearly broadened and has a lower peak value compared to the single species fit (dash-dotted black line), while a two species fit fully explains both the width and the height of the histogram.

For the single species fit of the experimental data corresponding to a 20% label density, we observe discrepancies similar to those seen for the single species fit of the simulated histogram, suggesting that the dopamine-induced oligomers are composed of more than one species. A two species fit of the experimental histogram of bleaching steps for the oligomers with 20% label density greatly improved the fit quality (figure 4.5, red solid line and table 4.1)), where both the peak height and the width of the histogram are now fitted well. Adding a third species (figure 4.5, black squares), the algorithm finds two essentially identical species (17 and 18 monomers per oligomer), while the third species contains 32 monomers per oligomer. However, the three species fit has a reduced fit quality compared to the two species fit, indicating that two distinct oligomeric species are sufficient to explain the data (see table 4.1).

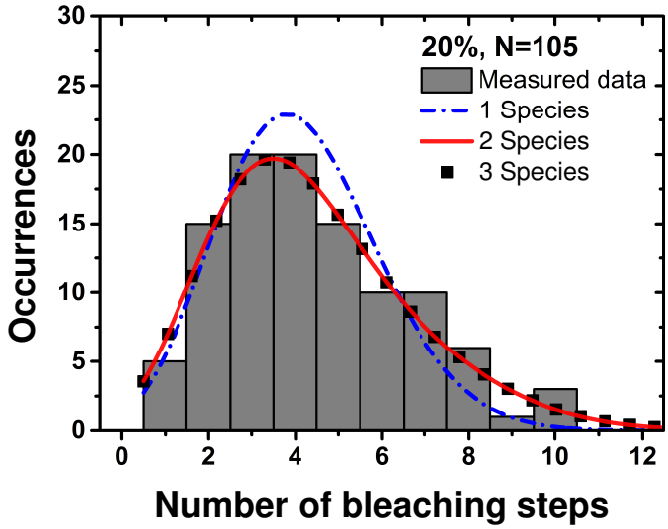

Figure 4.5: Experimental histogram of bleaching steps for dopamine-induced oligomers with a 20% label density built from bleaching traces of 105 distinct oligomers. The histogram is fitted with a single binomial distribution (blue dash-dotted line), a combination of two (solid red line) and three (black squares) binomial distributions. The fit quality greatly improved with the two species fit, while the three species fit yields a reduced fit quality.

Table 4.1: Reduced chi-squared parameter χ^2_{red} for the one, two, and three species fit and corresponding aggregation number of the oligomers.

	χ^2_{red}	**Aggregation number**
1 species	4.8	21
2 species	2.1	17/31
3 species	2.6	17/18/32

4.2.2.1 Multiple distinct oligomeric species formed under high protein concentrations and long incubation times?

The two species observed for dopamine-induced oligomers is a fundamentally different result than what we found in the previous chapter for αS oligomers prepared using a different protocol based on a high αS concentration and long incubation times. For these oligomers, we found a single, well-defined species of oligomers. To check whether these oligomers are indeed present as a single species, we fitted the histogram of bleaching steps obtained for these oligomers with a 15% label density with both a single species and two species, see figure 4.6. Both fits give exactly the same aggregation number of 32 monomers per oligomer with the two species fit having a worse reduced chi-squared parameter, namely 3.3 for the one species fit compared to 4.6 for the two species fit. The oligomers formed under high protein concentrations during long incubation times studied in the chapter 3 are indeed present as a single, well-defined species.

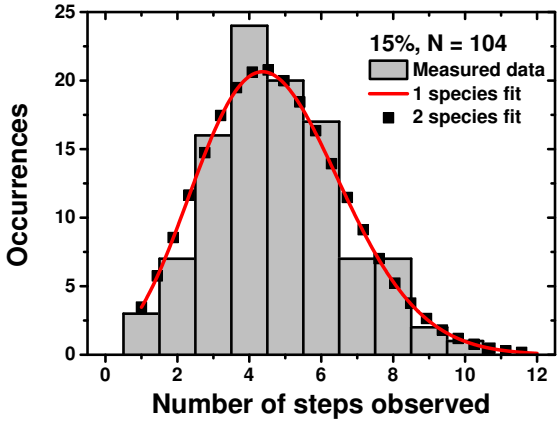

Figure 4.6: The histogram of bleaching steps for the 15% label density as obtained in the previous chapter for oligomers formed under high concentration of αS and during long incubation times. The histogram is fitted with both a single species (solid red line) and two species (black squares). For these oligomers, both fits are clearly identical and also give the same aggregation number of 32 monomers per oligomer. Additionally, the two species fit has a worse χ^2_{red}, indicating that these oligomers are indeed present as a single species.

4.2.3 Continuous distribution of oligomer species

Instead of a defined double species, one could also imagine that the dopamine-induced oligomers are present as a continuous distribution of oligomeric species around a central aggregation number, see equation (4.3) in the Materials and Methods. To test this hypothesis, we fitted the histogram of bleaching steps for the dopamine-induced oligomers with a 20% label density with continuously distributed aggregation numbers with varying widths of the distribution, see figure 4.7. For the distribution, we used normal, Gaussian distributed aggregation numbers, since this represents a random variation in aggregation numbers best.

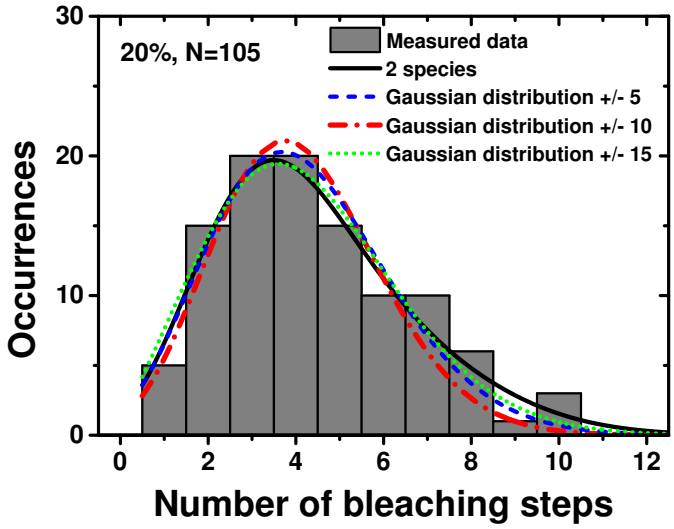

Figure 4.7: Experimental histogram of bleaching steps for dopamine-induced oligomers with a 20% label density built from bleaching traces of 105 distinct oligomers. The histogram is fitted with a combination of two binomials (solid black line), and with continuously distributed binomials with different widths of the distribution: ±5 (blue dashed line), ±10 (red dash-dotted line), and ±15 (green dotted line) monomers per oligomer.

As can be seen in figure 4.7 and table 4.2, fitting a narrow Gaussian distribution

with ±5 monomers per oligomer does not improve the fit quality compared to the two species fit. Broadening the Gaussian distribution more to ±10 monomers per oligomer, improves the fit quality significantly. However, making the Gaussian distribution even broader, ±15 monomers per oligomer, decreases the fit quality again (table 4.2). The best fit quality obtained by fitting Gaussian distributed aggregation numbers, namely a χ^2_{red} of 2.6 for a distribution width of ±10 monomers per oligomer, is still worse than the fit quality obtained for the two species fit. We therefore conclude that two distinct oligomeric species are sufficient to explain the data fully and chose to use the two species model that has the fewest fitting parameters to avoid overfitting the data.

Table 4.2: Reduced chi-squared parameter χ^2_{red} for the two species fit and fits using Gaussian distribution aggregation numbers.

	χ^2_{red}	**Aggregation number**
2 species	2.1	17/31
±5 mon/oligo	3.9	20
±10 mon/oligo	2.6	21
±15 mon/oligo	3.0	21

4.2.4 Determining the optimal label density

As was already outlined in the previous chapter, when using the combination of single-molecule photobleaching and sub-stoichiometric labeling, it is very important to use label densities for which the technique works optimally. Difficulties arise when using a label density that is either too low or too high. Choosing the appropriate label density becomes even more important if the oligomers are present in multiple species.

Since both species have a different aggregation number, the label density has to be chosen in such a way that both aggregation numbers can be determined accurately.

To determine the optimal label density, the following has to be considered for both species. When using a lower label density, an increasing fraction of the oligomers will not contain a fluorescent label due to the stochastic nature of aggregation and are therefore invisible to this method. Because this fraction cannot be measured, it is not included in the histogram and will cause an uncertainty in the fitting. The larger the fraction of oligomers without a label, the larger the uncertainty in the fitting, which results in an overestimation of the number of monomers per oligomer. Clearly, for a two species system, overestimating the aggregation number of the smaller species will also influence the aggregation number found for the larger species.

On the other hand, using a too high label density will result in similar problems as for conventional photobleaching. The intensity decay will converge to an exponentially decaying curve, making it impossible to accurately determine the number of bleaching steps. As a consequence, those oligomers containing too many labels will not be included in the histogram, resulting in an underestimation of the number of monomers per oligomer.

4.2.5 Dopamine-induced oligomers with different label densities

To obtain optimal results it is thus necessary to choose the label density in such a way that both species do not suffer from either of these biases. To verify that the 20% label density we used is within the optimal range of label densities and hence gives accurate results for the aggregation number of both species, we also determined the photobleaching histograms for dopamine-induced αS oligomers with label densities of 15% and 10%, each built from bleaching traces of at least 100 distinct oligomers (see figure 4.8). There is, as expected, a clear shift of the histograms to a lower number of bleaching steps with decreasing label density, since a lower label density results in a lower average number of labels per oligomer. Each label density was fitted with a combination of two binomial distributions and the mean number of monomers per oligomer was determined for both species (figure 4.8, solid lines).

In chapter 5, we used simulations to determine the accuracy with which we can determine the aggregation number of this combination of oligomeric species when using the combination of single-molecule photobleaching and sub-stoichiometric labeling. We show in chapter 5 that for the combination of a 20-mer and 30-mer, when working within the optimal range of label densities, it is possible to determine the aggregation number with an accuracy of ± 5 monomers per oligomer for the 20-mer and ± 4 monomers per oligomer for the 30-mer, including possible errors made due to small mistakes in determining the labeling efficiency. If the uncertainty in the mean number of monomers per oligomer determined from the fitted binomial distributions is larger than the uncertainty we determined in chapter 5, we take the uncertainty determined by the fit.

The mean number of monomers per oligomer is determined as 17 ± 5 and 31 ± 6 for the 20% label density, 18 ± 5 and 36 ± 4 for the 15% label density, and 23 ± 5 and 44 ± 14 for the 10% label density, see table 2. The numbers of monomers that form an oligomer are, within the error bars, identical for the 20% and 15% label densities. To test whether the aggregation protocol reproducibly yields the same oligomers, we prepared a second batch of oligomers with an optimal label density of 15%. Well within the error bars, we found identical aggregation numbers (17 ± 5 and 35 ± 4) for this preparation, see figure 4.9 and table 4.3.

We cannot, however, resolve a small heterogeneity of the number of monomers per oligomer within each species. Such a range of species would result in a broadening of the histogram of bleaching steps compared to the fit, which is very difficult to observe if a sum of binomials is fitted. Furthermore, adding more species to the fit did not improve the fit or yield distinctly different values, indicating that possible additional species must have aggregation numbers similar to the species already found. Therefore, the largest heterogeneity within each species is given by the uncertainty in the mean number of monomers per oligomer.

For the 10% label density we observe deviations that can be explained by the low label density. For this label density, the mean number of bleaching steps for the smaller species of the dopamine-induced oligomers is less than two. In this case, more than 15% of the oligomers do not contain a fluorescent label due to the stochastic nature of the aggregation process and are hence not included in the histogram of

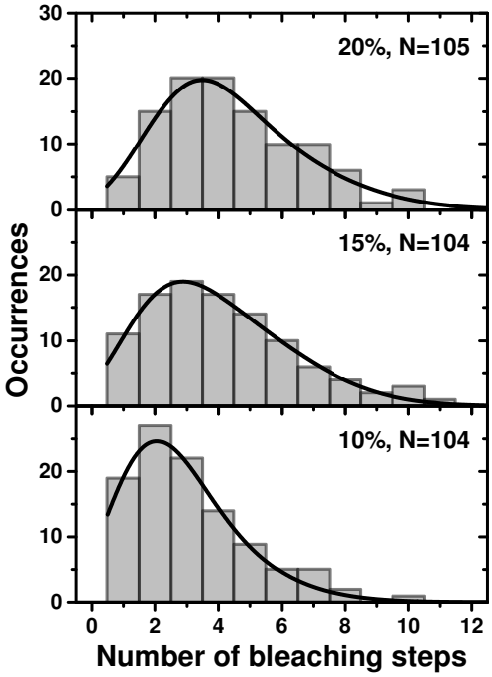

Figure 4.8: Histogram of bleaching steps for dopamine-induced oligomers with a 20%, 15%, and 10% label density, each built from bleaching traces of at least 100 distinct oligomers. The histograms are fitted with a combination of two binomial distributions (solid black lines). The mean values of the two binomial distributions give the mean number of monomers per oligomer for both species. The mean number of monomers per oligomer is determined as 17 ± 5 and 31 ± 6 for the 20% label density, 18 ± 5 and 36 ± 4 for the 15% label density, and 23 ± 5 and 44 ± 14 for the 10% label density.

bleaching steps. This will result in the observed overestimation of the aggregation number. This severe overestimation of the aggregation number of the smaller species also results in an overestimation of the number of monomers in the larger species. The uncertainty in the number of monomers per oligomer for the 10% label density is also reflected by the correspondingly large experimental error compared to that found for the 15% label density.

For the 20% label density we find a small deviation in the larger, second species compared to the 15% label density which can be attributed to the large number

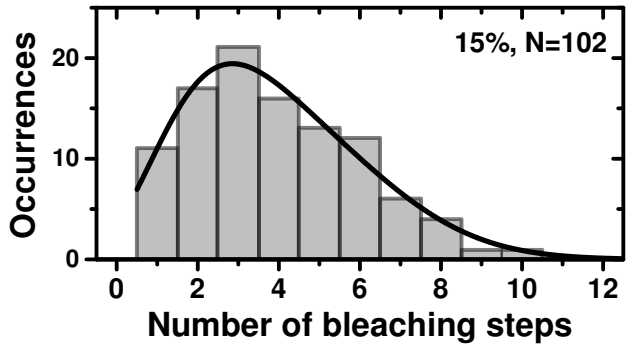

Figure 4.9: Histogram of bleaching steps for a second batch of dopamine-induced oligomers with a 15% label density, built from bleaching traces of 102 distinct oligomers. The histogram is fitted with a combination of two binomial distributions (solid black line). The mean values of the two binomial distributions give the mean number of monomers per oligomer for both species. We found identical aggregation numbers as compared to the first batch, namely 17 $\pm$ 5 and 35 $\pm$ 4 monomers per oligomer.

of bleaching steps. The mean number of bleaching steps for the larger species of the dopamine-induced oligomers is more than seven, which results in about 10% of the oligomers containing more than 10 fluorescent labels. As we showed in the previous chapter, 10 bleaching steps is at the limit of what can still be accurately determined from a time trace. This limit results in the observed underestimation of the aggregation number for the larger species, which is also reflected by the larger experimental error compared to the error found for the 15% label density.

The presence of oligomers with no labels, and oligomers with too many labels, limits the range of label densities within which the technique of single-molecule photobleaching in combination with sub-stoichiometric labeling can be used. The optimal label density depends on the aggregation number and the heterogeneity of the protein aggregates. As explained above, if the mean number of labels is less than two, more than 15% of the oligomers do not contain a fluorescent label. Therefore, as an estimate, the lowest suitable label density follows from the rule that the mean number of bleaching steps, and hence the mean number of labels, needs to be at least two. The mean number of bleaching steps is given by the product of the label density and the aggregation number. For the oligomers studied here, using the smallest

Table 4.3: Aggregation number found for each of the label densities including the accuracies determined in chapter 5.

Label density	Aggregation number
10%	23 ± 5 and 44 ± 14
15%	18 ± 5 and 36 ± 4
20%	17 ± 5 and 31 ± 6
Additional measurements	
15%, repeat	17 ± 5 and 35 ± 4
15%, no DA present	10 ± 2 and 30 ± 3

aggregation number found for the 15% label density of 18 monomers per oligomer as a reference value, the lowest suitable label density is about 11%.

On the other hand, if the mean number of labels is about eight, more than 15% of the oligomers will contain too many labels and will not be analyzable. Therefore, the highest suitable label density can be estimated following the rule that the mean number of bleaching steps should be about eight. For the oligomers studied here, taking the largest aggregation number found for the 15% label density of 36 monomers per oligomer, the highest suitable label density is about 22%.

4.2.6 Influence of dopamine: testing a third protocol

Our data clearly show that dopamine-induced oligomers are present in two species. This is fundamentally different from what we found in chapter 3 for oligomers formed under high protein concentrations during long incubation times: we found a single-well defined species.

To investigate whether this difference, single species versus double species, is the result of the presence of dopamine or is the result of the lower protein concentration

and the shorter incubation time, we also analyzed oligomers that are formed under the same conditions of low protein concentrations and short incubations times (just as the aggregation protocol for the dopamine-induced oligomers), but now in the absence of dopamine. We find that the oligomers formed in absence of dopamine also display a bimodal distribution but with clearly different aggregation numbers as compared to the dopamine-induced oligomers, namely 10 ± 2 and 30 ± 1, see figure 4.10 and table 4.3.

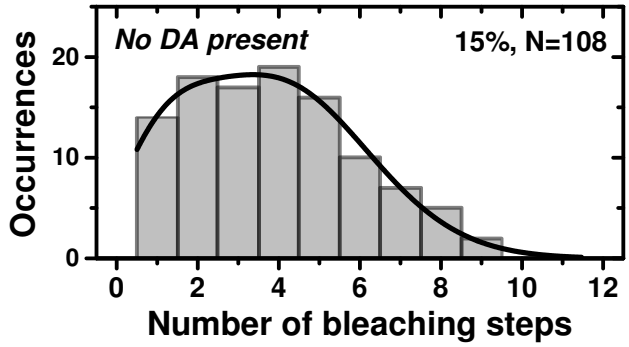

Figure 4.10: Histogram of bleaching steps for oligomers formed in the absence of dopamine with a 15% label density, built from bleaching traces of 108 distinct oligomers. The histogram is fitted with a combination of two binomial distributions (solid black line). The mean values of the two binomial distributions give the mean number of monomers per oligomer for both species. The mean number of monomers per oligomer is determined as 10 ± 2 and 30 ± 1.

Dopamine clearly has a specific effect on oligomer formation, leading to larger aggregation numbers for both detectable species. Dopamine has been reported to be incorporated in oligomers [62]. The observed difference in aggregation numbers in the presence of dopamine likely result from the changes in interactions between the αS monomers mediated by dopamine. There is considerable discussion about whether dopamine forms covalent or non-covalent bonds with αS [126, 127], although we are not in a position to distinguish between these possibilities with this technique. We note that the dopamine concentrations used are high compared to reported

physiological concentrations [128], although it is reasonable to assume that the dopamine concentration is elevated in the *Substantia Nigra*.

4.3 Conclusions and discussion

We have determined the aggregation number of dopamine-induced αS oligomers using the combination of single-molecule photobleaching and sub-stoichiometric labeling. Using this combination of techniques, we are even able to distinguish multiple distinct species present in the same sample and to determine their respective aggregation numbers from a single histogram of bleaching steps. We showed that dopamine-induced αS oligomers are present in two clearly different species. We find a small species consisting of 15-19 monomers per oligomer and a larger species of 34-38 monomers per oligomer. The small spread in the number of monomers determined per species might reflect small variations in the number of monomers per oligomer. However, the current data does not allow resolving the details of the aggregation number within the individual species. Interestingly, the values found suggest that the larger species might be a dimer of the smaller species. The relative fractions obtained from the fit indicate that both species are present in about the same fraction.

We do not see any indications of the presence of even larger assemblies such as tetramers of the smaller species, which should be detectable at the 10% label density. The absence of larger assemblies suggests that the dopamine-induced oligomers are off-pathway and do not form fibrils, although additional seeding experiments are necessary.

The combined result of this chapter and the previous chapter highlight that αS oligomers are indeed a heterogeneous family of aggregates in which the molecular details of the oligomers strongly depend on the conditions under which the oligomers form. The technique of single-molecule photobleaching of sub-stoichiometrically labeled αS oligomers allows for the sensitive detection of subtle changes in the molecular composition and aggregation number, and makes a systematic study of the influence of the aggregation conditions on the aggregation number of the oligomers formed possible.

Interestingly, in contrast to earlier reports [51, 56, 62, 98], our findings in both this chapter and the previous chapter show that αS forms oligomers of a defined number of monomers and not of a wide distribution in the number of monomers per oligomer, although this could also be the result of the purification process. Depending on the conditions, oligomers of different aggregation number are formed. These findings of species of distinct aggregation number imply that oligomers organize in a stable structure, but that the structure depends on the aggregation conditions. Linking the well-defined aggregation number and specific structure of the oligomers to their cytotoxicity may allow insights into the cause of the disease and provide specific targets for pharmaceutical intervention.

4.4 Materials and Methods

4.4.1 Instrumentation and measurement procedure

The photobleaching experiments were performed using a custom-built inverted confocal microscope as described in chapter 2. In short, as excitation source, we used a pulsed diode laser operating at 640 nm at a repetition rate of 20 MHz (LDH-D-C-640; Picoquant, Berlin, Germany). An epi-illumination configuration was used, i.e., the illumination and emission collection are through the same microscope objective (UPLSAPO 60XW, 60X, 1.2NA, Olympus). The remaining excitation light in the detection path was suppressed with a long-pass filter (Razoredge, 664 nm; Semrock, Rochester, NY) and a band pass filter (Brightline, 708/75 nm; Semrock, Rochester, NY). The emission was spatially filtered using a 30 μm pinhole and was subsequently focused onto a single photon avalanche diode (SPCM-APQR-16; PerkinElmer, Waltham, MA), connected to a photon counting module (PicoHarp300; Picoquant, Berlin, Germany). The initial scanning of the sample was done at a high scanning speed, 2 ms per pixel, and low excitation powers, $\sim$50 W/cm^2, to prevent dye bleaching. We then located individual oligomers in the initial area scan, localized them in the focus of the microscope objective, and subsequently collected fluorescence intensity time traces from distinct oligomers. To record the time trace we used higher excitation powers, $\sim$750 W/cm^2, to make sure that each dye molecule photobleached.

Typical time traces are shown in figure 4.11.

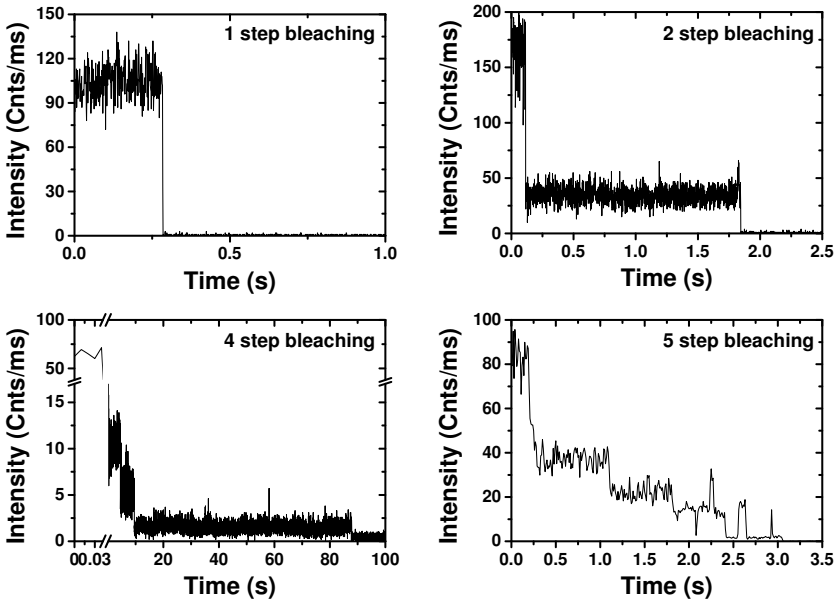

Figure 4.11: Four typical intensity time traces for fluorescently labeled αS oligomers. The time traces clearly shows discrete photobleaching steps. The graph shows one-step bleaching (top left), two-step bleaching (top right), four-step bleaching (bottom left), and five-step bleaching (bottom right). The time binning is optimized for each time trace to visualize the bleaching steps best. The intensity is background subtracted.

4.4.2 αS labeling, aggregation, and oligomer purification

Expression and purification of αS wild-type and mutant αS A140C was performed as previously published [125]. Prior to labeling, αS A140C in 10 mM Tris-HCl, 5 mM NaCl, pH7.4 was reduced with a six-fold molar excess of dithiothreitol (DTT) for 30 minutes at room temperature. The samples were desalted using a Pierce Zeba desalting column. A two-fold molar excess of Alexa Fluor 647 C2 maleimide

(Life Technologies, Invitrogen) was added and incubated for one hour in the dark at room temperature. Free label was removed using two consecutive desalting steps. The labeling efficiency was determined from the absorption spectrum. The protein concentration was determined from the absorbance at 276 nm using an extinction coefficient of 5745 M^{-1} cm^{-1}, the Alexa Fluor 647 concentration from the absorbance at 650 nm using an extinction coefficient of 239000 M^{-1} cm^{-1}. Subsequently, αS wild-type in 10 mM Tris-HCl, pH7.4 was added to the labeled αS A140C to obtain the desired ratio between wild-type and A140C αS.

To prepare the αS oligomers, we optimized a protocol previously described in literature to generate oligomers within an acceptable time frame at the required yields [58]. In short, the mixture of labeled and wild-type αS was dried in a vacuum evaporator and dissolved in 10 mM Phosphate buffer, pH7.4 at a final protein concentration of 140 μM. Dopamine was added at a final concentration of 200 μM and the solution was incubated for 3 hours at 37 °C. To protect the dopamine from light induced degradation, we kept the sample in the dark during the entire aggregation time. To remove very large aggregates, the solution was filtered using a 0.22 μm spin filter. The oligomers were purified by size-exclusion chromatography on a Superdex200 gel filtration column using 10 mM Tris-HCl, 50 mM NaCl, pH7.4 as eluent. The fractions containing the αS oligomers were identified by the absorbance at both 276 nm and 650 nm. A typical elution profile is shown in figure 4.12.

4.4.3 Sample preparation for single-molecule spectroscopy

Microscope glass coverslips were cleaned by placing them for at least one hour in an UV/ozone cleaner (UV/Ozone ProCleaner Plus; Bioforce, San Diego, CA). To study the oligomers, they need to be immobilized. To realize this, the isolated oligomers were diluted to about 1 nM in water and directly spincoated for 10 s at 6000 rpm on top of a cleaned coverslip. The samples contained the oligomers at low concentrations, so that the oligomers were well separated and did not overlap within the diffraction limit of the microscope.

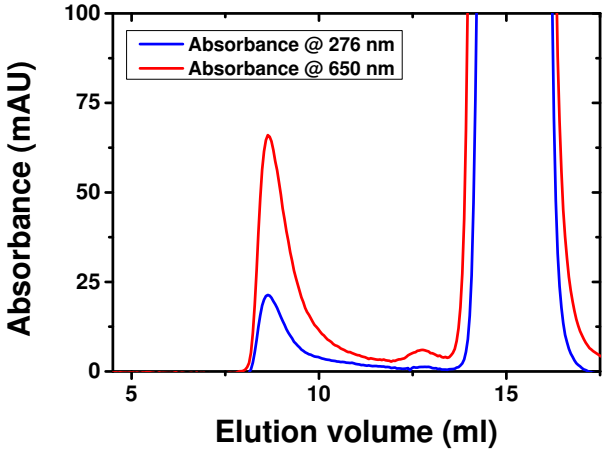

Figure 4.12: Typical elution profile of Alexa Fluor 647 labeled oligomers measured for the dye absorbance at 650 nm (red line) and the protein absorbance at 276 nm (blue line). The elution profile is for oligomers with a 10% label density. Indicated are the monomer and the oligomer peak. We have focused on the oligomers found in the peak eluting around ∼9 ml.

4.4.4 Fitting procedure

For the single species, the histograms of bleaching steps were fitted with a single binomial distribution given by

$$A \cdot \begin{pmatrix} n \\ k \end{pmatrix} \cdot p^k \cdot (1-p)^{n-k} \tag{4.2}$$

where A is the total number of analyzed oligomers, n is the aggregation number, k the number of fluorescent labels, and p is the label density.

For the Gaussian distributed aggregation numbers, a sum of binomials was used:

$$\sum_{N=n-W}^{n+W} A\left(n|n-W\right) \cdot \begin{pmatrix} N \\ k \end{pmatrix} \cdot p^k \cdot (1-p)^{N-k} \tag{4.3}$$

where N is the aggregation number, n is the center aggregation number, W is width of the Gaussian distribution, and $A\left(n|n-W\right)$ is Gaussian distributed area

and is given by:

$$A\left(n|n-W\right)=\frac{1}{\sigma\sqrt{2\pi}}\cdot\exp\left(-\frac{n^2}{2\sigma^2}\right) \tag{4.4}$$

where σ is the standard deviation, which was chosen in such a way that the Gaussian distribution had the desired width W. The sum of all amplitudes was normalized to the total number of analyzed oligomers.

The quality of the fits were determined using the reduced chi-squared parameter χ^2_{red}, which is given by:

$$\chi^2_{red}=\frac{\sum_{i=1}^{n}\left(y_i-y_{fit,i}\right)^2}{d_f} \tag{4.5}$$

where y_i is the experimental value, $y_{fit,i}$ is the fit value, n is the total number of data points, and d_f are the degrees of freedom, that is, the total number of data points minus the number of fit parameters.

All fitting was done using OriginPro 9.0 64-Bit.

Chapter 5

Single-molecule photobleaching on sub-stoichiometrically labeled aggregates: How well can we do?

5.1 Introduction

In the previous two chapters, we used single-molecule photobleaching on sub-stoichiometrically labeled α-Synuclein (αS) oligomers to determine their aggregation number. One of the main questions when using sub-stoichiometric labeling is how precise and accurate we can determine the aggregation number from a histogram of bleaching steps. In this chapter, precision refers to how reproducible the results are, or differently said, the uncertainty in the aggregation number found, while accuracy refers to how close the determined aggregation number is to the real aggregation number of the system.

5.1.1 Difficulties to precisely and accurately determine the aggregation number

Even though we do analyze a statistically relevant number of oligomers, typically ∼100, it is a limited subset, and therefore we do not measure a perfect distribution, but a distribution that includes some noise. It is possible that unintentionally more oligomers with a specific number of fluorescent labels are chosen to analyze, since a completely random selection is very difficult when using a limited number of distinct oligomers. Additionally, for some time traces it is difficult to determine the number of bleaching steps and sometimes a mistake will be made. Furthermore, since the incorporation of labeled monomers into the oligomer is stochastic, there will always be a fraction of the oligomers not containing a fluorescent label, which will then be invisible to the technique. On the other hand, we previously showed that it is possible to accurately determine up to 10 bleaching steps from a bleaching trace (see chapter 3). For oligomers consisting of more than 10 monomers, a fraction of the oligomers will contain more than 10 fluorescent labels. It is not possible to analyze the photobleaching traces arising from these oligomers and they will therefore not be taken into account into the final histogram of bleaching steps. These issues can influence the measured histogram, the quality of the fit, and hence the aggregation number found. It is therefore very important to tune the label density such that it is within the range of optimal label densities and that both the precision and accuracy with which the aggregation number can be determined are maximized.

Additionally, the interpretation of the histograms of bleaching steps assumes an accurate knowledge of the exact label density at the beginning of the aggregation. However, the real label density might deviate slightly from the label density aimed for, since it is very difficult to accurately determine the efficiency of labeling the monomeric protein. Although the errors made will be small when working within the range of label densities we used, it will influence the accuracy with which we can determine the aggregation number.

5.1.2 Additional difficulties arise for systems with more complex compositions

As we found in chapter 4 using single-molecule photobleaching on sub-stoichiometrically labeled dopamine-induced oligomers, there are systems that do not consist of a single, distinct species of oligomers, but are of a more complex composition. If the system consists of two species, it is very important to choose the label density in such a way that it is optimal for both species. Additionally, if there is no prior knowledge about the system, when is it still possible to distinguish a multiple species system from a single species system?

5.1.3 Aim of this chapter

In this chapter, we use simulated histograms of bleaching steps to gain insight into how precisely and accurately we can determine the aggregation number for a single species of oligomers and a combination of two species of oligomers. Additionally, we determine what the minimum detectable fraction of the second species must be in order to be able to distinguish between a single and two species system.

The purpose of this chapter is to evaluate the results found in the previous two chapters. Therefore, we limit ourselves to aggregation numbers similar to those found in those chapters. Additionally, we will establish practical guidelines on how to use single-molecule photobleaching to determine the aggregation numbers of sub-stoichiometrically labeled oligomers using the αS oligomers studied as examples. To show some general trends in the analysis accuracy and interpretation of systems of complex compositions, we will show some additional examples of different aggregation numbers or combinations of aggregation numbers. The methodologies developed in this chapter can be easily adapted for oligomers of different aggregation numbers or systems of different compositions.

Of course, the combination of single-molecule photobleaching and sub-stoichiometric labeling is not just suitable for amyloid oligomers, but can be used to study macro- or supramolecular assemblies in general.

5.2 Results and discussion

5.2.1 The basics: Simulated histograms and their interpretation

To simulate histograms of bleaching steps that closely resemble real, measured histograms, we first calculated an ideal histogram of bleaching steps using a binomial distribution, see equation (5.1) in the Methods section. Subsequently, to make the histograms more closely resemble real, measured histograms, we took the range between one and 10 bleaching steps, since this is the range we can analyze as explained above, and added amplitude dependent white noise using Matlab R2013a. Finally, we normalized the histogram to a total of 100 analyzed oligomers (N=100), since this is similar to the typical number of distinct oligomers we analyzed in the previous chapters. To determine the aggregation number, the final histogram including noise was fitted using a binomial distribution.

A typical simulated histogram of bleaching steps including amplitude dependent noise and corresponding binomial fit is shown in figure 5.1. The histogram was calculated for an aggregation number (AN) of 30 monomers per oligomer with a label density (LD) of 25%. The aggregation number of 30 was chosen to closely match the aggregation number we found for the αS oligomers we studied in chapter 3.

For the histogram shown in figure 5.1, the aggregation number was determined as 29.6 $\pm$ 0.6 monomers per oligomer. The precision is given by the uncertainty in the peak value determined by the fit. However, this is the uncertainty found for this specific, single histogram, that is, for this set of 100 analyzed oligomers. If we would repeat a real experiment, the histogram of bleaching steps obtained will look slightly different from the one we obtained during the first experiment. This is due to the above mentioned inherent noise due to the statistically relevant, but nevertheless limited number of aggregates we analyze and the way we select aggregates to analyze. It is very unlikely that the exact same set of 100 oligomers is selected a second or third time. Variations in histograms will result in variations in the aggregation number found.

To gain more insight into this variation, and hence the precision and accuracy, in

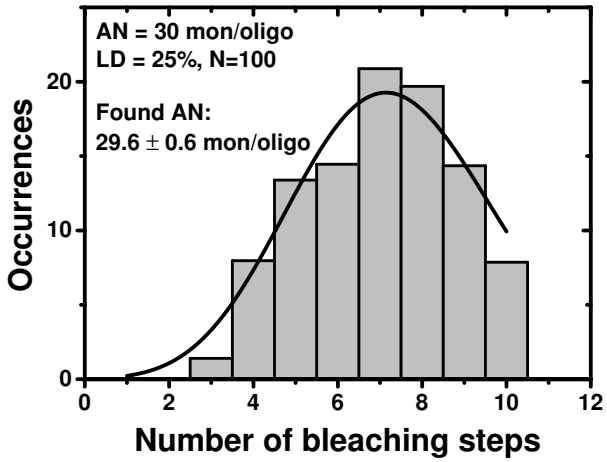

Figure 5.1: Typical simulated histogram of bleaching steps including amplitude dependent white noise. The input aggregation number is 30 monomers per oligomer with a label density of 25%. The total occurrences are normalized to 100 analyzed oligomers. Using a binomial fit (solid black line), the aggregation number was determined as 29.6 ± 0.6 monomers per oligomer.

the aggregation number determined from different histograms of bleaching steps, we calculated 100 of these histograms. All histograms were calculated for 30 monomers per oligomer and a 25% label density, but each histogram has different amplitude dependent white noise and therefore a different shape. Each of these histograms was fitted with a binomial distribution from which we determined the aggregation number. Finally, a histogram was built from all these aggregation numbers.

Figure 5.2 shows a typical histogram of aggregation numbers obtained as outlined above. The peak of the histogram gives the average aggregation number which was determined as 29.9 monomers per oligomer, indicating a high accuracy since it is the same as the input aggregation number of 30, although the histogram shows that there is a probability of about 20% that the aggregation number found deviates by 2 monomers per oligomer from the average. However, the precision with which we can determine the aggregation number is given by the half width at half maximum (HWHM) of the fitted Gaussian distribution, see black solid line in figure 5.2. Therefore, the uncertainty in the aggregation number for this specific species and

label density is determined as ±1 monomer per oligomer.

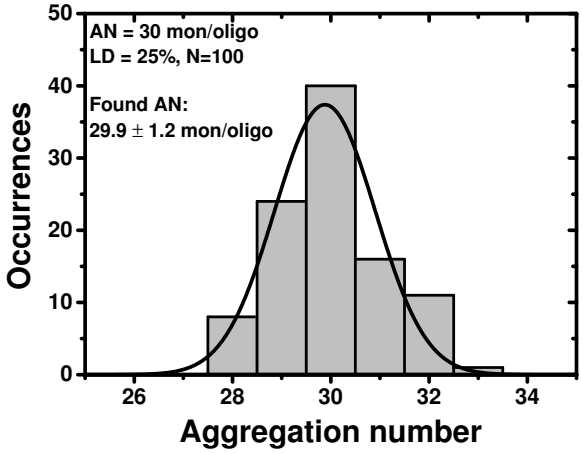

Figure 5.2: Histogram built from the determined aggregation numbers (AN) for all 100 simulated data sets. The black line is a Gaussian fit to the data. The aggregation number was determined as 29.9 ± 1.2 monomers per oligomer.

5.2.2 Optimal range of label densities for a single species

To study the influence of the label density on the precision, we repeated the simulations for a range of label densities, namely between 4% and 40%. As was mentioned above, when using sub-stoichiometric labeling, it is very important to work within the optimal range of label densities. To determine the optimal range, we not only determined the precision in the aggregation number, but also the quality of the binomial fit, that is, the reduced chi-squared parameter χ^2_{red}, see figure 5.3.

Figure 5.3 shows that both the precision in the aggregation number, as indicated by the error bars, and the χ^2_{red}, greatly depend on the label density used. For either a very low or very high label density, the uncertainty in the aggregation number increases. Moreover, the χ^2_{red} also increases, indicating that the quality of the fits is

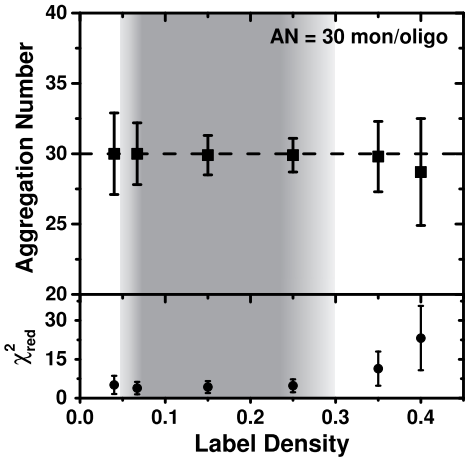

Figure 5.3: Determined aggregation number and quality of the binomial fits for a range of label densities for oligomers with an aggregation number of 30. The grey area indicates the optimal range of label densities. The translucent edges indicate that the technique might still work within this range, but it works best within the dark grey area.

reducing. This can be understood by considering the number of oligomers that cannot be analyzed. For low label densities, too many of the oligomers will not contain a fluorescent label and will therefore not be included in the histogram. The larger the fraction of oligomers without a label, the more difficult it is to accurately determine the aggregation number and hence the χ^2_{red} increases. On the other hand, using a too-high label density will result in problems similar to those encountered with conventional photobleaching. The intensity decay will converge to an exponentially decaying curve, making it impossible to accurately determine the number of bleaching steps. As a consequence, those oligomers containing too many labels will not be included in the histogram, resulting in an underestimation of the number of monomers per oligomer, as can be observed in figure 5.3, and therefore not only reducing the precision, but also the accuracy.

The optimal range of label densities is given by the combination of the precision of the aggregation number and the χ^2_{red} parameter. There should be an acceptable error on the aggregation number of about 2 and the χ^2_{red} should not significantly change within this range but rather stay constant. Therefore, the optimal range of label

densities is between ∼7% and ∼25%, giving a very broad range with almost threefold span in label density within which the technique works optimal. This range, however, is a minimal optimal range; the technique might still work just outside this range. Within this optimal range the uncertainty in the aggregation number is about ±2 monomers. However, even if a non-ideal label density is chosen, on average, we can still determine the correct aggregation number, only the uncertainty becomes larger.

Of course, the optimal range of label densities will depend on the aggregation number of the oligomer. Using the same label density, if the oligomer is larger, it will contain on average more fluorescent labels and will thus show more bleaching steps. On the other hand, if the oligomer is smaller, it will contain on average fewer fluorescent labels and will show fewer bleaching steps. To investigate the influence of the oligomer size on the optimal range, we calculated histograms of bleaching steps for oligomers with aggregation numbers of 10 and 50, see figure 5.4.

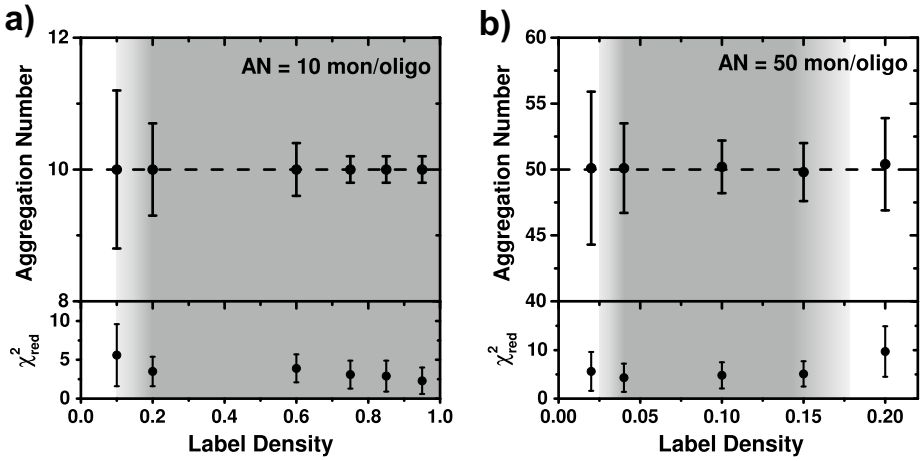

Figure 5.4: Determined aggregation number and quality of the binomial fits for a range of label densities for an input aggregation number of 10 (a) and 50 (b) monomers per oligomer. The grey areas indicate the optimal range of label densities.

Figure 5.4a shows that, for oligomers consisting of 10 monomers, the uncertainty

in the aggregation number changes only a little with decreasing label density. Even for a label density as low as 10% we can the uncertainty is only ±1. Interestingly, on average, for a 10-mer with a 10% label density, which means on average one bleaching step, we can still determine the aggregation number very accurately. Even a very narrow distribution is sufficient to determine the aggregation number for sub-stoichiometrically labeled oligomers. However, the quality of the fit does increase significantly when going to a 20% label density. Therefore, the combination of the uncertainty and the goodness of fit gives an optimal range between ∼20% and 100% for oligomers with an aggregation number of 10, indicated by the grey area in figure 5.4a. Within this range the uncertainty in the aggregation number is about ±1 monomers per oligomer.

If we now consider larger oligomers with an aggregation number of 50, see figure 5.4b, it can be seen that the absolute uncertainty in the aggregation number increases, although the relative uncertainty, that is, the uncertainty compared to the aggregation number, is smaller compared to the case of aggregation numbers of 10. For an aggregation number of 50, the optimal range of label densities is between ∼4% and ∼15%. Within this range the uncertainty in the aggregation number is about ±2 monomers.

In general, figure 5.4 shows that, as expected, the precision of the determined aggregation number depends on the actual aggregation number: the smaller the aggregation number, the higher the precision, and the larger the aggregation number, the lower the precision. Interestingly, the accuracy with which we can determine the aggregation number only starts to decrease when working well outside the optimal range of label densities.

5.2.3 Additional uncertainty: Labeling efficiency

A very important input parameter used in sub-stoichiometric labeling is the label density at the beginning of the aggregation. So far, it was assumed that the label density at the start of the aggregation is exactly known. However, determining the exact label density is not trivial. The desired label density is obtained by mixing unlabeled wild-type protein with labeled protein. For labeling, typically thiol reactive

probes are used. However, this labeling procedure does not result in 100% of the monomeric proteins labeled. Therefore, it is important to know the exact labeling efficiency.

The most common method to determine the labeling efficiency is to measure the absorbance spectrum of the labeled protein and determine the ratio between protein and fluorescent label via the extinction coefficient. The protein absorbance is typically around 280 nm and the main absorbance of the fluorescent label is typically between 400 nm and 700 nm. However, the fluorescent label also absorbs at 280 nm, typically between 1% and 5% of the peak absorbance. This small absorbance at 280 nm does influence the absorbance measured for the protein and hence the protein concentration determined. It is therefore important to determine the exact contribution of the fluorescent label on the protein absorbance by measuring the absorbance spectrum of the fluorescent label not bound to the protein and use this to correct for the protein absorbance and hence the protein concentration. The label densities used for the combination of sub-stoichiometric labeling and single-molecule photobleaching are typically small, less than 30%, and the errors made in the concentration of the labeled protein have therefore only a small influence on the final label density. For the range of label densities we work with, we estimate the total error made in the final label density as 5% of the label density that was aimed for.

To address the additional uncertainty introduced in the aggregation number by these errors, histograms of bleaching steps were simulated for an aggregation number of 30 monomers per aggregate with label densities of 19%, 20%, and 21%, that is, 20% ± (5% of 20%). All histograms were fitted assuming a label density of 20%, since that is the expected label density. Figure 5.5 shows the aggregation numbers found for the different label densities. As expected, the aggregation number increases when the actual label density increases compared to the expected label density. The additional uncertainty in the aggregation number we introduce due to errors made in the concentration determination is ±1 monomers per oligomer. As a practical generalization, one can assume that the error made in the final aggregation number is less than 5% of the actual aggregation number. So for a 100-mer, the added uncertainty will be less than ±5 monomers per oligomer.

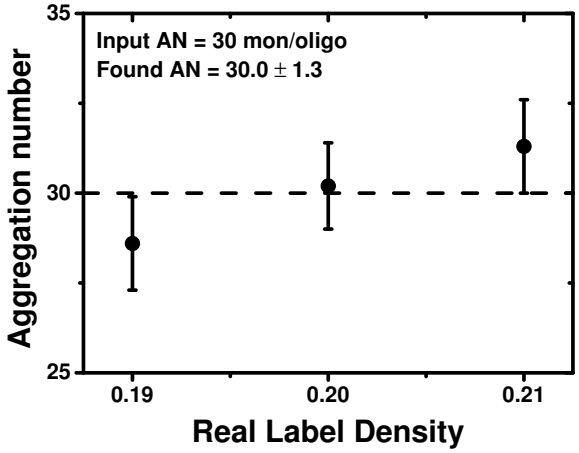

Figure 5.5: The aggregation number found for different label densities if a 20% label density is assumed at the start of the aggregation process. The estimated error made in the label density at the start of the aggregation is 5% of the label density aimed for.

5.2.4 Choosing and optimizing the label density

As expected, the optimal range of label densities does depend on the aggregation number and should therefore be optimized for every system. If there is no prior knowledge on the estimated aggregation number of the system under investigation, these data show that as an initial label density, 15% would be a good choice. For the range of aggregation numbers between 10 and 50, it allows for an precise determination of the aggregation number. Although this label density is outside the optimal range for an aggregation number of 10, it will still give the correct aggregation number, but with a larger uncertainty.

Depending on how the histogram of bleaching steps for this first run looks like, one might have to decrease or increase the label density for a second run. If the aggregates are too small for this label density, in the histogram there will be a large peak at 1 bleaching step. To obtain more reliable results, the label density should be increased. On the other hand, if the aggregates are too large for this label density, there will be many bleaching traces that cannot be analyzed due to the many bleaching steps, that is, the trace will look like an exponentially decaying curve. In this case, the

peak in the histogram will be at large number of bleaching steps (9 or 10). The label density should now be decreased for more reliable results. In general, multiple runs with different label densities are needed to obtain sufficient insight into the system to determine whether the optimal label density is used.

To summarize, we showed that single-molecule photobleaching on sub-stoichiometrically labeled oligomers is an excellent technique to determine the aggregation number of a single species of oligomers. The technique can be used for a wide range of aggregation numbers and works well within a broad range of label densities. The optimal range of label densities depends on the aggregation number of the oligomers under study, but can easily be optimized.

5.2.5 Two species instead of one

The discussion so far only holds for a system consisting of a single species of oligomers with a defined aggregation number. In chapter 4, however, we found that dopamine-induced αS oligomers are present in two distinct species. We found a small species consisting of $\sim$17 monomers per oligomer and a larger species consisting of $\sim$36 monomers per aggregate. The presence of the second species in the system makes it more difficult to determine the aggregation numbers from the histogram of bleaching steps precisely and accurately. For simplicity, let's consider two species that are present in equal fractions. The aggregation number of the first species is varied between 10 and 25 monomers per oligomer, while the aggregation number of the second species is kept constant at 30 monomers per oligomer. We used a label density of 25%, since this is the most suitable density for the combination of these two species. The overlap of the histograms of bleaching steps will become larger when the aggregation numbers become less well separated, see figure 5.6.

Figure 5.7 shows the aggregation numbers and corresponding uncertainties found for both species and the fraction of the first species. If the two species are clearly different in terms of aggregation number, that is, aggregation numbers of 10 and 30, the system can be considered to consist of two single species. As expected, figure 5.7 shows that we find the same uncertainty in the aggregation numbers as we found for the respective single species (see figures 5.3 and 5.4). Also, the relative fractions of

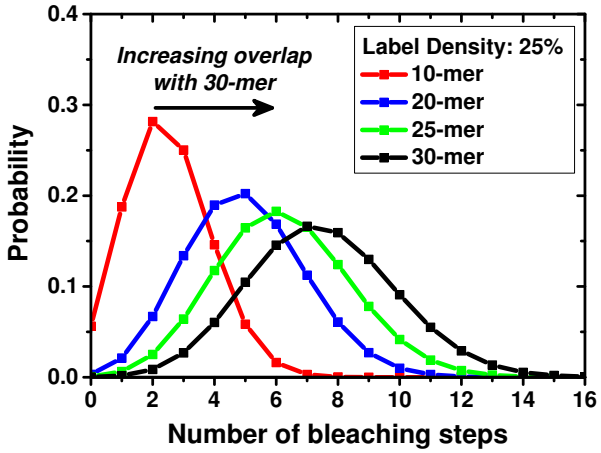

Figure 5.6: Simulated histograms of bleaching steps for 10-mer (red line), 20-mer (blue line), 25-mer (green line), and 30-mer (black line), all with a label density of 25%. The overlap with the histogram of the 30-mer becomes larger if the aggregation number of the smaller species increases.

both species can be determined accurately.

As expected, the closer the two species get in terms of aggregation number, the more difficult it becomes to accurately extract the information from the histogram. However, even for aggregation numbers as close as 20 and 30 monomers per aggregate, we can, on average, still determine the aggregation numbers reasonably precise, ± 5 monomers per aggregate, although the fraction that is found for the first species is incorrect, less than 10% instead of 50%. The fit cannot determine the contribution of the first species accurately anymore, since the histogram starts to resemble a single species. If we make the species even less well separated, 25 and 30 monomers per oligomer, it can be seen that both aggregation numbers start to deviate. Since the histogram looks like it only contains one single species, the fit finds one major species that has the average aggregation number of the two species, namely 27.5 monomers per oligomer, and a second species that is only used to compensate for deviations between the histogram and fit for the lower number of bleaching steps. Additionally, the fractions found for both species are incorrect. We will discuss whether it is possible to distinguish the presence of two species from a single species in detail below.

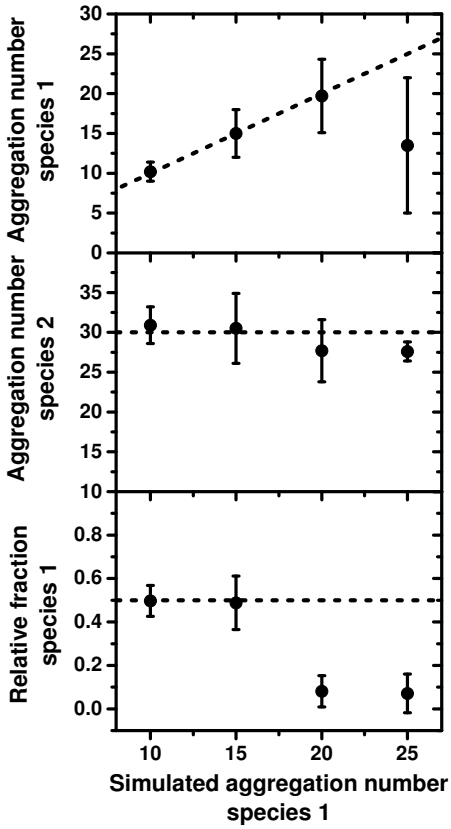

Figure 5.7: Aggregation numbers for a system consisting of two species present in equal fractions for varying aggregation number of the first species. The top panel shows the aggregation number found for the first species, the center panel shows the aggregation number of the second species, and the bottom panel shows the relative fraction of the first species.

The accuracy and precision with which we can determine the aggregation number of both species will depend on the fraction in which both species are present. Let's consider a system with two well separated species having aggregation numbers of 10 and 30 monomers per oligomer with a label density of 25%. Figure 5.8 shows the aggregation numbers found for both species for different fractions of the first species, the 10-mer.

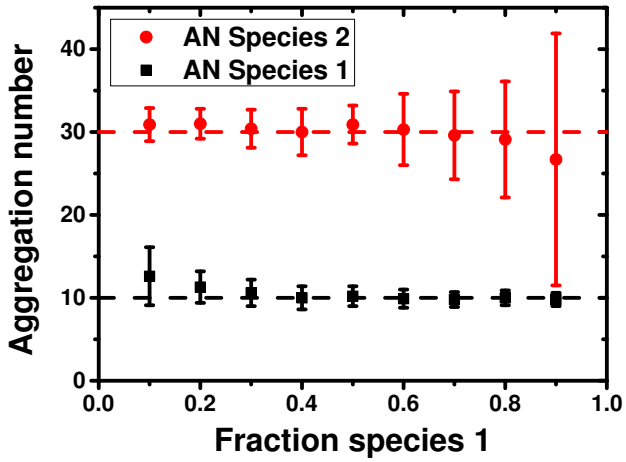

Figure 5.8: Aggregation numbers found for a system consisting of two species having 10 (black squares) and 30 (red circles) monomers per oligomer with a label density of 25% for different fractions of the 10-mer. The dashed lines indicate the aggregation numbers used in the simulations.

Figure 5.8 shows that the smaller the fraction of the species, the larger the uncertainty in the aggregation number. For very small fractions, less than 30%, even the average aggregation number starts to deviate, that is, the accuracy decreases. For a fraction of 90% of species one, the relative uncertainty in the aggregation number found for the 30-mer is very large, twice as large as for the 10-mer. The reason for this is that the histogram of bleaching steps for the 30-mer species is relatively broad compared to the histogram of the 10-mer, making it even more difficult for the fit to accurately find the peak position.

5.2.6 Single species or double species?

As can be seen from figure 5.7, if the aggregation numbers of the two species are too close to each other, it becomes increasingly difficult to determine the aggregation numbers with a high precision and accuracy, even for a system in which both species are present in equal fractions. To determine these aggregation numbers, we assumed that there are two species present in the system. But if there is no prior knowledge of

the system, the only way to determine whether there are one or two species present, is by determining the quality of the fit. If the system contains two species, the double species fit must be better than the single species fit. However, if the fraction of one of the species is getting smaller, it will become more difficult for the fit to find the aggregation number, as can be seen in figure 5.7. Below a certain fraction, it is not possible to distinguish between a single and double species system by looking at the quality of the fit anymore. Since a double species fit has more degrees of freedom, the quality might not increase anymore compared to a single species fit and it might even decrease.

To investigate the minimal fraction of a species needed to be able to distinguish between a single and double species, we determined the χ^2_{red} for the system consisting of two species with aggregation numbers of 10 and 30, for varying fractions of species, see figure 5.9.

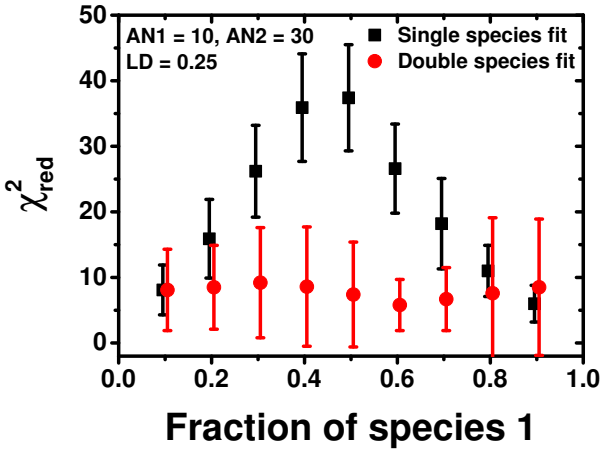

Figure 5.9: The χ^2_{red} parameter for a single and double species fit to the histograms of bleaching steps for a two species system, consisting of aggregates with aggregation numbers of 10 and 30, while varying the fraction of the first species.

Figure 5.9 shows that if the fraction of a species is between 30% and 70%, a two

species fit is clearly a better interpretation of the histogram of bleaching steps than a single species fit judged from the χ^2_{red}. If the fraction of one of the species however is getting less than 30% or more than 70%, the quality of the single species fit is similar or even better than the quality of the double species fit. Therefore, for this system with well separated aggregation numbers, a species needs to present in more than 20% to discriminate between a single and a double species system.

If the two species are less well separated, the fraction that is needed to make this discrimination increases, see figure 5.10. Since figure 5.9 shows the expected symmetry around a fraction of 50%, we only simulated the range between 10% and 50%.

In the case of a 15-mer and 30-mer, at least a 30% fraction of the first species is needed. Bringing the two species even closer to a 20-mer and 30-mer, even for a 50% fraction it is difficult to make the discrimination between a single and double species. In the case of a 25-mer and 30-mer, it is not possible to make the discrimination at all.

5.3 Conclusions and discussion

In the previous two chapters, we used single-molecule photobleaching on sub-stoichiometrically labeled αS oligomers to determine their aggregation numbers. The aim of this chapter was to evaluate the aggregation numbers found in these chapters. To do this, we used simulated histograms of bleaching steps to gain insight into the precision and accuracy with which we can determine the aggregation number of a single species of oligomers and a combination of two species of oligomers. We also studied what the minimum fraction of a second species should be to be able to distinguish between a single and two species system.

In chapter 3, we found αS oligomers with a well-defined aggregation number of 30 monomers per oligomer. In this chapter, we demonstrated that we did indeed work within the optimal range of label densities for these oligomers and that it is possible to determine their aggregation number with a precision of ± 3 monomers per oligomer, including possible errors made due to small mistakes in determining the

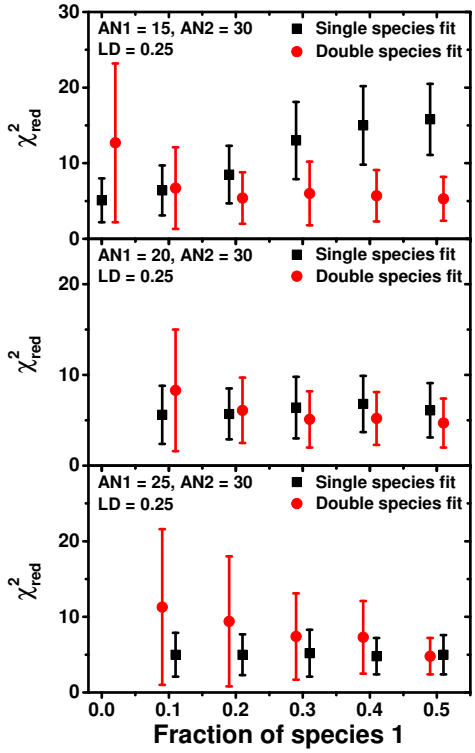

Figure 5.10: The χ^2_{red} parameter for a single and double species fit to the histograms of bleaching steps for decreasing separation of the two species

labeling efficiency.

In chapter 4 however, we found two coexisting, distinct species of dopamine-induced αS oligomers. One species consisted of 15-19 monomers per oligomer, while the second species consisted of 34-38 monomers per oligomer. We demonstrated that also for this combination of aggregation numbers, we worked within the optimal range of label densities and that it is possible to determine the aggregation number with a precision of ± 5 monomers per oligomer for the 20-mer and ± 4 monomers per oligomer for the 30-mer. Additionally, we demonstrated that, for this system, we can easily distinguish a double species system from a single species system by considering the reduced chi-squared parameter.

In general, we showed that single-molecule photobleaching on sub-stoichiometrically labeled oligomers is an eminently suitable technique to determine the aggregation number of a single species of oligomers consisting of a wide range of aggregation numbers and that the technique works well within a broad range of label densities. The optimal range of label densities does depend on the aggregation number of the oligomers under study.

For a system consisting of two species, we showed that both the accuracy with which the aggregation numbers can be determined and the minimum fraction of a species that is needed to distinguish between the presence of a single and double species depend significantly on how well the two species are separated in terms of aggregation number. The closer the aggregation numbers, the lower the accuracy and the more difficult it becomes to discriminate between a single and double species.

The combination of single-molecule photobleaching and sub-stoichiometric labeling can not only be used to study oligomers, but can also be applied to macro- or even supramolecular aggregates. In this chapter, we used a methodology that can easily be adapted to larger aggregates or systems of more complex compositions.

5.4 Methods

5.4.1 Simulation procedure

Aggregation and hence the incorporation of labeled subunits into the aggregate, is described by a classical Bernoulli experiment, where there is no preference to incorporate either a labeled or an unlabeled subunit. Therefore, the histogram of bleaching steps is calculated using a single binomial distribution given by:

$$P\left(k|A,L\right) = N \cdot \left(\begin{array}{c} A \\ k \end{array} \right) \cdot L^k \cdot (1-L)^{A-k} \tag{5.1}$$

where P is the probability that an oligomer of aggregation number A with label density L, contains k fluorescent labels. The distribution is normalized to the total number of analyzed aggregates N.

To simulate histograms of bleaching steps for a system of two species, we used a combination of two binomials distributions, given by:

$$P(k|A,L) = N \cdot \left(f_1 \cdot \begin{pmatrix} A_1 \\ k \end{pmatrix} \cdot L^k \cdot (1-L)^{A_1-k} + f_2 \cdot \begin{pmatrix} A_2 \\ k \end{pmatrix} \cdot L^k \cdot (1-L)^{A_2-k} \right) \quad (5.2)$$

where P is the probability that a combination of two species of aggregates with aggregation numbers A_1 and A_2 and label density L, present in relative fractions f_1 and f_2, contain k fluorescent labels. The distribution is normalized to the total number of analyzed aggregates N.

To make the histograms more closely resembling the real measured histograms, we took the range of bleaching steps between one and 10 and added amplitude dependent white noise using Matlab R2013a. Subsequently, we normalized the simulated histogram to contain 100 events, or distinct aggregates.

5.4.2 Fitting procedure

To obtain the aggregation number from the simulated histograms, the histograms were fitted in OriginPro 9 using either a single binomial distribution, see equation (5.1), or a combination of two binomial distributions, see equation (5.2). The optimal fit was determined by minimizing the reduced chi-squared parameter χ^2_{red}, which is given by:

$$\chi^2_{red} = \frac{\sum_{i=1}^{n} (y_i - y_{fit,i})^2}{d_f} \quad (5.3)$$

where y_i is the experimental value, $y_{fit,i}$ is the fit value, n is the total number of data points, and d_f are the degrees of freedom, that is, the total number of data points minus the number of fit parameters.

Chapter 6

Mapping the conformation of α-Synuclein monomers incorporated in an oligomer

6.1 Introduction

As was outlined in the first chapter, understanding the self-assembly process of α-Synuclein (αS) is essential in understanding the cause of Parkinson's disease. Important information about the self-assembly process is hidden in the very first steps of the aggregation process. αS in its monomeric form is considered to be an intrinsically disordered protein, which means that it does not have a stable secondary or tertiary structure at physiological conditions. Hence, the monomeric protein undergoes continuous conformational fluctuations, that is, it continuously changes its 3D structure. It is unclear whether there are a limited number of preferred conformations of the monomer that allow self-assembly into oligomers or whether there is no preferred conformation of the monomer.

As was discussed in chapter 1, to gain insight into the structural features of

αS monomers incorporated in oligomers formed under high protein concentrations and long incubation times, our group previously performed a systematic structural study using Tryptophan (Trp) spectroscopy [53]. These Trp measurements provided information about the microenvironment of the Trp residues and indicated a homogeneous and well-defined fold of the monomeric proteins incorporated into the oligomers. Additionally, as we showed in chapter 3, for these oligomers we found a single, well-defined aggregation number of about 30 monomers per oligomer. The results of these two studies combined suggest that the oligomers formed under these specific aggregation conditions organize in a stable structure and that hence it is reasonable to assume that the monomers incorporated into these oligomers might have a well-defined conformation.

Recently, structural studies were performed on oligomers formed under similar aggregation conditions using small angle x-ray scattering (SAXS) [54, 81]. These studies showed that the oligomers formed under these conditions have a monodisperse, globular structure and are present as two distinct species, where the major species consists of about 30 monomers per oligomer.

However, both the Tryptophan and the SAXS measurements only provide a low-resolution, ensemble averaged structure of the oligomers; no information is obtained about the actual conformation of the monomers incorporated into the oligomer, while this information is essential to gain insight into the early steps of aggregation. X-ray studies could provide a high-resolution structure, but for protein aggregates it is typically difficult to obtain a crystal with high diffraction quality needed for X-ray studies [129].

In this chapter, we use single-pair Förster resonance energy transfer (FRET) measurements to attempt to map the conformation of αS monomers incorporated into oligomers. FRET directly yields the distance between a donor and an acceptor fluorophore. By using a single FRET pair per oligomer, it is possible to access possible structural heterogeneity of monomers incorporated into different oligomers: It removes the ensemble averaging by looking at single pairs. By incorporating a range of double cysteine αS monomers containing a donor and acceptor fluorophore into oligomers and subsequently determining the distance between the two fluorophores on a single monomer within individual oligomers, indications for the structure of the

monomers incorporated into the oligomers can be obtained.

The oligomers under study are prepared using the same protocol used in chapter 3 and used for the Tryptophan measurements described above, which is based on high αS concentrations and long incubation times (for details on the aggregation protocol, see the Materials and Methods).

6.2 Single-pair Förster resonance energy transfer

Förster resonance energy transfer (FRET) offers a sensitive tool to determine distances at the nanometer scale and is often called the molecular ruler. FRET is the process in which energy is transferred from an excited donor fluorophore to a neighboring acceptor fluorophore, typically located within nanometer proximity of the donor. FRET is a non-radiative process that is based on the resonance between the emission transition dipole moment of the donor and the absorption transition dipole moment of the acceptor. The efficiency of the energy transfer process, the FRET efficiency, for a donor and acceptor separated by a distance r is given by [107]:

$$E_{FRET} = \frac{1}{1 + \left(\frac{r}{R_0}\right)^6} \tag{6.1}$$

where r is the distance between the donor and acceptor, and R_0 is the characteristic Förster distance at which 50% of the donor energy is transferred to the acceptor, while the other 50% of the donor energy is dissipated by the usual radiative and nonradiative processes.

The Förster distance mainly depends on three factors: the spectral overlap between the donor emission and acceptor absorbance, the quantum yield of the donor, and the relative transition dipole orientation of the donor and acceptor, also called the orientation factor. Due to the requirement of spectral overlap, only specific dye pairs are suitable for FRET. Depending on the donor-acceptor orientations, the orientation factor can range between 0 and 4, but is generally assumed to be 2/3 for a donor-acceptor pair that both have freely rotating dipole moments. To prevent any restrictions on the rotation of the dipole moments due to surface interactions,

FRET measurements are typically performed in solution. In some cases, however, the fluorophores can interact with the protein to which they are attached, thus restricting their motion and introducing an uncertainty in the orientation factor [101, 130].

For the most commonly used FRET pairs, the Förster distance is in the range of 3-7 nm [101]. The maximum distance that can accurately be measured using FRET depends on the FRET pair, but is typically about 10 nm.

6.2.1 Determining FRET efficiencies in single-pair measurements

The most widely used method to determine the FRET efficiency relies on determining the fluorescence intensities emitted by both the donor and acceptor simultaneously, also called the ratiometric approach [131]. If there is FRET, energy will be transferred from the donor to the acceptor, resulting in a decrease of the fluorescence intensity of the donor and an increase in the fluorescence intensity of the acceptor. The decrease and increase in fluorescence intensity depends on the amount of energy transferred, and hence the distance between donor and acceptor.

In the ideal case, when there is no cross talk between the donor and acceptor channel, both channels have equal detection efficiencies, and the donor and acceptor fluorophores have identical quantum efficiencies, the FRET efficiency is given by:

$$E_{FRET} = \frac{I_A}{I_D + I_A} \tag{6.2}$$

where I_A and I_D are the background subtracted fluorescence intensities of the acceptor and donor respectively. If a FRET pair diffuses through the excitation volume, it will emit a burst of photons. All the photons emitted in such a burst are summed to obtain I_A and I_D. Therefore, I_A and I_D are also called the burst integrated intensities.

However, in a real experiment, there is cross talk between the detection channels and there are differences in both the detection efficiencies and quantum efficiencies of the donor and acceptor fluorophores. Therefore, equation 6.2 only gives an apparent FRET efficiency, which is an indication for the distance between the donor and

acceptor fluorophore. In order to determine actual FRET efficiencies, and hence actual distances, the burst integrated intensities need to be compensated for cross talk between the donor and acceptor detection channels, differences in fluorophore quantum yield, and differences in detection efficiencies of donor and acceptor. Taking all these corrections into account, the FRET efficiency is now given by:

$$E_{FRET} = \frac{I_A - (I_D \cdot L_{DA})}{I_A \cdot (1 - L_{DA}) + I_D \cdot (\gamma - L_{DA})} \tag{6.3}$$

where L_{DA} is the fraction of donor photons leaking into the acceptor channel, L_{AD} is the fraction of acceptor photons leaking into the donor channel, mainly due to reflection of the dichroic mirror, and γ is the combined compensation for differences in detection efficiency and quantum yield between donor and acceptor. Once all these correction factors are applied, it is possible to convert the FRET efficiency into actual inter-dye distances using the Förster radius R_0.

6.2.1.1 Determining the correction factors

Two separate experiments were performed to determine the correction factors L_{DA}, L_{AD}, and γ. First, the cross talk between the donor and acceptor channels was determined by measuring the fluorescence intensities in both channels for a sample containing only the donor fluorophore, in our case Alexa Fluor 488, or only the acceptor fluorophore, that is, Alexa Fluor 568, in nM concentrations. By comparing the intensities in both channels for the separate samples, the factors L_{DA} and L_{AD} can be determined as follows:

$$L_{DA} = \frac{I_A}{I_D} \quad \text{for the donor only sample} \tag{6.4}$$

and

$$L_{AD} = \frac{I_D}{I_A} \quad \text{for the acceptor only sample} \tag{6.5}$$

Using similar excitation powers as for the single-pair FRET measurements, L_{DA} and L_{AD} were determined as 0.06 and 0.01, respectively.

To determine the correction factor γ, the custom-built single-molecule setup was compared with a detector-calibrated Fluoromax 4 (Horiba Yovin) spectrofluorometer using a solution containing the doubly labeled protein, similar to the method described in [132]. These measurements showed that the correction factor is 0.85. Additional information on the exact experimental conditions under which this correction factor was determined can be found in [133].

6.2.2 Practical considerations for sample preparation

For single-molecule spectroscopy, it is very important to make sure that only one fluorescently labeled particle is observed at the same time, in this case one monomer or one oligomer containing a single labeled monomer. As was already mentioned above, the single-pair FRET measurements are performed in solution. A simple way to verify that only one particle is observed is by doing fluorescence correlation spectroscopy (FCS) [134]. The diffusion of fluorescently labeled particles through the laser focus will result in fluctuations in the detected fluorescence emission signal. The amplitude of the autocorrelation of this signal is a direct measure for the number of particles that are simultaneously in the confocal volume: the higher the amplitude, the lower the number of particles. This information can be used to make sure that a maximum of one particle is observed at the same time, which corresponds to an autocorrelation amplitude of one. A typical autocorrelation curve obtained for doubly labeled αS monomers is shown in figure 6.1, showing an amplitude of about 3, which means that on average much less than one particle resides in the confocal volume.

For αS monomers, making sure that the autocorrelation amplitude is above one is sufficient, since one monomer contains one FRET pair. However, oligomers consist of about 30 monomers as was shown in chapter 3. In addition to making sure only one oligomer is observed, it is also important to make sure that single oligomer contains a maximum of one FRET labeled monomer, or else an average FRET efficiency and hence structure is observed. Simply using a ratio of 1:30 between labeled and unlabeled monomers is not sufficient, since aggregation is a stochastic process that results in a distribution in the number of labeled monomers per oligomer, as was explained in chapter 3. Therefore, at least a ratio of 1:100 should be chosen to make

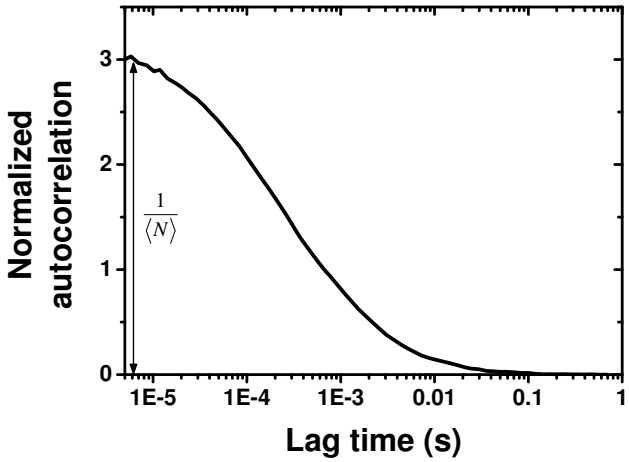

Figure 6.1: Typical autocorrelation curve obtained for double labeled αS monomers. The autocorrelation amplitude is much higher than 1, which means that on average much less than one particle resides in the confocal volume.

sure that less that 4% of the oligomers contain two or more FRET labeled monomers. For more details on the sample preparation, see the Materials and Methods section.

6.3 Doubly labeled αS monomers

To be able to construct a complete map of structure of the monomers incorporated into the oligomers, a series of double cysteine αS mutants was used, see figure 6.2. The labeling procedure used to produce doubly labeled monomers containing the donor dye Alexa Fluor 488 and acceptor dye Alexa Fluor 568, is described in [135]. There is no control over whether the cysteine residues are functionalized with a donor or an acceptor and hence three combinations of dyes on a single monomer are possible: one donor dye and one acceptor dye, two donor dyes, or two acceptor dyes. Figure 6.2 shows the six different double cysteine mutants used, including the positions where the cysteines were introduced and the number of amino acids between the two cysteine positions. The N-terminal part and central region of the protein (residues 1 to ∼100) are indicated by the rod, while the C-terminal part (residues ∼100-140) is indicated

by the curved line.

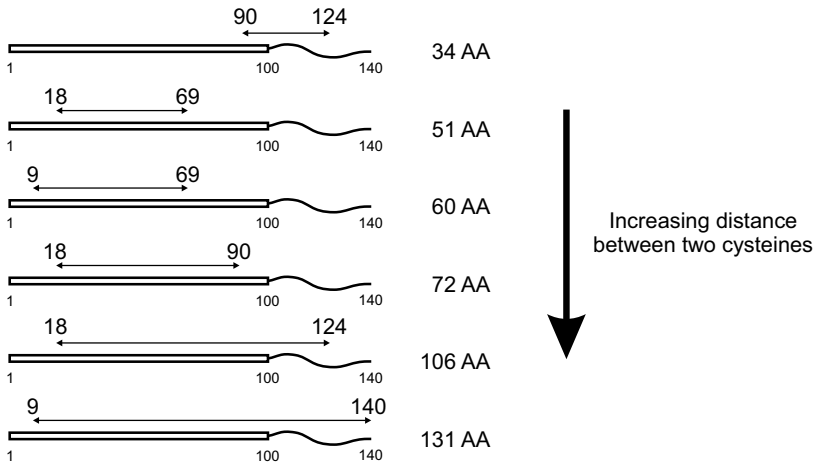

Figure 6.2: The six double cysteine αS mutants used for this study. For each mutant, the relative amino acid positions are indicated (1, 100, and 140) plus the positions where the cysteines were introduced (9, 18, 69, 90, 124, and 140). The N-terminal part and central region of the protein (residues 1 to ∼100) are indicated by the rod, while the C-terminal part (residues ∼100-140) is indicated by the curved line. On the right side, the number of amino acids (AA) between the two cysteines is indicated, with increasing number of amino acids from top to bottom.

Subsequently, the labeled monomers were incorporated into the oligomers in a 1:100 ratio with wild-type αS to ensure that each oligomer contains only a single doubly labeled monomer, as was described above. Six separate batches of oligomers were prepared, each batch containing one of the cysteine pair mutants. The oligomers under study are prepared using the same protocol used in chapter 3 and for the Tryptophan measurements described in chapter 1, which is based on high αS concentrations and long incubation times (for details on the aggregation protocol, see the Materials and Methods).

6.4 Mapping the structure of αS monomers incorporated into oligomers

The FRET measurements were performed on our custom-built single-molecule sensitive system, for more details see the Materials and Methods section and chapter 2. As explained above, the FRET efficiency can be determined by monitoring the photon bursts from freely diffusing αS oligomers. A typical time trace obtained for oligomers is shown in figure 6.3. The top and bottom panel in figure 6.3 show the emission intensity collected for the donor and acceptor respectively. The time trace clearly shows individual photon bursts, each corresponding to an individual oligomer diffusing through the confocal volume. The duration of these photon bursts is determined by the time it takes an oligomer to diffuse through the confocal volume. Bursts can show up in either the donor channel, the acceptor channel, or in both channels simultaneously, depending on the amount of FRET and whether the acceptor dye is fluorescently active. Figure 6.3, however, shows no fluorescence bursts in the acceptor channel, implying that there is little or no FRET between the donor and acceptor fluorophore.

By analyzing each burst individually in these time traces, a histogram of FRET efficiencies was built, see figure 6.4. To distinguish bursts from a single molecule from the background noise, a threshold level is set at about three times the background level. Additionally, the summed burst integrated intensity of donor and acceptor combined had to contain more than 40 counts. Only when the burst level was above the threshold level and the combined bursts contained more than 40 counts, was the burst included in the analysis. For more details on the analysis, see the Materials and Methods section.

Figure 6.4 shows the histograms of FRET efficiencies for all six doubly labeled αS monomers incorporated into oligomers, with increasing distance between the two cysteine positions from top to bottom. From three separate time traces of each 10 minutes, a total number of bursts (N), and hence individual oligomers, of more than 3000 was analyzed to build the individual histograms. Since the histograms show a single peak, the histograms were fitted with a single Gaussian distribution (solid blue line) from which the most frequent FRET efficiency was determined, see table 6.1.

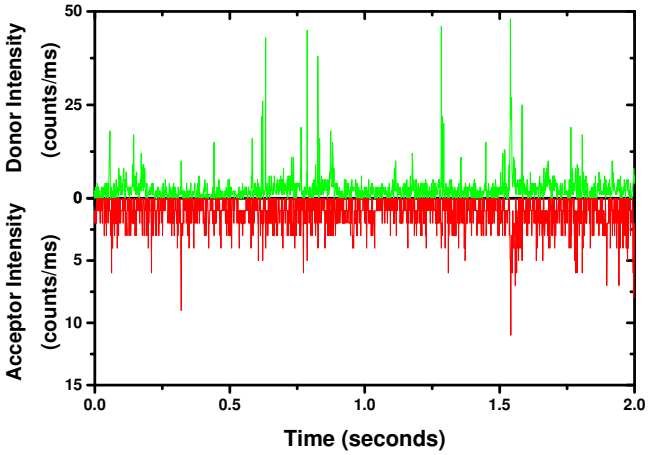

Figure 6.3: Typical time trace obtained for αS oligomers containing the 9/69 doubly labeled monomers freely diffusing in solution. If the oligomer diffuses through the excitation volume it emits a burst of photons. The top panel shows the emission intensity collected for the donor channel and the bottom panel for the acceptor channel. The time trace is binned to 1 ms.

Figure 6.4 shows six very similar histograms, all having a single peak centered at zero FRET efficiency.

In principle, the FRET efficiency cannot be smaller than 0 or larger than one. In practice, however, non-physical negative FRET efficiencies can show up in the histogram of FRET efficiencies. If the FRET efficiency is 0 or close to 0, the acceptor signal will be very small and the noise around the background level of the acceptor signal can result in a negative value for the burst integrated intensity for the acceptor signal. Since the FRET efficiency is calculated as the ratio between the donor and acceptor intensities (see equation 6.3), this can result in a negative FRET efficiencies. Similarly, non-physical FRET efficiencies above one can also be found if the FRET efficiency is one or close to one. Now, the donor signal will be very small and the noise around the background level of the donor signal can result in a negative value for the burst integrated intensity of the donor signal, resulting in FRET efficiencies of larger than one.

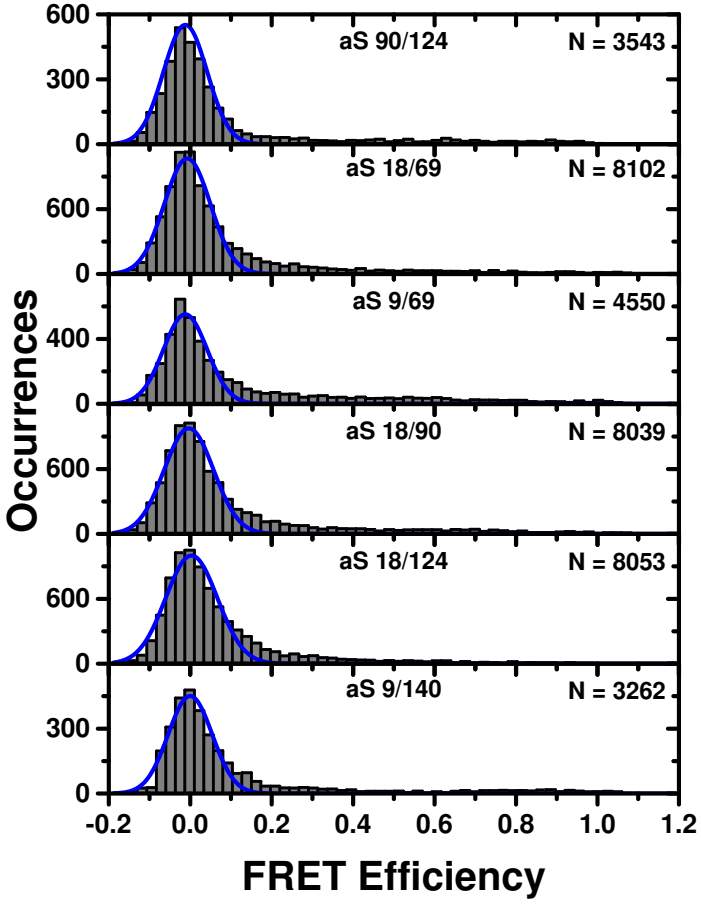

Figure 6.4: FRET-efficiency histograms of the αS oligomers freely diffusing in solution and containing six different doubly labeled αS monomers with increasing distance between the two cysteine positions from top to bottom. Solid lines represent Gaussian fits. Only a single peak was found for each histogram having a most frequent FRET efficiency of about zero, see also table 6.1. N gives the total number of occurrences, that is, the number of bursts analyzed.

As we discussed in the introduction of this chapter, there are two fundamentally different possibilities for the conformation of the monomers incorporated into the oligomers, both resulting in different histograms of FRET efficiencies: the monomers

Table 6.1: FRET efficiencies for all six doubly labeled αS monomers incorporated into oligomers. Only a single FRET efficiency peak was found for all six mutants. The most frequent (MF) FRET efficiency and HWHM are determined from the Gaussian fits shown in figure 6.4.

Double cysteine mutant	**FRET efficiency (MF ± HWHM)**
90/124	-0.01 ± 0.06
18/69	-0.01 ± 0.07
9/69	-0.01 ± 0.06
18/90	0.00 ± 0.07
18/124	0.00 ± 0.07
9/140	0.00 ± 0.06

either have a limited number of preferred conformations or the monomers have no preferred conformation. A preferred conformation would result in a narrow peak in the FRET efficiency that is centered at different values depending on the labeling positions used. No preferred conformation, that is, a completely random conformation, would result in a very broad distribution in FRET efficiencies, since every conformation, and hence a large number of inter-dye distances, is present in the oligomers. However, a single peak at zero FRET efficiency was observed for all of the mutants used, which does not correspond with what was expected beforehand. So what could this zero FRET efficiency imply? There are a few possibilities that could result in zero FRET efficiency.

First, the donor and acceptor dyes could simply be very far apart, that is, more than about 10 nm for the FRET pair used in this study. The shortest distance between the two cysteine residues is 34 amino acids for the αS 90/124. In a fully stretched conformation, 34 amino acids result in a distance of about 13 nm, assuming that each amino acid contributes 0.38 nm [136], which is more than can be determined using

FRET. For the other five mutants, the number of amino acids is more than 35, so this could result in zero FRET efficiency, even if they are not in a fully stretched conformation. However, if the zero FRET efficiency is the result of large inter-dye distance, finding it for all six mutants does imply that there must be some sort of common structure for the monomers incorporated into the oligomers. If there would be no common structure at all, that is, all monomers have a completely random conformation, it would be very unlikely that all oligomers show a zero FRET efficiency; one would expect to measure at least some FRET for a subset of the oligomers, especially since we are observing individual oligomers and are therefore not observing an ensemble average. However, it is a surprising and unexpected finding that the monomers are incorporated into the oligomer in some sort of extended conformation.

Single-pair FRET measurements are, however, very complex and there are a number of things that can go wrong. Therefore, in the next sections we will verify the quality of the labeling procedure, exclude errors made during the measurement procedure and analysis, and verify that the oligomers do contain monomers that have both donors and active acceptors.

6.4.1 Determining the FRET efficiency using ensemble emission lifetimes

A second method to determine the FRET efficiency is by comparing the donor emission lifetime in presence and absence of the acceptor. If there is FRET, the donor emission lifetime in presence of the acceptor will decrease compared to the lifetime in absence of the acceptor. The change in lifetime depends on the amount of energy transferred: The more energy is transferred, the larger the decrease in lifetime. To verify our finding of zero FRET efficiency using single-pair FRET measurements shown in figure 6.4, we also determined the emission lifetime of the donor for an ensemble of oligomers containing singly labeled, donor-only monomers and for an ensemble of oligomers containing doubly labeled monomers, see figure 6.5. For this ensemble measurement, the emission lifetime found for both the singly labeled and doubly labeled oligomers was similar. No lifetime change implies that there is no FRET, similar to what was found in figure 6.4 using single-pair FRET measurements.

Additionally, these lifetime measurements show that there is no energy transfer to a non-fluorescent acceptor dye, since the acceptor dye could be rendered non-fluorescent due to, for example, quenching by the oligomer itself.

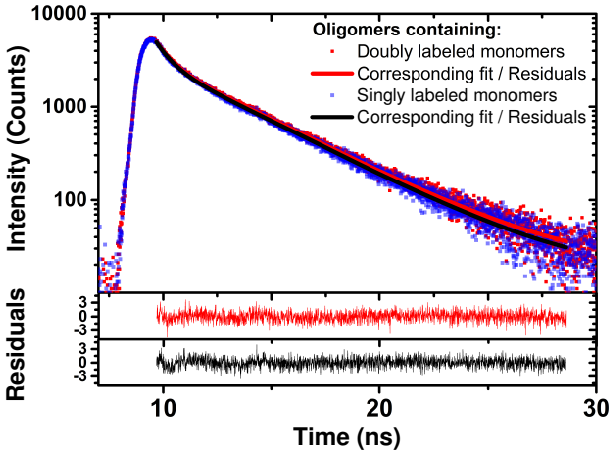

Figure 6.5: Typical decay curve for an ensemble of oligomers containing singly labeled, donor-only monomers and for an ensemble of oligomers containing doubly labeled monomers. The solid lines are single-exponential fits to the data from which the emission lifetimes were determined. The bottom two graphs show the residuals of the fits, where the color of the residuals matches the color of the corresponding fit. The emission lifetime found for both the singly labeled and doubly labeled oligomers was similar, implying there is no energy transfer.

6

6.5 FRET efficiency histograms of doubly labeled αS monomers

To verify the quality of the labeling procedure used to prepare the doubly labeled αS monomers, the histograms of FRET efficiencies for all six doubly labeled monomers are determined by monitoring the photon bursts from freely diffusing αS monomers.

A typical time trace obtained for monomers is shown in figure 6.6. The top and bottom panel in figure 6.6 show the emission intensity collected for the donor and acceptor respectively. The time trace clearly shows individual photon bursts, each corresponding to an individual monomer diffusing through the confocal volume. The acceptor channel in figure 6.6 clearly shows fluorescence bursts, implying that there is indeed energy transferred between the donor and the acceptor fluorophore; a significant difference with the time trace for oligomers shown in figure 6.3, where no acceptor bursts were visible.

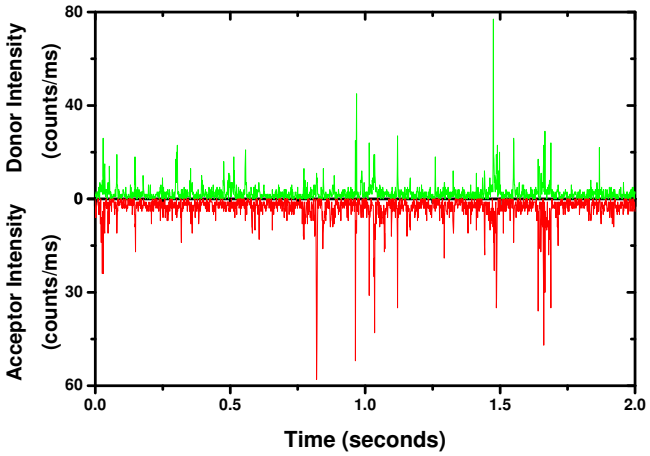

Figure 6.6: Typical time trace obtained for the 9/69 doubly labeled monomers freely diffusing in solution. If the monomer diffuses through the excitation volume it emits a burst of photons. The top panel shows the emission intensity collected for the donor channel and the bottom panel for the acceptor channel. The time trace is binned to 1 ms.

Figure 6.7 shows the histograms of FRET efficiencies for all six doubly labeled monomers. Since there are clearly two peaks in the histograms of FRET efficiencies, each histogram was fitted with a double Gaussian (solid blue lines). From each fit, the zero peaks and the most frequent FRET efficiencies for the doubly labeled monomers were determined, see table 6.2. The zero peaks, originating from monomers containing

either only donors or a donor with inactive acceptor, were consistently found at about zero FRET efficiency, similar to what was found for the oligomers. Using equation (6.1) and assuming a Förster distance of 6.2 nm for the dye pair used (according to manufacturer specifications), the FRET efficiencies can be used to determine the most frequent distances, see table 6.2.

Figure 6.7 shows a decrease in the FRET efficiency from the top panel to the bottom panel, see also table 6.2. This decrease is the result of the increase in the distance between the two cysteines from top to bottom (see also figure 6.2). As can be seen in equation (6.1), an increase in distance corresponds to a decrease in FRET efficiency. This is the exact behavior that can be seen in both figure 6.7 and table 6.2. The inter-dye distances found are in good agreement with previous reports in literature in which either single-pair FRET measurements or Monte Carlo simulations were used [137, 138]. They showed that the distances found correspond to αS exhibiting folding behavior somewhere between an excluded-volume random coil protein and a globular protein.

Additionally, table 6.2 shows that the width of the distributions also increases with increasing distance between the two cysteines. This can be understood by considering the intrinsically disordered nature of αS. Since αS is an intrinsically disordered protein, it can be expected to undergo significant conformation fluctuations, resulting in different structures for every distinct monomer observed. Therefore, there will be variation in the actual inter-dye distance, and hence FRET efficiency. The larger the distance between the two cysteine residues, the larger these fluctuations become.

For the 18/124 mutant however, a higher FRET efficiency was found compared to the general decreasing trend observed in figure 6.7. This sudden increase could be the result of the higher flexibility of the C-terminus of the monomeric protein, wherein residue 124 is located. A higher conformational flexibility is also reflected by the width of this distribution, which is relatively large compared to the four shorter distances. Previous reports using Monte Carlo simulations also observed sudden decreases in distances for specific residue combinations [138].

In general, the FRET efficiencies and inter-dye distances found for the six doubly labeled αS monomers are in good agreement with previous reports in literature using either single-pair FRET measurements or Monte Carlo simulations [137, 138]. Since

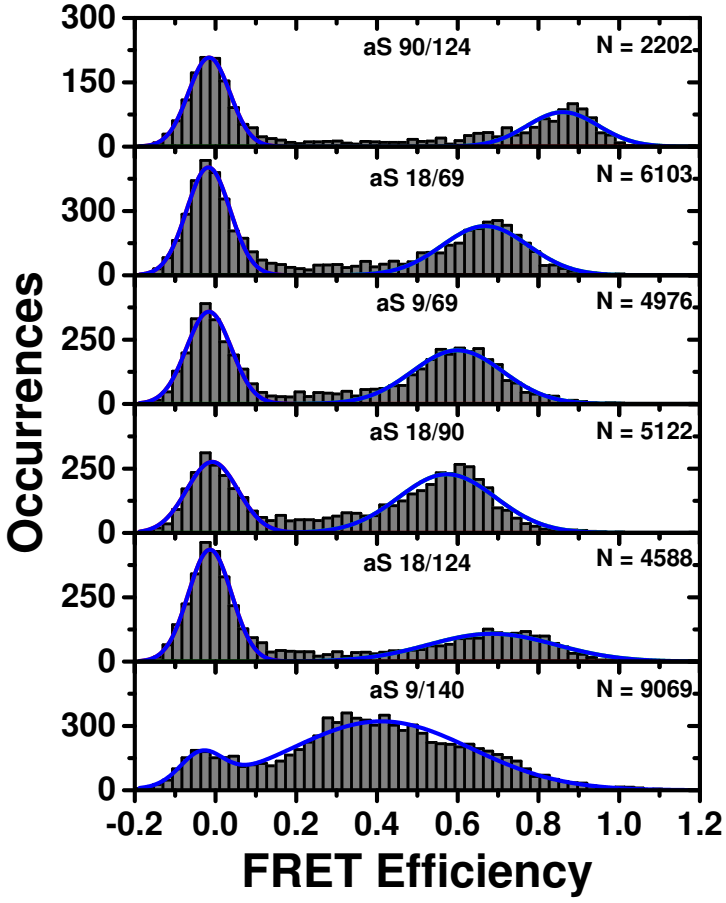

Figure 6.7: FRET-efficiency histograms of the six different doubly labeled αS mutants freely diffusing in solution with increasing distance between the two cysteine positions from top to bottom. Solid lines represent Gaussian fits to the data. FRET efficiencies determined from these fits are shown in table 6.2. N gives the total number of occurrences, that is, the number of bursts analyzed.

the double labeled monomers show the expected behavior in terms of FRET efficiency, it can therefore be concluded that the doubly labeled monomers are prepared properly and that the measurement procedure and analysis method is correct. However, to further verify the measurement procedure and analysis method, we also studied the

Table 6.2: Zero peak and FRET efficiencies for all six doubly labeled αS monomers. The distance is determined using equation (6.1) and assuming a Förster radius of 6.2 nm.

Double cysteine mutant	**Zero peak efficiency (MF ± HWHM)**	**FRET efficiency (MF ± HWHM)**	**Most frequent distance (nm)**
90/124	-0.02 ± 0.06	0.86 ± 0.10	4.6 ± 0.5
18/69	-0.02 ± 0.06	0.67 ± 0.13	5.5 ± 1.1
9/69	-0.02 ± 0.06	0.60 ± 0.13	5.8 ± 1.3
18/90	-0.01 ± 0.07	0.57 ± 0.14	5.9 ± 1.5
18/124	-0.01 ± 0.06	0.68 ± 0.18	5.5 ± 1.4
9/140	-0.03 ± 0.06	0.41 ± 0.26	6.6 ± 4.2

binding of αS monomers to SDS micelles in the next section.

6.6 Binding of monomeric αS to SDS micelles

To exclude errors made during the measurement procedure and analysis, we studied the binding of as monomers to SDS micelles. Our group previously studied the conformation of αS monomers upon interactions with SDS micelles using single-pair FRET measurements [135]. Veldhuis *et al.* used the same double cysteine 9/69 αS mutant containing the same FRET pair as we used here. It was shown that αS in the absence of SDS micelles remains in an unfolded state showing a low apparent FRET efficiency of about 0.54. However, upon binding to SDS micelles, the monomers undergo a conformational change forming a more tight conformation, the so-called horseshoe conformation, showing a higher apparent FRET efficiency of 0.82.

To further verify the measurement procedure and analysis method for our custom-built single-molecule sensitive system, we determined the histograms of FRET efficiencies for the same doubly labeled αS monomers in the absence and presence

of SDS micelles, see figure 6.8. The SDS concentration used was 12.5 mM, which is well above the critical micelle concentration for SDS in the buffer conditions used, namely 10 mM Tris at pH7.4.

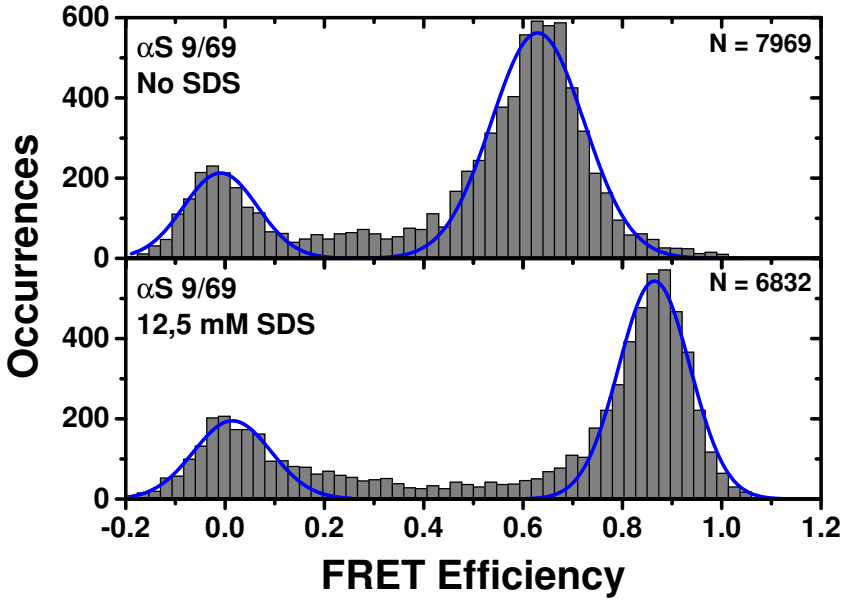

Figure 6.8: FRET-efficiency histograms of αS 9-69 in the absence (top) and presence (bottom) of SDS micelles. The solid lines are Gaussian fits to the data. There is a clear shift to higher FRET efficiencies upon addition of SDS, which is the result of the more compact horseshoe conformation that αS forms upon binding to micelles. N gives the total number of occurrences, that is, the number of bursts analyzed.

The top panel in figure 6.8 shows the histogram of FRET efficiencies in the absence of SDS. Since the histograms show two distinct peaks, the zero peak and the higher FRET efficiency peak, both histograms were fitted with two Gaussian distributions (solid blue line). The most frequent FRET efficiency for the higher FRET efficiency peak, which represents the population of interest, was determined from the Gaussian fit as 0.63, which is in very good agreement with what was observed before [135].

Small differences in determined FRET efficiencies compared to Veldhuis *et al.* are the result of different correction factors used. Since αS is an intrinsically disordered protein, it undergoes conformational fluctuations, resulting in the large full-width at half maximum (FWHM) of 0.22. Upon addition of SDS micelles, a clear change in FRET efficiency can be observed, see bottom panel in figure 6.8. The shift to the higher FRET efficiency of 0.86 is the result of a more compact conformation of the monomers bound to the micelles. Additionally, the distribution becomes more narrow with a FWHM of 0.17, which is attributed to a more uniform conformation of the αS monomers bound to the SDS micelles.

These measurements, in combination with the FRET measurements for the doubly labeled αS monomers shown in the previous section, show that we are capable of resolving differences in FRET efficiency for different conformations of αS monomers and that the FRET efficiencies we find are in good agreement with previous observations in literature.

Another possibility for zero FRET efficiency in the oligomers is the absence of a fluorescing acceptor dye, as we discussed in section 6.4. Since the emission lifetimes of the donor dye showed that there is no FRET to a non-fluorescing acceptor dye, the only possibility would be the complete absence of an acceptor dye.

6.7 Is the acceptor dye present in the oligomers?

To verify that the oligomers do contain monomers that have both donors and active acceptors, we determined the fluorescence emission spectra of an ensemble of oligomers using a commercial spectrophotometer: the Varian Cary Eclipse. Figure 6.9 shows the recorded emission spectra for oligomers containing the 9/69 mutant using either the donor excitation wavelength (485 nm) or the acceptor excitation wavelength (570 nm).

If the donor is excited at 485 nm, only a small amount of acceptor fluorescence is present, similar to what was observed for the single-molecule experiments. This would indicate that there is indeed a very low FRET efficiency. If the acceptor is directly excited at 570 nm, a significant amount of fluorescence from the acceptor is

visible, indicating that the acceptor is indeed present in the oligomers.

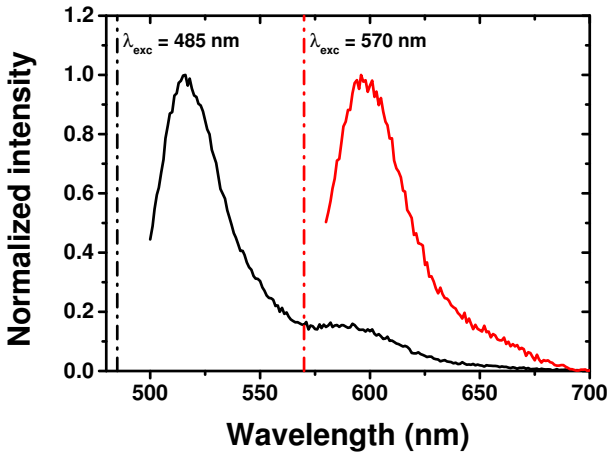

Figure 6.9: Fluorescence emission spectra for an ensemble of oligomers containing the αS 9/69 monomers. The black dash-dotted line indicates the donor excitation wavelength of 485 nm with the corresponding fluorescence emission spectra (solid black line). The red dash-dotted indicates the acceptor excitation wavelength of 570 nm with the corresponding fluorescence emission spectra (solid red line).

However, it could also be an indication of the presence of free acceptor dyes or free monomers in the sample, although the oligomers were purified using size exclusion chromatography and only the peak corresponding to the oligomer is under study. To verify that we are indeed looking at oligomers and not at free dye or free monomers, we performed FCS measurements on the oligomers containing the 9/69 doubly labeled monomers. Figure 6.10 shows three autocorrelation curves; one of 9/69 αS monomers (red circles) and two of oligomers with the 9/69 monomers incorporated using either the donor excitation wavelength (blue squares) or the acceptor excitation wavelength (green triangles). The measurements are on monomers/oligomers freely diffusing in solution. The autocorrelation curves are fitted with a single component free diffusion model in combination with a triplet state (black lines) [134]. The diffusion times and number of particles residing in the confocal volume as determined with the fits are

summarized in table 6.3.

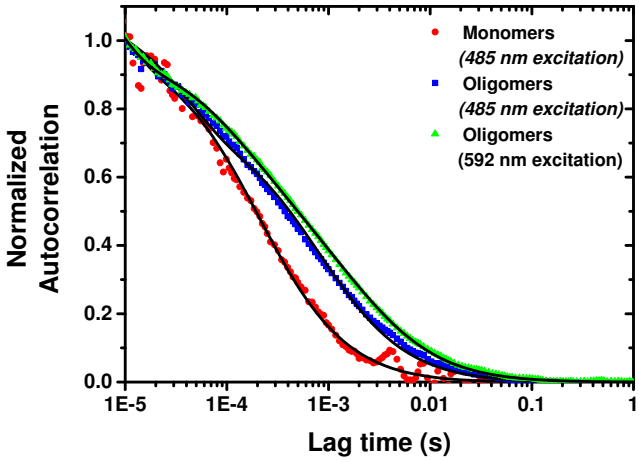

Figure 6.10: Normalized autocorrelation curves of freely diffusing αS monomers with donor excitation (red circles), oligomers with donor excitation (blue squares), and oligomers with acceptor excitation (green triangles) fitted with a single component free diffusion model in combination with a triplet state (solid black lines).

Figure 6.10 and table 6.3 show that there is the expected difference in the diffusion time found for the oligomers compared to the monomers, due to the difference in hydrodynamic radius. Previously performed unpublished results showed that there should be a factor of about 4 between the diffusion time of the monomers and the oligomers using the same excitation wavelength. Table 6.3 shows that there is indeed about a factor of 4 between the monomers and oligomers when directly exciting the donor at 485 nm. More importantly, the autocorrelation curve does not show indications of freely diffusing monomers or dyes. This shows that the donor dyes are indeed incorporated into the oligomers. For the same oligomers, exciting the acceptor directly at 592 nm shows a slightly longer diffusion time. However, since the excitation wavelength is longer, this will result in a larger confocal volume and hence a longer diffusion time. Additionally, the number of particles that reside in the confocal volume

simultaneously is very similar at both 485 nm and 592 nm excitation. As expected from the larger confocal volume for 592 nm excitation, the number of particles found using this wavelength is higher. The similar number of particles indicates that the donor and acceptor dyes are present in similar concentrations, as is expected when using doubly labeled monomers.

Table 6.3: Results from fitting the autocorrelation curves shown in figure 6.8 with a single component free diffusion model.

	Excitation wavelength (nm)	**Diffusion time (μs)**	**Number of particles**
Monomers	485	210	1.1
Oligomers	485	810	0.9
Oligomers	592	910	1.4

The combined findings from the fluorescence emission spectra and the FCS measurements show that the prepared oligomers do contain both donor and acceptor dyes. Furthermore, it shows that the acceptor dye is able to fluoresce and is not quenched due to, for example, interactions with the oligomer. These measurements do not contain information on whether the incorporated monomers contain both donor and acceptor simultaneously. However, the single-pair FRET measurements performed on the αS monomers in section 6.5 show that the monomers before aggregation contain both dyes and it is unlikely that one of the dyes is detached from the monomer during aggregation.

6.8 Conclusions and discussion

We have studied the conformation of αS monomers incorporated into oligomers formed under high protein concentrations during long incubation times using single-pair FRET measurements. FRET offers a sensitive tool to determine distances at the nanometer scale between a donor and an acceptor fluorophore. Using a series of six, double cysteine αS mutants labeled with a FRET pair a conformational map of the monomers incorporated into oligomers can be constructed. Since each oligomer contained a single doubly labeled monomer and the FRET efficiency for individual oligomers was determined, single-pair FRET should in principle allow accessing heterogeneity between different individual oligomers, information that cannot be accessed using ensemble based techniques such as SAXS or Tryptophan measurements.

For all six αS mutants incorporated into oligomers, we found a single peak centered at zero FRET efficiency, indicating that the donor and acceptor dyes are far apart, that is, more than 10 nm for the FRET pair used. Incorporation of monomers containing both donor dyes and active acceptors dyes was verified using fluorescence emission spectra and by performing FCS measurements. Both techniques showed that the oligomers indeed contain both dyes and that the acceptor dye is not rendered non-fluorescent. Additionally, the fluorescence emission spectra also showed a low FRET efficiency, similar to the single-pair FRET measurements. Furthermore, single-pair FRET measurements on the doubly labeled monomers and on monomers bound to SDS micelles showed similar results as previously reported in literature, from which it can be concluded that no errors were made in the sample preparation, measurement procedure, and analysis method.

Finding six very similar histograms all showing a peak around zero FRET efficiency does suggest that the monomers have a specific structure after being incorporated into the oligomers. If the monomers have a purely random structure, the FRET histograms should be very broad and should at least show some FRET efficiency for a subset of the oligomers. Therefore, the monomers must have a specific conformation, which is most likely an extended conformation. Furthermore, since the distribution of FRET efficiencies found are narrow and the histograms show no additional higher efficiency peaks, our findings indicate that the monomers probably have a limited number of

preferred conformations that allow for aggregation.

Unfortunately, the currently used FRET pair in combination with the chosen cysteine positions does not allow to probe the large distances found. Therefore, to gain more insight into the conformation of the monomers incorporated into the oligomers, it is necessary to use a different FRET pair that has a larger Förster distance and hence allows probing larger distances. Moreover, the two cysteines used for labeling should be introduced at different positions that are closer in the amino acid chain. Making the distances shorter and increasing the distances that can be determined using FRET, should allow creating a full conformational map of the monomers incorporated into the oligomers.

As we discussed in chapter 1, van Rooijen *et al.* studied the structural features of αS oligomers formed under identical conditions using Tryptophan measurements [53]. No spectral broadening of the emission spectra of Tryptophan was observed, indicating a homogeneous and well-defined conformation of the monomeric proteins incorporated into the oligomers, where the monomers have a solvent-shielded core consisting of about the first 100 residues of the amino acid sequence and a solvent-exposed C-terminus. These results in combination with our findings in chapter 3 that the oligomer have a well-defined aggregation number and the results of this chapter that the monomers have a specific, most likely extended conformation, provide strong evidence that the oligomers organize in a stable structure.

Our findings in chapters 3 and 4 that αS oligomers form species of distinct aggregation number, but that the aggregation number depends on the aggregation conditions used, implies that also the conformation of the monomers incorporated in oligomers formed under different aggregation conditions might differ. Identifying differences or commonalities in the structure of the monomers might provide valuable information about targets that help interfering with the progression of Parkinson's disease.

6.9 Materials and methods

6.9.1 αS preparation, labeling, and aggregation

Expression and purification of αS wild-type and the double-cysteine mutants shown in section 7.4 was performed as previously published [125]. The labeling of the double-cysteine mutants with the donor dye Alexa Fluor 488 and acceptor dye Alexa Fluor 568 was done as previously published [135]. The concentration of labeled protein was determined from the absorption spectrum by determining the absorbance of the Alexa Fluor 488 at 495 nm using an extinction coefficient of 72000 M^{-1} cm^{-1}.

To prepare the αS oligomers, we used the same protocol as described in chapter 3. In short, FRET labeled monomers were mixed with wild-type αS in a 1:100 ratio. The mixture was dried in a vacuum evaporator and dissolved using HPLC water at a final protein concentration of 1 mM in 40 mM Tris-HCl, pH7.4. The solution was incubated in an Eppendorf thermo mixer for 18 hours at room temperature with shaking at 1250 rpm and subsequently for 2 hours at 37 °C without shaking. The oligomers were purified by size-exclusion chromatography on a Superdex200 gel filtration column using 10 mM Tris-HCl, 50 mM NaCl, pH7.4 as eluent. The fractions containing the αS oligomers were identified by the 495 nm absorbance.

6.9.2 Samples for single-pair FRET measurements

Untreated 8-well chambered coverglasses with a #1.5 Borosilicate coverglass were used (Nunc Lab-Tek II, Thermo Scientific). The monomers or oligomers were diluted to sub-nM concentrations using a 10 mM Tris, pH7.4 buffer solution. For each measurement, at least 350 μL of solution was used to sufficiently fill the chamber with liquid and to be able to measure sufficiently far away from the bottom interface. Autocorrelations of the time traces were used to verify that the concentration was sufficiently low and that a maximum of one particle was in the confocal volume at the same time, see also section 6.2.2.

6.9.3 Instrumentation and measurement procedure

The singe-pair FRET experiments were performed using a custom-built inverted confocal microscope as described in chapter 2. In short, as excitation source, we used a pulsed diode laser operating at 485 nm at a repetition rate of 20 MHz (LDH-D-C-485, Picoquant). An epi-illumination configuration was used, i.e., the illumination and emission collection are through the same microscope objective (UPLSAPO 60XW, 60X, 1.2NA, Olympus). The remaining excitation light in the detection path was suppressed with a long pass filter (RazorEdge, 488 nm, Semrock) and an additional notch filter (Stopline, 488/14 nm, Semrock). The emission was spatially filtered using a 30 μm pinhole and was spectrally split into two detection paths for the donor and acceptor emission using a dichroic mirror (ZT561rdc, Chroma). The donor emission was filtered using a short-pass filter (Razoredge, 561 nm, Semrock) and the acceptor emission using a long-pass filter (BA590, 590 nm, Olympus). Subsequently, the donor and acceptor emission were focused onto two single photon avalanche diodes (SPCM-APQR-16, PerkinElmer), both connected to a photon counting module (PicoHarp300, Picoquant). The excitation power used to collect fluorescence intensity time traces was about 8 kW/cm^2. For all samples, three time traces of each 10 minutes were recorded. The histogram of FRET efficiencies was determined from the fluorescence intensity time traces using the Symphotime software (Symphotime 32bit, Picoquant). For analysis, the time traces were binned to 1 ms. To distinguish bursts from a single molecule from the background noise, a threshold level was set at about three times the background level. Additionally, the summed burst integrated intensities of both donor and acceptor combined had to contain more than 40 counts. Only when the burst level was above the threshold level and the combined bursts contained more than 40 counts, the burst was included in the analysis. The histograms were fitted with a double Gaussian using Origin Pro 9. The most frequent FRET efficiencies and corresponding widths of the distributions were determined from the Gaussian fits.

Chapter 7

Summary, conclusions, and future directions

7.1 Summary and conclusion

During the last 15 years, we have witnessed a major shift in the research focus to understand the cause of amyloid diseases. The attention has shifted from the fully matured amyloid fibrils to the nanometer sized aggregation intermediates called oligomers as the cytotoxic species that are at the basis of these diseases. Since then, there are an increasing number of reports in the literature discussing amyloid oligomers. In this thesis, we focused on α-Synuclein (αS) oligomers, potentially key players in Parkinsons disease.

Ever since the first realization that the αS oligomers are cytotoxic and might be responsible for Parkinson's disease, much effort has been devoted to: 1) fully characterize these oligomers in terms of structure, morphology, and aggregation number and 2) obtain detailed information on the formation process of these oligomers. This information is essential for understanding the disease process and to identify specific targets for pharmaceutical intervention. One would expect that all the research effort combined would quickly provide detailed biophysical insights into these

oligomers and provide a pharmaceutical strategy. Instead, it became abundantly clear that, depending on the preparation protocol used, these oligomers exhibit a significant degree of structural and morphological heterogeneity, making it extremely challenging to identify a specific cytotoxic type of oligomer and to fully characterize these.

Even information on the aggregation numbers of the different oligomers is lacking, simply because standard techniques struggle to provide reliable results, since they need suitable reference samples or need to determine the molecular weight of the oligomers first, which is very difficult for the typically unstable aggregates of intrinsically disordered proteins such as αS oligomers. Hence, a more direct approach is needed that avoids these problems. We therefore developed a new approach to determine the aggregation number of protein aggregates that combines single-molecule photobleaching and sub-stoichiometric labeling. By counting the number of discrete photobleaching steps in the intensity time traces for a large number of distinct oligomers and by applying a statistical analysis on the histogram of bleaching steps, the aggregation number can be determined.

This approach allows us to directly study the aggregation number of αS oligomers, and large macromolecular protein assemblies in general, without the need to determine the molecular mass of the oligomers first, the need to compare it with a reference sample, or the need for a high spatial resolution. This approach is therefore very suitable for the sensitive detection of subtle changes in the aggregation number and makes a systematic study of the influence of the aggregation conditions on the aggregation number of the oligomers formed possible. Additionally, it allows us to detect a possible distribution in the number of monomers per oligomer.

We used this approach to study the aggregation numbers of αS oligomers formed under several different aggregation conditions. For αS oligomers formed under high protein concentrations and during long incubation times, we find no distribution in the aggregation number and find a single, well-defined species consisting of about 31 monomers per oligomer. Additionally, we verified that for αS aggregation the fluorescent labels used do not have an influence. Combining these results with previous work by van Rooijen *et al.* in which a systematic Tryptophan study was performed to gain insight into the global structure of the oligomers [53], suggests that the oligomers formed under these specific aggregation conditions organize in a stable

structure that has a dense core comprised of the first 100 amino acid of the monomeric chain and a floppy, solvent exposed outer shell consisting of the C-terminus, see figure 7.1 for an artist impression of the possible global structure of these oligomers. The substantial helical structure shown in figure 7.1 is not necessary representative for the real structure.

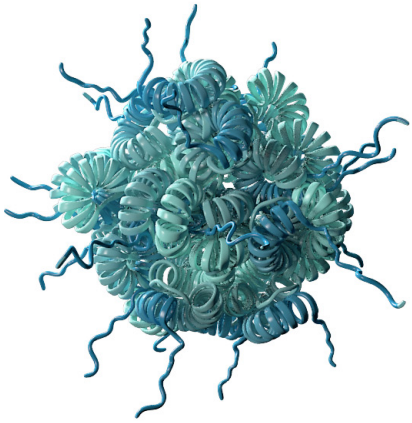

Figure 7.1: Artist impression of the possible global structure of αS oligomers derived from our single-molecule photobleaching approach and a systematic Tryptophan study. The substantial helical structure shown is not necessary representative for the real structure.

Using the same approach, we also studied the aggregation number for αS oligomers formed under different aggregation conditions, namely during short aggregation times and in the presence of the neurotransmitter dopamine. Using these sub-stoichiometrically labeled oligomers, we showed that we are able to distinguish multiple distinct species present in the same sample and determine their respective aggregation numbers from a single histogram of bleaching steps. We find a small species consisting of 15-19 monomers per oligomer and a larger species of 34-38 monomers per oligomer. If the same preparation protocol is used, only without the dopamine present, we again find two distinct species. However, the two species have

clearly different aggregation numbers as compared to the dopamine-induced oligomers. Now, we find a smaller species consisting of about 10 monomers per oligomer and a larger species of about 30 monomers per oligomer.

To gain insight into how accurate the aggregation numbers for a system consisting of a single species and for a complex system consisting of multiple species can be determined, we used simulated histograms of bleaching steps. In general, we showed that the technique works well within a wide range of aggregation numbers and thus within a broad range of label densities. The optimal range of label densities depends on the aggregation number of the system under study. For example, for an aggregation number of 30 monomers per oligomer, as we found in chapter 3, the optimal range of label densities is between ∼7% and ∼25%, giving a very broad range with almost a factor of 3 in label density. Within this range, the aggregation number can be determined with an accuracy of ±3 monomers. As expected, for a complex system consisting of more than one species, it is mainly the separation between the species in terms of aggregation number that determines the accuracy and the minimal detectable fraction. The closer the aggregation numbers, the lower the accuracy and the more difficult it becomes to discriminate between the different species. For example, in the case of a system consisting of a 20-mer and 30-mer, similar to what we found in chapter 4, the accuracy with which the aggregation numbers can be determined decreases compared to the simpler one species system and is ±5 monomers per oligomer for the 20-mer and ±4 monomers per oligomer for the 30-mer.

As was mentioned above, to identify specific pharmaceutical targets, it is not only important to identify and characterize the oligomers, but also study how they form. Important information on how the oligomers form is hidden in the very first steps of the aggregation process. Monomeric αS is considered to be an intrinsically disordered protein that undergoes continuous conformational fluctuations. It is still unclear whether there are a limited number of preferred conformations of the monomer that allow self-assembly into oligomers or that there is no preferred conformation of the monomer at all. We used single-pair Förster Resonance Energy Transfer (FRET) measurements to create a partial conformational map of αS monomers incorporated into oligomers.

We determined the histograms of FRET efficiencies for a series of six doubly

labeled αS mutants incorporated into oligomers For all six αS mutants incorporated into oligomers, we found a single peak centered at zero FRET efficiency, indicating that the donor and acceptor dyes are far apart. Finding six very similar histograms does imply that the monomers must have a specific structure after being incorporated into the oligomers. If the monomers would have a purely random structure, the FRET histograms should be very broad and should at least show some FRET efficiency for a subset of the oligomers. Therefore, the monomers must have a specific conformation, which is most likely an extended conformation. Furthermore, since the distribution of FRET efficiencies found are narrow and the histograms show no additional higher efficiency peaks, our findings indicate that the monomers do indeed have a limited number of preferred conformations that allow for aggregation.

7.2 How can we use this work in the future?

7.2.1 Single-molecule photobleaching and sub-stoichiometric labeling

In this thesis, we specifically developed a new approach combining single-molecule photobleaching and sub-stoichiometric labeling to determine the aggregation number of αS oligomers. However, as we showed in chapter 5, this approach can also be applied to many more systems having a large range of aggregation numbers, since the label density can be tuned to optimally match the aggregation number of the system under study. Having such an easily tunable parameter makes this approach very suitable to study a wide range of systems, ranging from nanoscale assemblies, such as protein aggregates consisting of 10s of subunits, to large macromolecular complexes, such as micelles formed through the self-assembly of polymers consisting of 100s to 1000s of subunits. Our newly developed approach opens exciting possibilities to accurately determine aggregation numbers especially for systems consisting of many subunits. Additionally, the methodology we presented in chapter 5 can easily be adapted to determine the accuracy in the aggregation number and estimate suitable initial label densities for these kinds of systems.

Furthermore, single-molecule photobleaching is not limited to complexes that have

sizes smaller than the diffraction limit of optical microscopy. This technique can also be used in a line scanning approach to obtain more insights in the aggregation number of, for example, protein fibrils or long polymer chains that have a sub-diffraction limited width but can be micrometers long. By photobleaching multiple spatially separated regions, an aggregation number per length unit can be derived. Combining this number with the total length of the fibril or polymer chain, the total number of monomers constituting the system can be determined.

7.2.1.1 Extending the approach: Multi-color single-molecule photobleaching

For very large systems consisting of more than ∼500 subunits, the optimal label density will become very low, that is, less than a few percent. For such low label densities, the error in the determined aggregation number will increase due to a relatively large uncertainty in the final label density. Multi-color single-molecule photobleaching could provide an increased accuracy in the aggregation number.

In multi-color photobleaching, multiple spectrally different dyes are used for labeling simultaneously, each at the same sub-stoichiometric ratio. The different fluorescent labels can be photobleached at the same time by illuminating the sample with multiple lasers operating at different wavelengths. By recording the photobleaching time traces for all the different dyes simultaneously using multiple detection channels, a histogram of bleaching steps can be constructed for each dye for exactly the same set of complexes. From each histogram, the aggregation number of the system can be obtained independently and should ideally give the same result, but most likely shows some diversity due to the extremely low label densities used. By combining the aggregation numbers found for each of the histograms, an average aggregation number and corresponding standard deviation can be determined, providing a higher accuracy compared to the aggregation number determined from a single histogram of bleaching steps.

Additionally, one could also imagine that a system has a complex molecular composition and is not purely built from a single component. Multi-color photobleaching can be used to study systems of complex composition by specifically labeling each

component with a different fluorescent label and determining the aggregation numbers of each component and their stoichiometry, even for large macromolecular assemblies.

7.2.2 αS oligomers: what should we do?

The realization that oligomers might be the cytotoxic species in many amyloid diseases as such makes them an interesting system to study. However, there is one major issue when studying αS oligomers: how do you prepare physiologically relevant αS oligomers *in vitro?*

There are a large number of different preparation protocols available in literature that all result in the formation of αS oligomers *in vitro*. However, it remains an open question what the biologically most relevant conditions are to prepare oligomers. The currently available protocols differ in terms of protein concentration, incubation times, agitation speeds, temperature, and buffer conditions. It even remains to be seen whether truly physiologically relevant conditions would actually be suitable for the laboratory, since Parkinson's disease is a late onset disease and waiting for decades in the laboratory to obtain a sufficient amount of αS oligomers to study does not seem to be a realistic option.

Taking all of this into account, one of the first key challenges in the research field is to form, detect, and characterize αS oligomers within the cell. There are a few reports in literature discussing the formation of αS clusters in cells, but detailed characterization of these clusters is lacking. One of the main challenges is to overcome the autofluorescence signal coming from the cells. One way to overcome this problem is using bright fluorophores. However, typically, organic fluorophores that can be expressed in the cell are not very bright or photostable. Inorganic fluorophores, on the other hand, are typically both bright and photostable, but need to be applied extracellularly and subsequently taken up by the cell. Inorganic fluorophores, however, might interfere with the function of the protein and disrupt the oligomer formation process.

Initial results from our laboratory show that SH-SY5Y neuroblastoma cells expressing GFP-tagged αS show αS clusters after differentiation. Preliminary results of single-molecule photobleaching on these *in vivo* formed clusters show that their

aggregation number is much larger and much more heterogeneous compared to the isolated oligomers discussed in this thesis and most of the literature. Although similar to the *in vitro* work, one of the challenges is to identify the physiologically most relevant type of cells to conduct these experiments on.

Additionally, even if we succeed in fully characterizing αS oligomers formed *in vivo* (and due to the major developments in the field of microscopy during the last decade, it might be possible soon), the main challenge still remains to identify the oligomers most relevant in the disease process. The more there is known about the αS oligomers, the less likely it seems that it is a specific type of oligomer that is responsible for cell death; there probably is a whole range of different oligomers that are cytotoxic. Without this information, it remains difficult to design an drug that interferes with the relevant oligomers.

7.2.2.1 What would be an alternative to oligomers?

Of course, there are many different ways to approach Parkinson's disease that could all result in a suitable pharmaceutical target. One alternative and probably very promising research direction in the near future is to target the first step in the disease process: the misfolding of the monomeric proteins. It is the misfolding of the monomeric proteins that allow them to interact and form cytotoxic oligomers. During the last decade, a number of chaperone molecules have been identified that interact with αS and decrease its cytotoxicity, including Hsp70, Hsp90, and Prefoldin.

However, the exact molecular mechanisms underlying the αS-chaperone interactions remain elusive. The formation of cytotoxic aggregates could possibly be prevented by selectively interfering with the folding process of the monomeric proteins without withholding them from doing their natural biological function, if there is any.

Single-molecule spectroscopy offers an ideal tool to study these interactions by selectively observing only the monomers or aggregates and chaperones that are interacting. It would be possible to distinguish between whether the chaperones, for example, prevent oligomer formation by assisting in the folding process, degrade oligomers, or even accelerate aggregation into mature fibrils and to directly study the mechanisms underlying these interactions.

References

[1] Reynaud, E., *Protein misfolding and degenerative diseases*, Nature Education **3** (9) (2010).

[2] Dobson, C. M., *Principles of protein folding, misfolding and aggregation*, Seminars in Cell & Developmental Biology **15** (1): pp. 3–16 (2004).

[3] Dobson, C. M., *Protein misfolding, evolution and disease*, Trends in Biochemical Sciences **24** (9): pp. 329–332 (1999).

[4] Hartl, F. U. and Hayer-Hartl, M., *Protein folding - molecular chaperones in the cytosol: from nascent chain to folded protein*, Science **295** (5561): pp. 1852–1858 (2002).

[5] Babu, M. M., van der Lee, R., de Groot, N. S., *et al.*, *Intrinsically disordered proteins: regulation and disease*, Current Opinion in Structural Biology **21** (3): pp. 432–440 (2011).

[6] Uversky, V. N., *Intrinsically disordered proteins from a to z*, The International Journal of Biochemistry & Cell Biology **43** (8): pp. 1090–1103 (2011).

[7] Dobson, C. M., *Protein folding and misfolding*, Nature **426** (6968): pp. 884–890 (2003).

[8] Anfinsen, C. B., *Principles that govern the folding of protein chains*, Science **181** (4096): pp. 223–230 (1973).

[9] Rose, G. D., Fleming, P. J., Banavar, J. R., *et al.*, *A backbone-based theory of protein folding*, Proceedings of the National Academy of Sciences, USA **103** (45): pp. 16623–16633 (2006).

[10] Ellis, R. J. and Hartl, F. U., *Principles of protein folding in the cellular environment*, Current Opinion in Structural Biology **9** (1): pp. 102–110 (1999).

[11] Hardesty, B. and Kramer, G., *Folding of a nascent peptide on the ribosome*, in: *Progress in Nucleic Acid Research and Molecular Biology*, volume Volume 66, pp. 41–66, Academic Press (2000).

[12] Braakman, I. and Bulleid, N. J., *Protein folding and modification in the mammalian endoplasmic reticulum*, Annual Review of Biochemistry **80** (1): pp. 71–99 (2011).

[13] Bukau, B., Weissman, J., and Horwich, A., *Molecular chaperones and protein quality control*, Cell **125** (3): pp. 443–451 (2006).

[14] Dobson, C. M. and Karplus, M., *The fundamentals of protein folding: bringing together theory and experiment*, Current Opinion in Structural Biology **9** (1): pp. 92–101 (1999).

[15] Ciechanover, A. and Brundin, P., *The ubiquitin proteasome system in neurodegenerative diseases: Sometimes the chicken, sometimes the egg*, Neuron **40** (2): pp. 427–446 (2003).

[16] Chiti, F. and Dobson, C. M., *Protein misfolding, functional amyloid, and human disease*, Annual Review of Biochemistry **75**: pp. 333–366 (2006).

[17] Schmit, J. D., Ghosh, K., and Dill, K., *What drives amyloid molecules to assemble into oligomers and fibrils?*, Biophysical Journal **100** (2): pp. 450–458 (2011).

[18] Wilson, M. R., Yerbury, J. J., and Poon, S., *Potential roles of abundant extracellular chaperones in the control of amyloid formation and toxicity*, Molecular BioSystems **4** (1): pp. 42–52 (2008).

[19] Petkova, A. T., Leapman, R. D., Guo, Z. H., *et al.*, *Self-propagating, molecular-level polymorphism in alzheimer's beta-amyloid fibrils*, Science **307** (5707): pp. 262–265 (2005).

[20] Luhrs, T., Ritter, C., Adrian, M., *et al.*, *3D structure of alzheimer's amyloid-b(1-42) fibrils*, Proceedings of the National Academy of Sciences, USA **102** (48): pp. 17342–17347 (2005).

[21] Kayed, R., Head, E., Thompson, J. L., *et al.*, *Common structure of soluble amyloid oligomers implies common mechanism of pathogenesis*, Science **300** (5618): pp. 486–489 (2003).

[22] Uversky, V. N., *Mysterious oligomerization of the amyloidogenic proteins.*, FEBS journal **277**: pp. 2940–2953 (2010).

[23] Lashuel, H. A., Hartley, D., Petre, B. M., *et al.*, *Neurodegenerative disease - amyloid pores from pathogenic mutations*, Nature **418** (6895): pp. 291–291 (2002).

[24] Caughey, B. and Lansbury, P. T., *Protofibrils, pores, fibrils, and neurodegeneration: Separating the responsible protein aggregates from the innocent bystanders*, Annual Review of Neuroscience **26**: pp. 267–298 (2003).

[25] Bucciantini, M., Giannoni, E., Chiti, F., *et al.*, *Inherent toxicity of aggregates implies a common mechanism for protein misfolding diseases*, Nature **416** (6880): pp. 507–511 (2002).

[26] Demuro, A., Mina, E., Kayed, R., *et al.*, *Calcium dysregulation and membrane disruption as a ubiquitous neurotoxic mechanism of soluble amyloid oligomers*, Journal of Biological Chemistry **280** (17): pp. 17294–17300 (2005).

[27] Fink, A. L., *The aggregation and fibrillation of alpha-synuclein*, Accounts of Chemical Research **39** (9): pp. 628–634 (2006).

[28] Lambert, M. P., Barlow, A. K., Chromy, B. A., *et al.*, *Diffusible, nonfibrillar ligands derived from a beta(1-42) are potent central nervous system neurotoxins*, Proceedings of the National Academy of Sciences, USA **95** (11): pp. 6448–6453 (1998).

[29] Roher, A. E., Chaney, M. O., Kuo, Y. M., *et al.*, *Morphology and toxicity of a beta-(1-42) dimer derived from neuritic and vascular amyloid deposits of alzheimer's disease*, Journal of Biological Chemistry **271** (34): pp. 20631–20635 (1996).

[30] Volles, M. J. and Lansbury, P. T., *Zeroing in on the pathogenic form of alpha-synuclein and its mechanism of neurotoxicity in parkinson's disease*, Biochemistry **42** (26): pp. 7871–7878 (2003).

[31] Recchia, A., Debetto, P., Negro, A., *et al.*, *alpha-synuclein and parkinson's disease*, The FASEB Journal **18** (6): pp. 617–626 (2004).

[32] Pollanen, M. S., Dickson, D. W., and Bergeron, C., *Pathology and biology of the lewy body*, Journal of Neuropathology & Experimental Neurology **52** (3): pp. 183–191 (1993).

[33] Damier, P., Hirsch, E. C., Agid, Y., *et al.*, *The substantia nigra of the human brain: II. patterns of loss of dopamine-containing neurons in parkinson's disease*, Brain **122** (8): pp. 1437–1448 (1999).

[34] Bartels, T., Choi, J. G., and Selkoe, D. J., *alpha-synuclein occurs physiologically as a helically folded tetramer that resists aggregation*, Nature **477** (7362): pp. 107–110 (2011).

[35] Wang, W., Perovic, I., Chittuluru, J., *et al.*, *A soluble alpha-synuclein construct forms a dynamic tetramer*, Proceedings of the National Academy of Sciences, USA **108** (43): pp. 17797–17802 (2011).

[36] Fauvet, B., Mbefo, M. K., Fares, M.-B., *et al.*, *Alpha-synuclein in the central nervous system and from erythrocytes, mammalian cells and E. coli exists predominantly as a disordered monomer*, Journal of Biological Chemistry pp. 15345–15364 (2012).

[37] Zarranz, J. J., Alegre, J., Gómez-Esteban, J. C., *et al.*, *The new mutation, E46K, of alpha-synuclein causes parkinson and lewy body dementia*, Annals of Neurology **55** (2): pp. 164–173 (2004).

[38] Polymeropoulos, M. H., Lavedan, C., Leroy, E., *et al.*, *Mutation in the alpha-synuclein gene identified in families with parkinson's disease*, Science **276** (5321): pp. 2045–2047 (1997).

[39] Kruger, R., Kuhn, W., Muller, T., *et al.*, *AlaSOPro mutation in the gene encoding alpha-synuclein in parkinson's disease*, Nature Genetics **18** (2): pp. 106–108 (1998).

[40] Lesage, S., Anheim, M., Letournel, F., *et al.*, *G51D alpha-synuclein mutation causes a novel parkinsonianpyramidal syndrome*, Annals of Neurology **73** (4): pp. 459–471 (2013).

[41] Hoffman-Zacharska, D., Koziorowski, D., Ross, O. A., *et al.*, *Novel A18T and pA29S substitutions in alpha-synuclein may be associated with sporadic parkinson's disease*, Parkinsonism & Related Disorders **19** (11): pp. 1057–1060 (2013).

[42] Appel-Cresswell, S., Vilarino-Guell, C., Encarnacion, M., *et al.*, *Alpha-synuclein p.H50Q, a novel pathogenic mutation for parkinson's disease*, Movement Disorders **28** (6): pp. 811–813 (2013).

[43] Tofaris, G. K. and Spillantini, M. G., *Physiological and pathological properties of alpha-synuclein*, Cellular and Molecular Life Sciences **64** (17): pp. 2194–2201 (2007).

[44] Alim, M. A., Hossain, M. S., Arima, K., *et al.*, *Tubulin seeds alpha-synuclein fibril formation*, Journal of Biological Chemistry **277** (3): pp. 2112–2117 (2002).

[45] Alim, M. A., Ma, Q.-L., Takeda, K., *et al.*, *Demonstration of a role for a-synuclein as a functional microtubule-associated protein*, Journal of Alzheimer's Disease **6** (4): pp. 435–442 (2004).

[46] Murphy, D. D., Rueter, S. M., Trojanowski, J. Q., *et al.*, *Synucleins are developmentally expressed, and alpha-synuclein regulates the size of the presynaptic vesicular pool in primary hippocampal neurons*, The Journal of Neuroscience **20** (9): pp. 3214–3220 (2000).

[47] Abeliovich, A., Schmitz, Y., Farias, I., *et al.*, *Mice lacking alpha-synuclein display functional deficits in the nigrostriatal dopamine system*, Neuron **25** (1): pp. 239–252 (2000).

[48] Souza, J. M., Giasson, B. I., Lee, V. M. Y., *et al.*, *Chaperone-like activity of synucleins*, FEBS Letters **474** (1): pp. 116–119 (2000).

[49] Chandra, S., Gallardo, G., Fernndez-Chacn, R., *et al.*, *alpha-synuclein cooperates with CSPalpha in preventing neurodegeneration*, Cell **123** (3): pp. 383–396 (2005).

[50] Bonini, N. M. and Giasson, B. I., *Snaring the function of alpha-synuclein*, Cell **123** (3): pp. 359–361 (2005).

[51] Winner, B., Jappelli, R., Maji, S. K., *et al.*, *In vivo demonstration that alpha-synuclein oligomers are toxic*, Proceedings of the National Academy of Sciences, USA **108** (10): pp. 4194–4199 (2011).

[52] Ding, T. T., Lee, S. J., Rochet, J. C., *et al.*, *Annular alpha-synuclein protofibrils are produced when spherical protofibrils are incubated in solution or bound to brain-derived membranes*, Biochemistry **41** (32): pp. 10209–10217 (2002).

[53] van Rooijen, B. D., van Leijenhorst-Groener, K. A., Claessens, M. M. A. E., *et al.*, *Tryptophan fluorescence reveals structural features of alpha-synuclein oligomers*, Journal of Molecular Biology **394** (5): pp. 826–833 (2009).

[54] Giehm, L., Svergun, D. I., Otzen, D. E., *et al.*, *Low-resolution structure of a vesicle disrupting alpha-synuclein oligomer that accumulates during fibrillation*, Proceedings of the National Academy of Sciences, USA **108** (8): pp. 3246–3251 (2011).

[55] Grey, M., Linse, S., Nilsson, H., *et al.*, *Membrane interaction of alpha-synuclein in different aggregation states*, Journal of Parkinson's Disease **1** (4): pp. 359–371 (2011).

[56] Kostka, M., Hoegen, T., Danzer, K. M., *et al.*, *Single particle characterization of iron-induced pore-forming alpha-synuclein oligomers*, Journal of Biological Chemistry **283** (16): pp. 10992–11003 (2008).

[57] Lowe, R., Pountney, D. L., Jensen, P. H., *et al.*, *Calcium(II) selectively induces alpha-synuclein annular oligomers via interaction with the c-terminal domain*, Protein Science **13** (12): pp. 3245–3252 (2004).

[58] Cappai, R., Leck, S. L., Tew, D. J., *et al.*, *Dopamine promotes alpha-synuclein aggregation into SDS-resistant soluble oligomers via a distinct folding pathway*, FASEB journal **19** (10): pp. 1377–1379 (2005).

[59] Leong, S. L., Pham, C. L. L., Galatis, D., *et al.*, *Formation of dopamine-mediated alpha-synuclein-soluble oligomers requires methionine oxidation*, Free Radical Biology and Medicine **46** (10): pp. 1328–1337 (2009).

[60] Leong, S. L., Cappai, R., Barnham, K. J., *et al.*, *Modulation of alpha-synuclein aggregation by dopamine: A review*, Neurochemical Research **34** (10): pp. 1838–1846 (2009).

[61] Rekas, A., Cappai, R., Curtain, C., *et al.*, *Chapter 27 - dopamine-induced alpha-synuclein oligomers*, in: V. N. Uversky and Y. L. Lyubchenko (Eds.), *Bio-nanoimaging*, pp. 291–300, Academic Press, Boston (2014).

[62] Rekas, A., Knott, R. B., Sokolova, A., *et al.*, *The structure of dopamine induced alpha-synuclein oligomers*, European Biophysics Journal **39** (10): pp. 1407–1419 (2010).

[63] Nasstrom, T., Fagerqvist, T., Barbu, M., *et al.*, *The lipid peroxidation products 4-oxo-2-nonenal and 4-hydroxy-2-nonenal promote the formation of alpha-synuclein oligomers with distinct biochemical, morphological, and functional properties*, Free Radical Biology and Medicine **50** (3): pp. 428–437 (2011).

[64] De Franceschi, G., Frare, E., Pivato, M., *et al.*, *Structural and morphological characterization of aggregated species of alpha-synuclein induced by docosahexaenoic acid*, Journal of Biological Chemistry **286** (25): pp. 22262–22274 (2011).

[65] Jo, E. J., McLaurin, J., Yip, C. M., *et al.*, *Alpha-synuclein membrane interactions and lipid specificity*, Journal of Biological Chemistry **275** (44): pp. 34328–34334 (2000).

[66] Lee, H. J., Choi, C., and Lee, S. J., *Membrane-bound alpha-synuclein has a high aggregation propensity and the ability to seed the aggregation of the cytosolic form*, Journal of Biological Chemistry **277** (1): pp. 671–678 (2002).

[67] Georgieva, E. R., Ramlall, T. F., Borbat, P. P., *et al.*, *Membrane-bound alpha-synuclein forms an extended helix: Long-distance pulsed ESR measurements using vesicles, bicelles, and rodlike micelles*, Journal of the American Chemical Society **130** (39): pp. 12856–12857 (2008).

[68] Mihajlovic, M. and Lazaridis, T., *Membrane-bound structure and energetics of alpha-synuclein*, Proteins **70**: pp. 761–78 (2008).

[69] Munishkina, L. A., Phelan, C., Uversky, V. N., *et al.*, *Conformational behavior and aggregation of alpha-synuclein in organic solvents: Modeling the effects of membranes*, Biochemistry **42** (9): pp. 2720–2730 (2003).

[70] Wright, J. A., Wang, X., and Brown, D. R., *Unique copper-induced oligomers mediate alpha-synuclein toxicity*, The FASEB Journal **23** (8): pp. 2384–2393 (2009).

[71] Kim, H.-Y., Cho, M.-K., Kumar, A., *et al.*, *Structural properties of pore-forming oligomers of alpha-synuclein.*, Journal of the American Chemical Society **131**: pp. 17482–17489 (2009).

[72] Danzer, K. M., Haasen, D., Karow, A. R., *et al.*, *Different species of alpha-synuclein oligomers induce calcium influx and seeding*, Journal of Neuroscience **27** (34): pp. 9220–9232 (2007).

[73] Conway, K. A., Lee, S. J., Rochet, J. C., *et al.*, *Accelerated oligomerization by parkinson's disease linked alpha-synuclein mutants*, Annals of the New York academy of sciences **920**: pp. 42–45 (2000).

[74] Conway, K. A., Lee, S. J., Rochet, J. C., *et al.*, *Acceleration of oligomerization, not fibrillization, is a shared property of both alpha-synuclein mutations linked to early-onset parkinson's disease: Implications for pathogenesis and therapy*, Proceedings of the National Academy of Sciences, USA **97** (2): pp. 571–576 (2000).

[75] Hong, D.-P., Fink, A. L., and Uversky, V. N., *Structural characteristics of alpha-synuclein oligomers stabilized by the flavonoid baicalein*, Journal of Molecular Biology **383** (1): pp. 214–223 (2008).

[76] Fauerbach, J. A., Yushchenko, D. A., Shahmoradian, S. H., *et al.*, *Supramolecular non-amyloid intermediates in the early stages of alpha-synuclein aggregation*, Biophysical Journal **102** (5): pp. 1127–1136 (2012).

[77] Apetri, M. M., Maiti, N. C., Zagorski, M. G., *et al.*, *Secondary structure of alpha-synuclein oligomers: Characterization by raman and atomic force microscopy*, Journal of Molecular Biology **355** (1): pp. 63–71 (2006).

[78] Hoyer, W. G., Cherny, D., Subramaniam, V., *et al.*, *Rapid self-assembly of alpha-synuclein observed by in situ atomic force microscopy*, Journal of Molecular Biology **340** (1): pp. 127–139 (2004).

[79] Lashuel, H. A., Petre, B. M., Wall, J., *et al.*, *alpha-synuclein, especially the parkinson's disease-associated mutants, forms pore-like annular and tubular protofibrils*, Journal of Molecular Biology **322** (5): pp. 1089–1102 (2002).

[80] Quist, A., Doudevski, L., Lin, H., *et al.*, *Amyloid ion channels: A common structural link for protein-misfolding disease*, Proceedings of the National Academy of Sciences, USA **102** (30): pp. 10427–10432 (2005).

[81] Lorenzen, N., Nielsen, S. B., Buell, A. K., *et al.*, *The role of stable alpha-synuclein oligomers in the molecular events underlying amyloid formation*, Journal of the American Chemical Society **136** (10): pp. 3859–3868 (2014).

[82] Shtilerman, M. D., Ding, T. T., and Lansbury, P. T., *Molecular crowding accelerates fibrillization of alpha-synuclein: Could an increase in the cytoplasmic protein concentration induce parkinson's disease?*, Biochemistry **41** (12): pp. 3855–3860 (2002).

[83] Hoyer, W., Cherny, D., Subramaniam, V., *et al.*, *Impact of the acidic c-terminal region comprising amino acids 109-140 on alpha-synuclein aggregation in vitro*, Biochemistry **43**: pp. 16233–42 (2004).

[84] Rochet, J. C., Conway, K. A., and Lansbury, P. T., *Inhibition of fibrillization and accumulation of prefibrillar oligomers in mixtures of human and mouse alpha-synuclein*, Biochemistry **39** (35): pp. 10619–10626 (2000).

[85] Kaylor, J., Bodner, N., Edridge, S., *et al.*, *Characterization of oligomeric intermediates in alpha-synuclein fibrillation: FRET studies of Y125W/Y133F/Y136F alpha-synuclein*, Journal of Molecular Biology **353** (2): pp. 357–372 (2005).

[86] Burstein, E. A., Vedenkin.Ns, and Ivkova, M. N., *Fluorescence and location of tryptophan residues in protein molecules*, Photochemistry and Photobiology **18** (4): pp. 263–279 (1973).

[87] Chen, Y. and Barkley, M. D., *Toward understanding tryptophan fluorescence in proteins*, Biochemistry **37** (28): pp. 9976–9982 (1998).

[88] Szabo, A. G. and Rayner, D. M., *Fluorescence decay of tryptophan conformers in aqueous-solution*, Journal of the American Chemical Society **102** (2): pp. 554–563 (1980).

[89] Dusa, A., Kaylor, J., Edridge, S., *et al.*, *Characterization of oligomers during alpha-synuclein aggregation using intrinsic tryptophan fluorescence*, Biochemistry **45** (8): pp. 2752–2760 (2006).

[90] Cohen, S. I. A., Vendruscolo, M., Welland, M. E., *et al.*, *Nucleated polymerization with secondary pathways. i. time evolution of the principal moments*, Journal of Chemical Physics **135** (6): p. 065105 (2011).

[91] Cohen, S. I. A., Vendruscolo, M., Dobson, C. M., *et al.*, *Nucleated polymerization with secondary pathways. II. determination of self-consistent solutions to growth processes described by non-linear master equations*, Journal of Chemical Physics **135** (6): p. 065106 (2011).

[92] Cohen, S. I. A., Vendruscolo, M., Dobson, C. M., *et al.*, *Nucleated polymerization with secondary pathways. III. equilibrium behavior and oligomer populations*, Journal of Chemical Physics **135** (6): p. 065107 (2011).

[93] Paleologou, K. E., Oueslati, A., Shakked, G., *et al.*, *Phosphorylation at s87 is enhanced in synucleinopathies, inhibits alpha-synuclein oligomerization, and influences synuclein-membrane interactions*, The Journal of Neuroscience **30** (9): pp. 3184–3198 (2010).

[94] van Rooijen, B. D., Claessens, M. M. A. E., and Subramaniam, V., *Lipid bilayer disruption by oligomeric alpha-synuclein depends on bilayer charge and accessibility of the hydrophobic core*, Biochimica et Biophysica Acta (BBA) - Biomembranes **1788** (6): pp. 1271–1278 (2009).

[95] Ionut Iurascu, M., Cozma, C., Tomczyk, N., *et al.*, *Structural characterization of beta-amyloid oligomer-aggregates by ion mobility mass spectrometry and electron spin resonance spectroscopy*, Analytical and Bioanalytical Chemistry **395** (8): pp. 2509–2519 (2009).

[96] Hogen, T., Levin, J., Schmidt, F., *et al.*, *Two different binding modes of alpha-synuclein to lipid vesicles depending on its aggregation state*, Biophysical Journal **102** (7): pp. 1646–1655 (2012).

[97] Plotegher, N., Gratton, E., and Bubacco, L., *Number and brightness analysis of alpha-synuclein oligomerization and the associated mitochondrial morphology alterations in live cells*, Biochimica et Biophysica Acta (BBA) - General Subjects **1840** (6): pp. 2014–2024 (2014).

[98] Cremades, N., Cohen, S. I. A., Deas, E., *et al.*, *Direct observation of the interconversion of normal and toxic forms of alpha-synuclein*, Cell **149** (5): pp. 1048–1059 (2012).

[99] Ding, H., Wong, P. T., Lee, E. L., *et al.*, *Determination of the oligomer size of amyloidogenic protein beta-amyloid(1-40) by single-molecule spectroscopy*, Biophysical Journal **97**: pp. 912–921 (2009).

[100] Dukes, K. D., Rodenberg, C. F., and Lammi, R. K., *Monitoring the earliest amyloid-beta oligomers via quantized photobleaching of dye-labeled peptides.*, Analytical Biochemistry **382**: pp. 29–34 (2008).

[101] Lakowicz, J., *Principles of Fluorescence Spectroscopy*, Principles of Fluorescence Spectroscopy, Kluwer Academic/Plenum Publishers, New York, Boston, Dordrecht, London, Moscow, third edition (2006).

[102] Diaspro, A., Chirico, G., Usai, C., *et al.*, *Photobleaching*, in: J. B. Pawley (Ed.), *Handbook Of Biological Confocal Microscopy*, pp. 690–702, Springer US (2006).

[103] Moerner, W. E. and Fromm, D. P., *Methods of single-molecule fluorescence spectroscopy and microscopy*, Review of Scientific Instruments **74** (8): pp. 3597–3619 (2003).

[104] Wan, D. S., Rajadhyaksha, M., and Webb, R. H., *Analysis of spherical aberration of a water immersion objective: application to specimens with refractive indices 1.33-1.40*, Journal of Microscopy **197**: pp. 274–284 (2000).

[105] Meixner, A. J. and Weber, M. A., *Single molecule spectral dynamics at room temperature*, Journal of Luminescence **86** (3-4): pp. 181–187 (2000).

[106] Hess, S. T. and Webb, W. W., *Focal volume optics and experimental artifacts in confocal fluorescence correlation spectroscopy*, Biophysical Journal **83** (4): pp. 2300–2317 (2002).

[107] Pawley, J. B. (Ed.), *Handbook Of Biological Confocal Microscopy*, Springer US, New York, third edition (2006).

[108] Kozankiewicz, B. and Orrit, M., *Single-molecule photophysics, from cryogenic to ambient conditions*, Chemical Society Reviews **43** (4): pp. 1029–1043 (2014).

[109] Stennett, E. M. S., Ciuba, M. A., and Levitus, M., *Photophysical processes in single molecule organic fluorescent probes*, Chemical Society Reviews **43** (4): pp. 1057–1075 (2014).

[110] Zondervan, R., Kulzer, F., Kolchenko, M. A., *et al.*, *Photobleaching of rhodamine 6G in poly(vinyl alcohol) at the ensemble and single-molecule levels*, Journal of Physical Chemistry A **108** (10): pp. 1657–1665 (2004).

[111] Ha, T. and Xu, J., *Photodestruction intermediates probed by an adjacent reporter molecule*, Physical Review Letters **90** (22) (2003).

[112] Hubner, C. G., Renn, A., Renge, I., *et al.*, *Direct observation of the triplet lifetime quenching of single dye molecules by molecular oxygen*, Journal of Chemical Physics **115** (21): pp. 9619–9622 (2001).

[113] Ha, T. and Tinnefeld, P., *Photophysics of fluorescent probes for single-molecule biophysics and super-resolution imaging*, Annual Review of Physical Chemistry **63**: pp. 595–617 (2012).

[114] Schweitzer, C. and Schmidt, R., *Physical mechanisms of generation and deactivation of singlet oxygen*, Chemical Reviews **103** (5): pp. 1685–1757 (2003).

[115] Bonnett, R. and Martinez, G., *Photobleaching of sensitisers used in photodynamic therapy*, Tetrahedron **57** (47): pp. 9513–9547 (2001).

[116] van de Linde, S., Krstic, I., Prisner, T., *et al.*, *Photoinduced formation of reversible dye radicals and their impact on super-resolution imaging*, Photochemical & Photobiological Sciences **11** (12): pp. 1952–1953 (2012).

[117] Rasnik, I., McKinney, S. A., and Ha, T., *Nonblinking and longlasting single-molecule fluorescence imaging*, Nature Methods **3** (11): pp. 891–893 (2006).

[118] Bates, M., Blosser, T. R., and Zhuang, X. W., *Short-range spectroscopic ruler based on a single-molecule optical switch*, Physical Review Letters **94** (10) (2005).

[119] Zhang, H. and Guo, P., *Single molecule photobleaching (SMPB) technology for counting of RNA, DNA, protein and other molecules in nanoparticles and biological complexes by TIRF instrumentation*, Methods (2014).

[120] Leake, M. C., Chandler, J. H., Wadhams, G. H., *et al.*, *Stoichiometry and turnover in single, functioning membrane protein complexes*, Nature **443** (7109): pp. 355–358 (2006).

[121] Shu, D., Zhang, H., Jin, J., *et al.*, *Counting of six pRNAs of phi29 DNA-packaging motor with customized single-molecule dual-view system*, EMBO Journal **26** (2): pp. 527–537 (2007).

[122] Hohlbein, J. and Huebner, C. G., *Three-dimensional orientation determination of the emission dipoles of single molecules: The shot-noise limit*, Journal of Chemical Physics **129** (9) (2008).

[123] van Rooijen, B. D., Claessens, M. M. A. E., and Subramaniam, V., *Membrane permeabilization by oligomeric alpha-synuclein: In search of the mechanism*, Plos One **5** (12) (2010).

[124] van Rooijen, B. D., *Structural and functional insights into interactions of oligomeric alpha-synuclein with lipid membranes*, PhD, University of Twente (2009).

[125] van Raaij, M. E., Segers-Nolten, I. M. J., and Subramaniam, V., *Quantitative morphological analysis reveals ultrastructural diversity of amyloid fibrils from alpha-synuclein mutants*, Biophysical Journal **91** (11): pp. L96–L98 (2006).

[126] Conway, K. A., Rochet, J. C., Bieganski, R. M., *et al.*, *Kinetic stabilization of the alpha-synuclein protofibril by a dopamine-alpha-synuclein adduct*, Science **294** (5545): pp. 1346–1349 (2001).

[127] Herrera, F. E., Chesi, A., Paleologou, K. E., *et al.*, *Inhibition of alpha-synuclein fibrillization by dopamine is mediated by interactions with five c-terminal residues and with e83 in the NAC region*, PLoS One **3** (10): p. e3394 (2008).

[128] Mosharov, E. V., Larsen, K. E., Kanter, E., *et al.*, *Interplay between cytosolic dopamine, calcium, and alpha-synuclein causes selective death of substantia nigra neurons*, Neuron **62** (2): pp. 218–229 (2009).

[129] Li, H., Rahimi, F., Sinha, S., *et al.*, *Amyloids and protein aggregation analytical methods*, in: *Encyclopedia of Analytical Chemistry*, John Wiley & Sons, Ltd (2006).

[130] van der Meer, B. W., *Kappa-squared: from nuisance to new sense*, Journal of Biotechnology **82** (3): pp. 181–96 (2002).

[131] Deniz, A. A., Laurence, T. A., Dahan, M., *et al.*, *Ratiometric single-molecule studies of freely diffusing biomolecules*, Annual Review of Physical Chemistry **52**: pp. 233–253 (2001).

[132] Schuler, B., Lipman, E. A., and Eaton, W. A., *Probing the free-energy surface for protein folding with single-molecule fluorescence spectroscopy*, Nature **419** (6908): pp. 743–747 (2002).

[133] Beekman, P., *Single-molecule FRET measurements on fluorescently labeled alpha-synuclein*, Technical report, University of Twente (2013).

[134] Haustein, E. and Schwille, P., *Fluorescence correlation spectroscopy: Novel variations of an established technique*, Annual Review of Biophysics and Biomolecular Structure **36** (1): pp. 151–169 (2007).

[135] Veldhuis, G., Segers-Nolten, I., Ferlemann, E., *et al.*, *Single-molecule FRET reveals structural heterogeneity of SDS-bound alpha-synuclein*, Chembiochem **10** (3): pp. 436–439 (2009).

[136] Zhou, H.-X., *Polymer models of protein stability, folding, and interactions*, Biochemistry **43** (8): pp. 2141–2154 (2004).

[137] Nath, A., Sammalkorpi, M., DeWitt, D. C., *et al.*, *The conformational ensembles of alpha-synuclein and tau: Combining single-molecule FRET and simulations*, Biophysical Journal **103** (9): pp. 1940–1949 (2012).

[138] Trexler, A. J. and Rhoades, E., *Single molecule characterization of alpha-synuclein in aggregation-prone states*, Biophysical Journal **99** (9): pp. 3048–3055 (2010).

Nederlandse samenvatting

Gedurende de laatste 15 jaar zijn we getuige geweest van een grote verschuiving in de focus van het onderzoek naar de oorzaak van amyloïde ziektes. In plaats van de volgroeide amyloïde fibrillen, worden nu de nanometer grote oligomeren, een tussenliggende soort in het aggregatieproces, gezien als de soort die schadelijk is voor cellen en aan de basis van de ziektes staan. Sinds deze verschuiving zijn er vele verslagen in de wetenschappelijke literatuur te vinden die deze oligomeren bespreken. In deze thesis focussen we ons op α-Synucleine (αS) oligomeren, mogelijk de belangrijkste spelers in de ziekte van Parkinson zijn.

Sinds men zich realiseerde dat αS oligomeren schadelijk zijn voor cellen en misschien de ziekte van Parkinson veroorzaken, heeft men veel aandacht besteed aan 1) het volledig karakteriseren van deze oligomeren wat betreft structuur, vorm en aggregatiegetal en 2) het verkrijgen van gedetailleerde informatie over hoe deze oligomeren vormen. Al deze informatie is essentieel als je het verloop van de ziekte wilt begrijpen en specifieke doelen wilt vinden die geschikt zijn voor medische interventie.

Je zou verwachten dat al het onderzoek dat gedaan wordt snel tot een gedetailleerde biofysische beschrijving van de oligomeren zou leiden en een medische strategie zou moeten opleveren. Integendeel, het werd akelig duidelijk dat, afhankelijk van de omstandigheden waaronder de oligomeren zich vormen, deze oligomeren een ontzettend grote variatie vertonen wat betreft structuur en vorm. Dit maakt het heel erg moeilijk om een specifiek type oligomeer aan te wijzen die schadelijk voor cellen

is en deze volledig te karakteriseren. Zelfs informatie wat betreft het aggregatiegetal van de verschillende oligomeren ontbreekt, aangezien het moeilijk is om met behulp van de standaard technieken betrouwbare resultaten te krijgen. Dit komt omdat deze technieken meestal een vergelijkingsmonster nodig hebben of ervan uitgaan dat je het moleculaire gewicht van de oligomeren kunt bepalen, wat nu juist ontzettend moeilijk is voor deze over het algemeen instabiele aggregaten die opgebouwd zijn uit het intrinsiek ongeordende eiwit αS. Daarom is er een grote behoefte aan een techniek die deze problemen omzeilt en waarmee je direct het aggregatiegetal kunt bepalen.

Daarom hebben wij een nieuwe techniek ontwikkeld om het aggregatiegetal van eiwit aggregaten te bepalen. Deze techniek maakt gebruik van de combinatie van enkel-molecuul fotobleken en sub-stoichiometrische fluorescente labeling. Het aggregatiegetal kan bepaald worden door, voor een groot aantal oligomeren, het aantal discrete fotobleek stappen in een intensiteit-tijd diagram te tellen en vervolgens een statistische analyse uit te voeren op het histogram van fotobleek stappen.

Met deze techniek kun je direct het aggregatiegetal van αS oligomeren bepalen, en ook van grote macromoleculaire samenstellingen van eiwitten in het algemeen, zonder dat je een vergelijkingsmonster nodig hebt of een hoge ruimtelijke resolutie. Deze techniek is daarom uitermate geschikt om subtiele verschillen in het aggregatiegetal te bepalen en maakt het mogelijk om een systematische studie uit te voeren om de invloed van de aggregatieomstandigheden op het aggregatiegetal te bepalen. Daar bovenop maakt deze techniek het mogelijk om een mogelijke verdeling in het aggregatiegetal te bepalen.

Wij hebben deze nieuwe techniek gebruikt om het aggregatiegetal van αS oligomeren, die onder een aantal verschillende aggregatieomstandigheden zijn gevormd, te bepalen. Voor oligomeren die gevormd werden onder hoge eiwit concentraties en tijdens langdurig incuberen, vonden wij geen verdeling in het aggregatiegetal, maar een enkele, goed gedefinieerde soort oligomeren die bestaat uit ongeveer 31 monomeren per oligomeer. Daarbovenop hebben we vastgesteld dat de fluorescente labels die we gebruikt hebben het aggregatieproces niet benvloeden. De combinatie van deze resultaten en de resultaten uit een eerdere studie door van Rooijen *et al.* waar ze een systematisch studie met behulp van Tryptofaan hebben uitgevoerd om inzicht te krijgen in de globale structuur van de oligomeren, suggereert dat de oligomeren

gevormd onder deze omstandigheden zichzelf organiseren in een stabiele structuur waarin de kern die uit de eerste 100 aminozuren van het monomere eiwit bestaat een hoge dichtheid heeft en de buitenschil die bloot staat aan de vloeistof en bestaat uit de C-terminus van het eiwit juist heel erg luchtig is.

Met dezelfde techniek hebben we ook oligomeren bestudeerd die gevormd zijn onder andere aggregatieomstandigheden, namelijk korte incubatietijden en in de aanwezigheid van de neurotransmitter dopamine. Met behulp van deze sub-stoichiometrisch gelabelde oligomeren hebben we laten zien dat we in staat zijn om onderscheid te maken tussen meerdere soorten oligomeren in hetzelfde monster en dat we het aggregatiegetal van alle soorten tegelijkertijd kunnen bepalen vanuit een enkel histogram van fotobleek stappen. Voor deze oligomeren vonden we een soort dat bestond uit 15-19 monomeren per oligomeer en een tweede soort die bestond uit 34-38 monomeren per oligomeer. Als we dezelfde aggregatieomstandigheden gebruiken met als enige verschil dat er geen dopamine aanwezig is, zien we dat er nog steeds twee soorten oligomeren zijn. Maar deze oligomeren hebben wel een duidelijk ander aggregatiegetal: de eerste soort bestaat uit ongeveer 10 monomeren en de tweede soort uit ongeveer 30 monomeren.

Om wat meer inzicht te krijgen in hoe nauwkeurig we het aggregatiegetal van een enkele soort en van een complexer systeem bestaande uit meerdere soorten oligomeren kunnen bepalen, hebben we gebruik gemaakt van gesimuleerde histogrammen van fotobleek stappen. We hebben laten zien dat in het algemeen de techniek goed werkt voor een groot bereik aan aggregatiegetallen en dus binnen een groot bereik van label dichtheden. Het optimale bereik van label dichtheden hangt van het aggregatiegetal van het bestudeerde systeem af. Het optimale bereik van label dichtheden voor een aggregatiegetal van bijvoorbeeld 30, wat we ook gevonden hebben in hoofdstuk 3, ligt tussen de $\sim$7% en $\sim$25%, wat een erg groot bereik is met meer dan een factor 3 in label dichtheid. Binnen dit bereik kan het aggregatiegetal met een nauwkeurigheid van $\pm$3 monomeren bepaald worden. Zoals je zou verwachten is het voor een complexer systeem dat uit meerdere soorten oligomeren bestaat het hoofdzakelijk het verschil tussen de aggregatiegetallen wat bepaald hoe nauwkeurig het aggregatiegetal bepaald kan worden en wat de minimale fractie van een soort oligomeren is wat nog terug gevonden kan worden. Hoe dichter de aggregatiegetallen bij elkaar liggen, hoe lager

de nauwkeurigheid is en hoe moeilijker het is om het verschil tussen de verschillende soorten te zien. De nauwkeurigheid voor een systeem dat bijvoorbeeld uit een 20-meer en een 30-meer bestaat, vergelijkbaar met wat we in hoofdstuk 4 gevonden hebben, is lager dan voor een simpeler systeem dat uit èèn soort bestaat en we hebben de nauwkeurigheid bepaald op ± 5 voor de 20-meer en ± 4 voor de 30-meer.

Zoals hierboven al genoemd is, als je een farmaceutisch doelwit wilt vinden, is het belangrijk om de oligomeren niet alleen te karakteriseren, maar ook te bestuderen hoe ze vormen. Belangrijke informatie over hoe de oligomeren vormen zit verborgen in de allereerste stappen van het aggregatieproces. αS als monomeer wordt beschouwd als een intrinsiek ongeordend eiwit dat continue veranderingen in zijn 3D vouwing ondergaat. Tot op heden is het onduidelijk of er een bepaald aantal vouwingen zijn dat het eiwit in staat gesteld om te aggregeren of dat aggregatie onafhankelijk van de vouwing is. Wij hebben metingen aan enkele Förster resonante energie overdracht (FRET) paren gedaan om de vouwing van αS monomeren die in een oligomeer ingelijfd zaten gedeeltelijk in kaart te brengen.

We hebben de histogrammen van FRET efficiënties bepaald voor een serie van zes αS mutanten die ingelijfd waren in oligomeren. Voor alle zes mutanten vonden we in het histogram een enkele piek die gecentreerd was rond een efficiëntie van 0%, wat suggereert dat de energie donor en energie ontvanger ver van elkaar verwijderd zijn. Dat alle zes de histogrammen hetzelfde zijn, suggereert dat de monomeren wel degelijk een specifieke vouwing moeten hebben nadat ze door de oligomeren zijn ingelijfd. Als de monomeren een puur willekeurige vouwing hebben, zou je heel breed FRET histogramm verwachten die in ieder geval enige energie overdracht laten zien voor een kleine subgroep van de oligomeren. Daarom moeten de monomeren wel degelijk een specifieke vouwing hebben, waarschijnlijk een uitgestrekte vouwing. Bovendien suggereren onze vindingen dat de monomeren inderdaad een beperkt aantal vouwingen hebben dat ze toelaat om te aggregeren, aangezien de FRET histogrammen smal zijn en er geen pieken zijn op hogere FRET efficiënties.

Acknowledgements

It is finished! Who would have thought all those years ago that this moment would actually happen. A PhD seems so long when you are at the beginning. It seem that there is almost an infinite amount of time during which you can actually change the world. But the further you get into the project and the less time you have, the more you realize what you can do (or afterward, should have done) in such limited time. Science is not always fast, it doesn't always go right the first time (or second time for that matter), but it definitely is fun to do!

All the work that was presented in this thesis was of course a group effort for which I can only take part of the credit. I would like to thank everyone with whom I had the pleasure of working with during these last few years and who made it possible to do all this fantastic science. It was great to have so much freedom to fill in the project as I wished or to explore some unrelated, but very interesting, scientific questions, have collaborations both within the university and outside of the university. I would like to take this opportunity to thank a few people specifically.

Vinod, at the beginning, we had an interesting discussion partly about what we could do, but mostly about what I actually wanted to do. In hindsight, I realized that you probably already knew that before I did and that it is not a coincidence I ended up doing this specific project. I am very grateful for the opportunity and all the advice you gave me during these years, not only about work related issues, but also on the personal nature. I enjoyed our discussions about how science works (or

should work), and about all the cool stuff we could do, but unfortunately didn't have time to do.

Christian, it was a pleasure to work with you for all those years and having you as my daily supervisor. You taught me a lot about science and about being critical. Your door was always open and you were always enthusiastic about the work. Although you were always in for a good discussion, you also made sure that the additional work that resulted from these discussions was finished latest yesterday. I'm still disappointed that you moved to an office without a heater that I could sit on, but in the end, I guess I got used to the chairs as well.

During these years, I had the pleasure of working with many different people in the dark, but always busy, optical lab: Martijn, Remco, Jord, Amin, Anja, Chris, Harmen, and Peter: You all made it so much more enjoyable being there and made sure that there was no room for getting depressed during the dark and cold winters.

Of course, this work would not have been possible without the invaluable administrative and technical support that made everything so much easier, and without the infinite amount of α-Synuclein always available to us: Syl, Robert, Kees, Kirsten, Yvonne, Nathalie, and Irene, thank you very much!

I always appreciated the relaxed, but still challenging, working atmosphere in the NBP group, but work is fortunately only one part of life. I would like to thank the entire NBP group for making the time we spend outside of work also fantastic with barbeques, bowling, movies, the occasional chat in the office, or just having a coffee together. This was a large part of what made the science so much fun. Martijn, we should definitely finish the special beer menu soon :).

Finally, I would like to thank my family and friends for their support. Even when life didn't exactly go as planned, you were there for me to support me and help me in making the right decision. Or if there was no right or wrong, we just had a beer and everything solved itself.

Burcu, my sweet girl, although it took us a while to find each other, you make my life better with your love and friendship. And wherever our journey leads us, as long as we are together, I'm sure we'll be happy there.

Niels, Enschede, 2014

List of publications

Published articles

N. Zijlstra, M.M.A.E. Claessens, C. Blum, and V. Subramaniam, *Elucidating the aggregation number of dopamine-induced α-Synuclein oligomeric assemblies*, Biophysical Journal **106**: pp. 440-446 (2014).

N. Zijlstra, and V. Subramaniam, *Structural and Compositional Information about Pre-Amyloid Oligomers*, in: *Amyloid Fibrils and Prefibrillar Aggregates: Molecular and Biological Properties*, D.E. Otzen (ed), pp. 103-126, Wiley-VCH Verlag GmbH & Co. KGaA, Weinheim (2013).

C. Blum, N. Zijlstra, A. Lagendijk, M. Wubs, A.P. Mosk, V. Subramaniam, and W.L. Vos, *Nanophotonic control of the Förster resonance energy transfer efficiency*, Physical Review Letters **109**: pp. 203601 (2012).

M.T. Stöckl, N. Zijlstra, and V. Subramaniam, *α-Synuclein Oligomers: An Amyloid Pore?*, Molecular Neurobiology **47**: pp. 613-621 (2012).

N. Zijlstra, C. Blum, I.M.J. Segers-Nolten, M.M.A.E. Claessens, and V. Subramaniam, *Molecular composition of sub-stoichiometrically labeled α-Synuclein oligomers*

determined by single-molecule photobleaching, Angewandte Chemie IE **51** (35): pp. 8821-8824 (2012).

M. Robotta, C. Hintze, S. Schildknecht, N. Zijlstra, C. Jngst, C. Karreman, M. Huber, M. Leist, V. Subramaniam, and M. Drescher, *Locally resolved membrane binding affinity of the α-Synuclein N-terminus*, Biochemistry **51** (19): pp. 39603962 (2012).

Manuscripts in preparation

N. Zijlstra, C. Blum, and V. Subramaniam, *Single-molecule photobleaching on sub-stoichiometrically labeled aggregates: How well can we do?*

N. Zijlstra, N. Schilder, and V. Subramaniam, *Fluorescence methods for delineating oligomeric amyloid intermediates*, in: *Protein Aggregation*, D. Eliezer (ed), Springer Series on: *Methods in Molecular Biology.*

Conference proceedings

N. Zijlstra, C. Blum, and V. Subramaniam, *Aggregation conditions strongly influence the molecular composition of alpha-synuclein oligomers*, European Biophyisics Journal **42**: pp. S200-S200 (2013).

C. Blum, N. Zijlstra, A. Lagendijk, M. Wubs, A.P. Mosk, V. Subramaniam, and W.L. Vos, *Can nanophotonics control the Förster resonance energy transfer efficiency?*, International Quantum Electronics Conference (2013).

C. Blum, N. Zijlstra, Y. Cesa, V. Subramaniam, J.M. van den Broek, A.P. Mosk, and W.L. Vos, *Nanobiophotonics: using the nanophotonics toolbox to manipulate biological fluorophores*, International Workshop on BioPhotonics (2011).

Oral presentations at international conferences

Aggregation number of α-synuclein amyloid oligomers determined by single-molecule photobleaching, **European Biophysical Societies' Association Meeting**, Lisbon: 2013, July 17.

Establishing the composition of alpha-synuclein amyloid oligomers using single molecule photobleaching, **Optics Within Life Sciences Meeting**, Genua: 2012, July 6.

Molecular composition of alpha-synuclein oligomers determined by single-molecule photobleaching, **Hole-Burning and Single-Molecule Meeting**, Tuebingen: 2012, August 27.

Poster presentations at international conferences

N. Zijlstra, G.M.J. Segers-Nolten, M.M.A.E. Claessens, C. Blum, and V. Subramaniam, *Shining light on amyloid protein aggregates*, **Focus on Microscopy**: 2013, March 24-27.

N. Zijlstra, C. Blum, G.M.J. Segers-Nolten, M.M.A.E. Claessens, and V. Subramaniam, *Establishing the molecular composition of alpha-synuclein oligomers by sub-stoichiometric labeling and single-molecule photobleaching*, **Biophysical Society Meeting**: 2012, February 25-28.

N. Zijlstra, C. Blum, G.M.J. Segers-Nolten, M.M.A.E. Claessens, and V. Subramaniam, *Establishing the composition of alpha-synuclein oligomers using single-molecule photobleaching*, **European Biophysical Societies' Association Meeting**: 2011, August 23-27.